POLITECNICO DI TORINO

Collegio di Ingegneria Chimica e dei Materiali

Corso di Laurea Magistrale
in Ingegneria Chimica e dei Processi Sostenibili

Tesi di Laurea Magistrale

Mathematical modelling of the spray-freeze-drying process applied to biopharmaceuticals

Relatori

prof. Roberto Pisano
prof. Gianluca Boccardo

Candidato

Raffaele Tuccinardi

Dicembre 2021

Sommario esteso

La produzione farmaceutica in continuo

Negli ultimi 50 anni, l'industria farmaceutica ha ottimizzato la produzione batch dei farmaci in modo tale da soddisfare la richiesta di maggiori volumi di produzione. Tuttavia, la tecnologia in discontinuo non permette un'adeguata flessibilità al processo di produzione, portando ad inefficienze nei controlli di qualità del prodotto finito. Le grandi dimensioni richieste alle apparecchiature e gli ingenti scarti del prodotto finito per bassa qualità hanno portato ad una perdita che si stima essere di circa $50 miliardi/anno.

Il passaggio ad una produzione in continuo rappresenta la maggiore fonte di cost saving che attualmente l'industria farmaceutica sta perseguendo. Tale tecnologia permetterebbe una maggiore flessibilità di processo, riducendo le dimensioni delle apparecchiature richieste e garantendo un controllo di qualità on-line continuo ed accurato.

Tuttavia, la transizione da una produzione batch ad una continua vede molti ostacoli nel suo percorso. Il problema più grande sono gli ingenti costi che un'eventuale transizione richiederebbe. Inoltre, le leggi e gli standard a cui l'industria farmaceutica è soggetta dovrebbero essere adeguati ad una produzione continua, il che richiederebbe l'intervento da parte del legislatore con conseguente aumento dei tempi richiesti per la transizione.

Le multinazionali che attualmente avrebbero la forza economica per investire su una tecnologia di produzione in continuo vengono frenate dai suddetti ostacoli e la produzione batch continua ad essere la tecnologia più comune.

Ad oggi sono pochi i processi farmaceutici che possono vantare una produzione in continuo. È, ad esempio, il caso dei processi di granulazione e cristallizzazione.

La maggior parte dei processi di produzione farmaceutica prevedono uno o più step di liofilizzazione. Tale fenomeno consiste nell'eliminazione dell'acqua dalla soluzione contenente il principio attivo dopo averla congelata, sfruttando alti gradi di vuoto e basse temperature per cercare di preservare le caratteristiche morfologiche delle proteine coinvolte. Di conseguenza, il passaggio da una liofilizzazione batch (attualmente la più diffusa) ad una liofilizzazione in continuo garantirebbe un grande step verso una produzione più flessibile ed accurata.

La liofilizzazione in continuo

Il processo di liofilizzazione può essere suddiviso in due grandi fasi. La prima fase, in cui avviene il congelamento della soluzione contenente il principio attivo, è regolata dal processo di nucleazione. La seconda fase, in cui si rimuove il solvente congelato attraverso un processo di sublimazione, è fortemente influenzata dalle condizioni termodinamiche del processo.

La natura stocastica del processo di nucleazione dei cristalli di ghiaccio nella liofilizzazione in batch è la causa principale della non omogeneità nella qualità del prodotto finito. Inoltre, la varianza derivante dalle fluttuazioni nel grado di vuoto durante la fase di sublimazione, non permette un controllo accurato nello scambio di calore a cui il prodotto è soggetto. Come risultato si ottiene un grande scarto di prodotto finito a causa di un'eccessiva umidità residua o perdita di principio attivo.

La realizzazione di un processo di liofilizzazione in continuo dovrebbe presentare due diversi approcci, in base a sé il prodotto da essiccare è presente in bulk o in dosaggi singoli (ad esempio in fiale).

Nella liofilizzazione continua di prodotti in bulk, il dosaggio finale del farmaco avverrebbe alla fine dell'essiccazione ed il trasporto del materiale attraverso le diverse sezioni dell'essiccazione

potrebbe essere facilmente eseguito utilizzando tecnologie come quelle del letto fluidizzato di sistemi vibranti. Nella liofilizzazione continua di singole dosi, il dosaggio della soluzione nel contenitore del farmaco deve essere eseguito prima dell'essiccazione. In quest'ultimo tipo di tecnologia è più facile controllare la sterilità durante l'intera fase di essiccazione, ma il design dell'apparecchiatura dovrebbe considerare l'enorme varietà di dimensioni e forme che i contenitori per farmaci potrebbero avere. In Fig. 1 sono riportati due esempi di tecnologie proposte per la liofilizzazione in continuo.

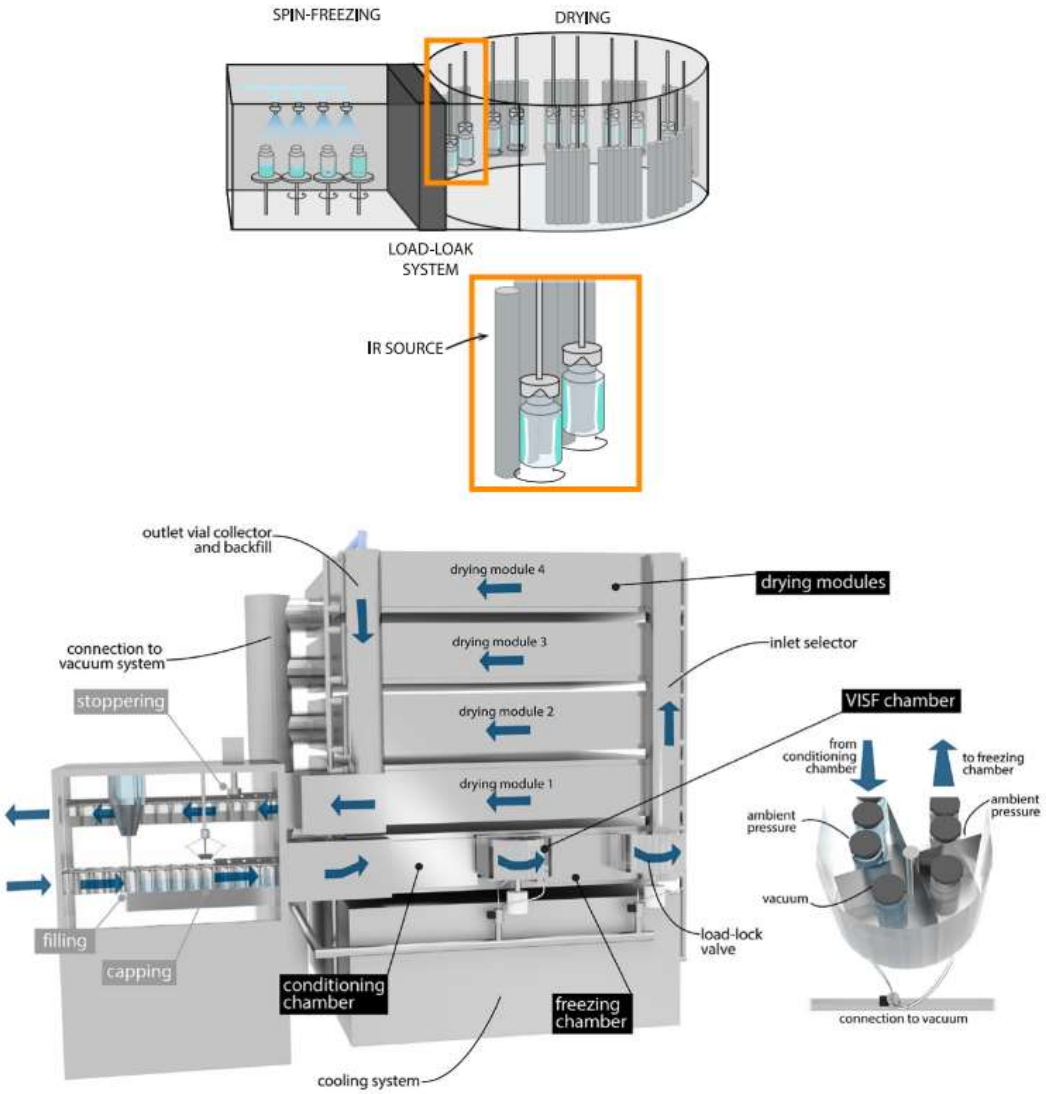

Figura 1: (Top) Liofilizzatore continuo proposto da Corver, (Bottom) Liofilizzatore continuo proposto da Trout *et al*. Immagine modificata, tratta da Pisano (2019).

Spray-freeze-drying

Una delle tecniche di liofilizzazione più innovative su cui vi è una grande attenzione per lo sviluppo di una tecnologia continua è lo spray-freeze-drying (SFD).

La SFD è una tecnologia ideale per liofilizzare proteine, vaccini, aerosol e nanoparticelle dove è essenziale controllare dimensioni e porosità del prodotto finito. Grazie ad una fase di congelamento rapido è possibile prevenire la denaturazione del principio attivo. Diverse tecnologie possono essere selezionate ed utilizzate per eseguire le diverse fasi del metodo ed ottenere varie formulazioni garantendo un'elevata flessibilità. Inoltre, le polveri sferiche

ottenute con la SFD forniscono una velocità di trasferimento di massa e di calore molto elevate, migliori velocità di reidratazione ed affidabilità nella fase di incapsulamento.

Secondo Vishali (2019), la tecnica SFD potrebbe avere un ruolo centrale nello sviluppo di un sistema di somministrazione controllata e mirata di farmaci. In Fig. 2 vengono riportate le fasi principali del processo di spray-freeze-drying.

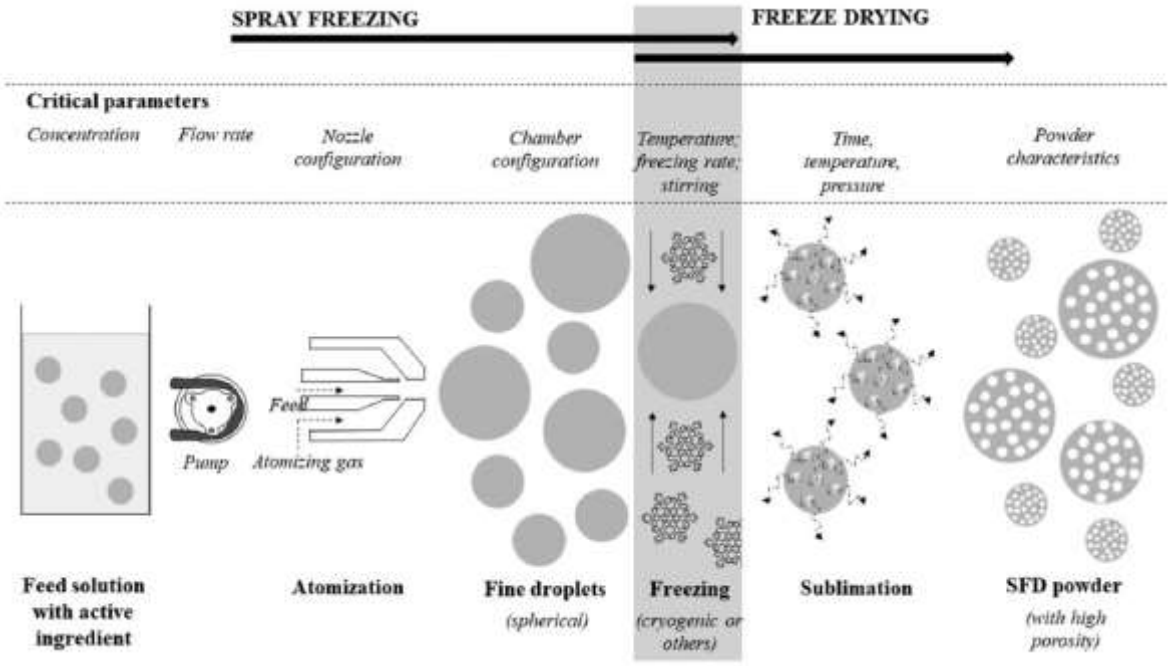

Figura 2: Processo di spray freeze-drying. Vishali *et al.*, 2019.

La prima fase del processo prevede l'atomizzazione della soluzione contenente il principio attivo. Tale atomizzazione può essere effettuata adoperando ugelli di più tipo (idraulici, ad ultrasuoni, pneumatici). Il congelamento della fase nebulizzata avviene in concomitanza con l'atomizzazione stessa attraverso l'immersione in un liquido criogenico (generalmente azoto) o nei vapori da esso emanati. Una volta atomizzata e congelata (spray-freeze), le particelle sferiche ottenute vengono essiccate (drying).

È evidente come la flessibilità e le caratteristiche peculiari nel controllo morfologico del prodotto e dei fenomeni di trasporto di massa e calore, rendano la SFD una delle tecnologie più promettenti per la realizzazione di un processo di liofilizzazione in continuo.

Motivazione della tesi

L'incapsulamento in fiala delle particelle sferiche generate durante la SFD, crea un letto impaccato con delle proprietà fisiche ben precise.

Lo scopo di questo lavoro è quello di sviluppare un modello matematico in grado di prevedere il comportamento del letto impaccato durante la fase di essiccazione della tecnica SFD.

Modelli per la descrizione della fase di essiccazione

In letteratura sono due i modelli principali già presenti che si propongono di descrivere accuratamente la fase di essiccazione della SFD. Questi sono il modello di Liapis e Bruttini (2009) ed il modello multiscala di Capozzi *et al.* (2019a).

Entrambi i modelli suddividono il letto impaccato di particelle in due domini distinti, uno detto "layer essiccato" dove non vi sono particelle congelate e l'altro detto "layer congelato" dove sono presenti le particelle congelate. Entrambi i modelli fanno uso di un sistema assialsimmetrico.

I due domini sono separati da un'interfaccia in grado di muoversi nello spazio durante la sublimazione. La teoria alla base dei modelli prevede che il flusso di vapore generato durante la liofilizzazione del layer congelato, attraversi l'interfaccia di sublimazione per giungere nel layer essiccato ed essere poi evacuato dalla testa della fiala grazie all'alto grado di vuoto. In Fig. 3 viene riportato uno schema dei fenomeni avvenenti nel letto impaccato durante l'essicazione.

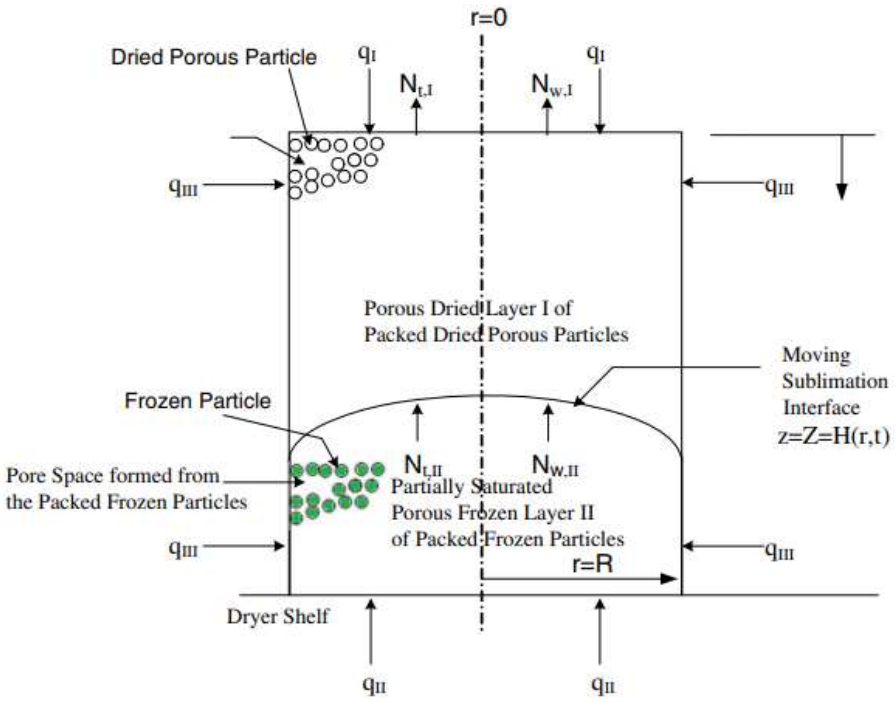

Figura 3: Essiccazione in fiala. Da Liapis e Bruttini (2009), immagine modificata.

Come mostrato in Fig. 3, il calore necessario per condurre l'essicazione può essere fornito in qualunque zona perimetrale della fiala.

Per il corretto funzionamento dei modelli è necessario un'attenta stima del grado di saturazione di ghiaccio a cui ogni particella nel letto è soggetto. In Fig. 4 vengono riportate tutte le possibili casistiche.

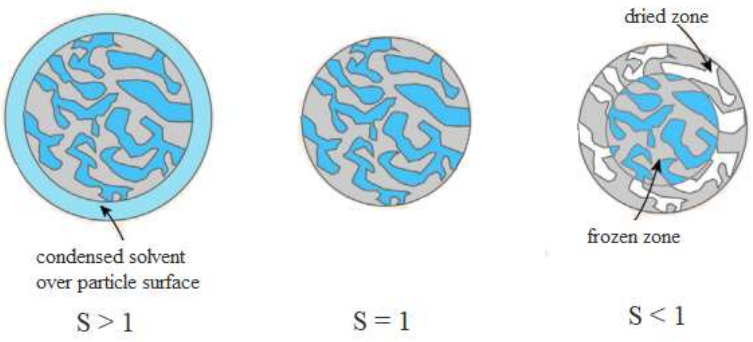

Figura 4: Illustrazione schematica dei possibili gradi di saturazione del ghiaccio. Da Capozzi *et al*. (2019a), immagine modificata.

In Fig. 4, la variabile S rappresenta il grado di saturazione di ghiaccio presente nella particella. È evidente come nel layer essiccato non sia possibile avere un valore di S diverso da 0. Da ciò è possibile dedurre che le proprietà chimico-fisiche in questo layer non variano nel tempo, a differenza del volume del dominio stesso che aumenta con il procedere dell'essiccamento. Di contro, le proprietà chimico-fisiche nel layer congelato cambiano localmente a seconda del grado di saturazione di ghiaccio ed il volume del dominio diminuisce nel tempo.

In teoria nel layer congelato, qualora il flusso di vapore generato attraversasse una zona in cui la concentrazione di vapore acqueo è maggiore della tensione di vapore, si potrebbe avere una condensazione del vapore con conseguente formazione di ghiaccio sulla superficie esterna delle particelle (Fig. 4, immagine a sinistra). Se tale fenomeno procedesse in maniera indiscriminata, si avrebbe un parziale (o totale) otturamento della struttura porosa del letto impaccato con conseguente perdita di permeabilità al vapore.

I risultati mostrati dai modelli, tuttavia, non corrispondono a quanto descritto precedentemente. Sono due i motivi principali che rendono dubbia la possibile applicazione di tali modelli. Il primo, è il salto netto da un layer congelato ad uno essiccato attraverso un'interfaccia di sublimazione mobile, senza la presenza di un gradiente a cavallo tra i due domini (Fig. 5). Il secondo, è la possibilità per il grado di saturazione di ghiaccio di raggiungere valori ben al di sopra di quello che annullerebbe la permeabilità del letto poroso al vapore (Fig. 6), senza che la condensazione locale sia bloccata. Da notare che i risultati mostrati in Fig. 6 sono stati ottenuti simulando il modello multiscala di Capozzi *et al.* (2019a).

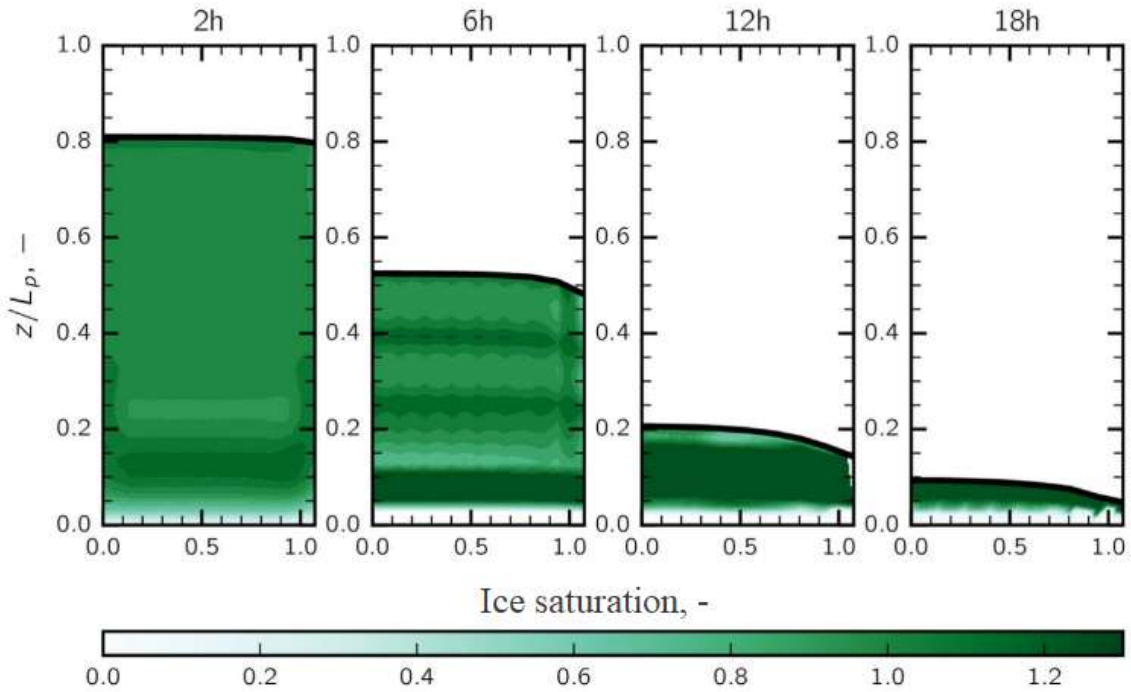

Figura 5: Evoluzione del grado di saturazione di ghiaccio. Capozzi *et al*. (2019b).

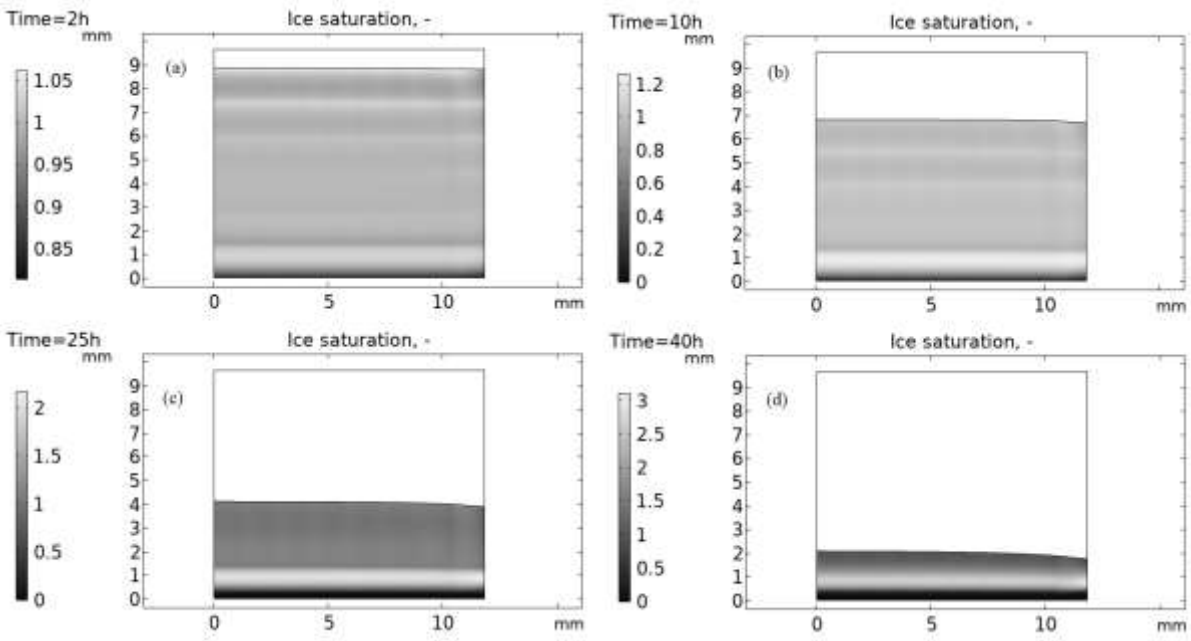

Figura 6: Grado di saturazione di ghiaccio, temperatura del ripiano a 238 K. Evoluzione senza blocco superiore. (a) Tempo 2 h, (b) Tempo 10 h, (c) Tempo 25 h, (d) Tempo 40 h.

Partendo dai risultati mostrati, è stato deciso di creare un modello ad interfaccia diffusa in grado di risolvere le difficoltà illustrate per i precedenti modelli.

La realizzazione del modello ad interfaccia diffusa ha richiesto lo sviluppo di un secondo modello descrivente la liofilizzazione di una singola particella. Da quest'ultimo è stato possibile ottenere informazioni a livello microscopico e trasferirle al modello del letto impaccato (scala macroscopica).

Modello a singola particella

Il modello è stato sviluppato per stimare un parametro detto costante cinetica di sublimazione (v_s). Tale parametro descrive la generazione di massa durante la sublimazione a livello microscopico e permette il passaggio di tale informazione al modello ad interfaccia diffusa.

In Fig. 7 è riportato uno schema della singola particella simulata.

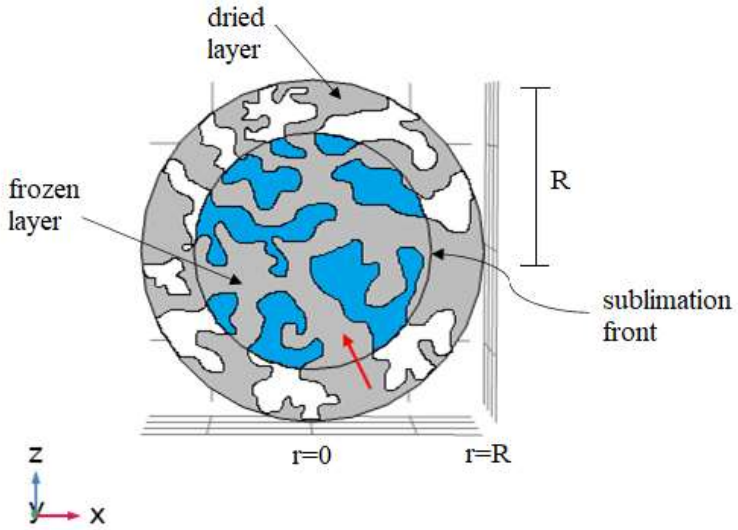

Figura 7: Rappresentazione schematica di una singola particella porosa.

La struttura del modello richiama quella utilizzata da Liapis e Bruttini (2009) per la simulazione del letto impaccato. La differenza sostanziale, rispetto ai modelli di Liapis e Bruttini (2009) e di Capozzi *et al.* (2019a), risiede nella possibilità per il flusso di vapore generato nel layer congelato durante la sublimazione di attraversare l'interfaccia di sublimazione mobile, condizione non prevista nei modelli preesistenti.

Per la valutazione della costante cinetica di sublimazione, sono state definite due espressioni. Dalla prima (Eq. 1), si ottiene un andamento della costante indipendente dalle proprietà fisiche della particella liofilizzata. Dalla seconda espressione (Eq. 2) si ottiene un andamento della costante cinetica che varia al variare della resistenza al trasporto di vapore offerta dal layer essiccato.

$$\nu_s = \frac{N_{w,interf}}{\left(\frac{p_{inter}}{RT_{inter}} - \frac{p_{vac}}{RT_{r=R_0}}\right) d_{dried} M_w} \tag{1}$$

$$\nu_s = \frac{N_{w,interf} S_{interf}}{\left(\frac{p_{inter}}{RT_{inter}} - \frac{p_{vac}}{RT_{r=R_0}}\right) M_w V_{ref}} \tag{2}$$

Il termine $N_{w,interf}$ presente in entrambe le espressioni rappresenta il flusso di vapore generato che attraversa l'interfaccia di sublimazione. La forza spingente per entrambe le equazioni è data dalla differenza tra la concentrazione di vapore all'interfaccia e la concentrazione di vapore sulla superficie della particella sferica. La pressione sulla superficie della particella è stata approssimata essere pari al grado di vuoto imposto nella camera durante la liofilizzazione. La pressione all'interfaccia, fissate le condizioni a contorno, è stata ricavata utilizzando l'equazione di Clausius-Clapeyron per l'acqua. Il termine M_w rappresenta il peso molecolare dell'acqua.

Nella prima valutazione della costante cinetica (Eq. 1) si è deciso di rendere i valori ottenuti indipendenti dalla resistenza offerta al trasporto di massa inserendo al denominatore il termine d_{dried}. Tale grandezza rappresenta lo spessore dello strato essiccato che si forma nella particella durante il processo.

Nella seconda valutazione della costante cinetica (Eq. 2) è stato deciso di adottare un volume di riferimento V_{ref}. Il software usato per le simulazioni utilizza un metodo agli elementi finiti. Di conseguenza, il volume di riferimento deve necessariamente tener conto non solo della singola particella, ma anche di ciò che viene descritto dal volume dell'elemento finito. Tale aspetto è stato considerato inserendo la porosità del letto impaccato nella definizione del volume di riferimento (Eq. 3).

$$V_{ref} = \frac{\frac{4}{3}\pi R_0^3}{1 - \varepsilon_{pb}} \tag{3}$$

L'andamento indipendente della costante cinetica (Eq. 1) dal variare delle proprietà fisiche della particella durante la simulazione è una descrizione sufficientemente accurata di ciò che avviene a livello microscopico qualora le particelle fossero di dimensioni molto contenute (dell'ordine dei nanometri). Se la dimensione delle particelle crescesse, la resistenza offerta dallo strato essiccato generato contribuirebbe pesantemente al trasporto di vapore nella particella stessa. In quest'ultimo caso, l'andamento valutato attraverso la seconda espressione (Eq. 2) garantirebbe risultati più accurati.

La costante cinetica valutata attraverso il modello a singola particela rappresenterà un parametro fondamentale del modello ad interfaccia diffusa per la descrizione della generazione di massa nel letto impaccato.

Modello ad interfaccia diffusa

Rispetto ai modelli già esistenti per la descrizione della fase di sublimazione di un letto impaccato, il fronte di sublimazione mobile è stato rimosso. Il letto è stato schematizzato attraverso un singolo dominio in cui le proprietà fisiche cambiano con il grado di saturazione di ghiaccio. L'interfaccia non è più imposta a priori, ma ottenuta da un meccanismo diffusivo.

È stato adottato un sistema bidisperso per descrivere l'intero letto impaccato. Il modello è stato sviluppato assumendo che una quantità controllata di gas inerte (azoto) venga inviata al sistema per manipolare la pressione della camera.

In Fig. 8 è mostrata una rappresentazione schematica del letto durante la liofilizzazione.

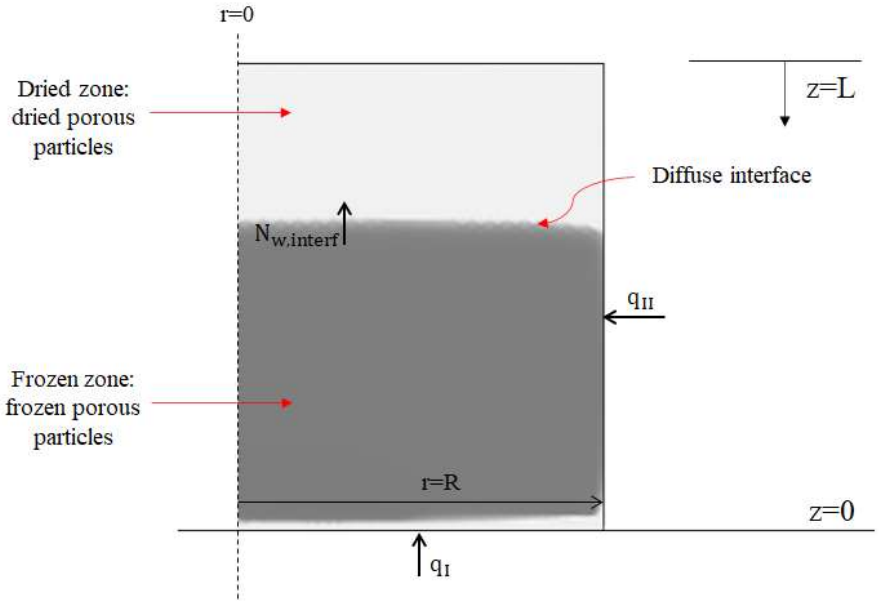

Figura 8: Rappresentazione schematica del letto impaccato durante la liofilizzazione, modello ad interfaccia diffusa.

Il grado di saturazione di ghiaccio (Eq. 4), fondamentale per la descrizione delle proprietà fisiche del letto impaccato e dell'avanzamento della sublimazione, è definito come il complemento ad uno del rapporto tra la quantità di acqua che cambia fase durante l'essiccazione e la quantità totale di acqua che deve essere sublimata.

$$S = 1 - \frac{C_{w,int}}{C_{w,i}} \tag{4}$$

Una volta definito il grado di saturazione, è stato possibile ottenere le proprietà fisiche del letto attraverso una media pesata in cui il peso è *S*, tenendo conto dell'ipotesi di sistema bidisperso. Di seguito viene riportata la definizione della porosità totale del letto impaccato (Eq. 5).

$$\varepsilon_{tot} = \begin{cases} \varepsilon_{pb} & \text{for } S < 1 \\ \varepsilon_{pb} + \left(1 - \varepsilon_{pb}\right)\varepsilon_p(1 - S) & \text{for } S \geq 1 \end{cases} \tag{5}$$

Nell'Eq. 5, i termini ε_{pb} e ε_p rappresentano rispettivamente la porosità del letto e della singola particella. Dalla definzione della porosità totale del letto è facile notare come esista un valore critico di *S* tale per cui la stessa porosità viene annullata. Ciò rappresenta il caso in cui la condensazione del vapore precedentemente generato è tale da ostruire localmente la struttura porosa del letto impaccato. Un valore nullo della porosità totale genera conseguentemente un annullamento della permeabilità al vapore del letto (il vapore generato non è in grado di attraversare la struttura ostruita del letto). In questa condizione, il trasporto di massa del vapore (Eq. 6) si annulla automaticamente finché lo stato termodinamico locale del sistema non permetterà nuovamente la generazione di materia a partire dai layer di ghiaccio ostruenti i pori del letto.

$$\frac{\partial(\varepsilon_{tot} C_w)}{\partial t} = -\boldsymbol{\nabla} \cdot \boldsymbol{N_w} + G_w \tag{6}$$

Le conseguenze derivanti dalla definizione della porosità (Eq. 5) sono in netto contrasto con i risultati ottenuti dai modelli precedentemente presentati, in cui il grado di saturazione del ghiaccio può superare il valore critico senza che il trasporto di vapore sia fermato.

Una volta definito il grado di saturazione è stato possibile esprimere il termine di generazione di massa nel letto durante la liofilizzazione (Eq. 7).

$$G_w = \begin{cases} \left(\frac{p_w^{sat}}{RT} - C_w\right) \nu_s & \text{se } \left(\frac{p_w^{sat}}{RT} - C_w\right) \geq 0 \\ \left(\frac{p_w^{sat}}{RT} - C_w\right) \nu_c & \text{se } \left(\frac{p_w^{sat}}{RT} - C_w\right) < 0 \end{cases} \tag{7}$$

Il termine C_w rappresenta la concentrazione di vapore acqueo presente localmente nel letto, ottenibile dall'equazioni di trasporto di massa del vapore. Il termine è direttamente influenzato dal grado di saturazione di ghiaccio presente localmente. La differenza tra la concentrazione C_w e la concentrazione di saturazione termodinamica (ottenibile dall'equazione di Marti, 1993) rappresenta la quantità di moli per metro cubo che sublimano o condensano durante il processo. Tale quantità è stata moltiplicata per la costante cinetica (di condensazione o di sublimazione) in base a quale fenomeno sia termodinamicamente favorito.

Da notare che, a differenza della costante cinetica di sublimazione, la costante di condensazione non è stata valutata, ma è stata soggetta di un'analisi parametrica per stabilire l'impatto che questa avesse sulle simulazioni e quale valore rappresentasse meglio i dati sperimentali.

Tutte le simulazioni (sia per il modello a singola particella che per il modello ad interfaccia diffusa) sono state eseguite utilizzando una licenza accademica del software COMSOL. Tale programma, come anticipato precedentemente, utilizza un sistema agli elementi finiti.

Risultati del modello a singola particella

In Tab. 1 sono riportati i parametri di input del modello che discriminano le diverse simulazioni condotte.

Tabella 1: Parametri del modello a singola particella.

Parametro	Valore	Unità	Descrizione
B_0	$d^2_{pore}/180 \cdot d^3_{pore}/(1-\varepsilon_p)^2$	m²	Permeabilità della particella
d_{pore}	$2 \cdot R_0/X$	m	Diametro dei pori nella particella
R_0	1.62E-05	m	Raggio della particella
ε_p	0.95	-	Porosità della particella

Il parametro X rappresenta il rapporto tra il diametro della sfera ed il diametro dei pori nella particella. Le simulazioni condotte sono state discriminate in base al valore di X. Dalle osservazioni sperimentali, è stato possibile affermare che tale parametro assume un valore compreso tra 30 e 100. È stato deciso di utilizzare diversi possibili valori, elencati in Tab. 2.

Il diametro delle particelle utilizzato è stato ricavato sperimentalmente dalla Dott.ssa M. Adali. Oltre al diametro sperimentale, è stato deciso di utilizzare un ulteriore valore di 500 µm per investigare quale fenomeno sia controllante il trasporto di massa durante l'essiccazione del letto impaccato.

In Tab. 2 sono riportate le sigle con cui sono state etichettate alcune delle simulazioni condotte, insieme ai valori di X e del diametro delle particelle rispettivamente utilizzati.

Tabella 2: Etichettatura delle simulazioni.

Rapporto	Diametro	Etichetta
X=1000	$R_0 = 16.2$ µm	SP.1000
X=100	$R_0 = 16.2$ µm	SP.100
X=60	$R_0 = 16.2$ µm	SP.60
X=30	$R_0 = 16.2$ µm	SP.30
X=1000	$R_0 = 250$ µm	SP250.1000
X=100	$R_0 = 250$ µm	SP250.100

I risultati mostrati in Fig. 9 sono stati estratti dalle simulazioni utilizzando la prima defezione (Eq. 1) di costante cinetica di sublimazione.

Come anticipato in precedenza, la definizione usata permette di ottenere una costante indipendente dalle proprietà fisiche della particella che si sta essiccando. Ciò si evince dall'asintoto raggiunto dai profili sopra riportati una volta essiccati i primi strati superficiali del granulo.

Il parametro v_s nel modello ad interfaccia diffusa, facente riferimento all'Eq. (1), è stato settato costante e pari all'asintoto raggiunto dai profili in Fig. 9.

In Fig. 10 sono riportati i profili ricavati dall'Eq. (2).

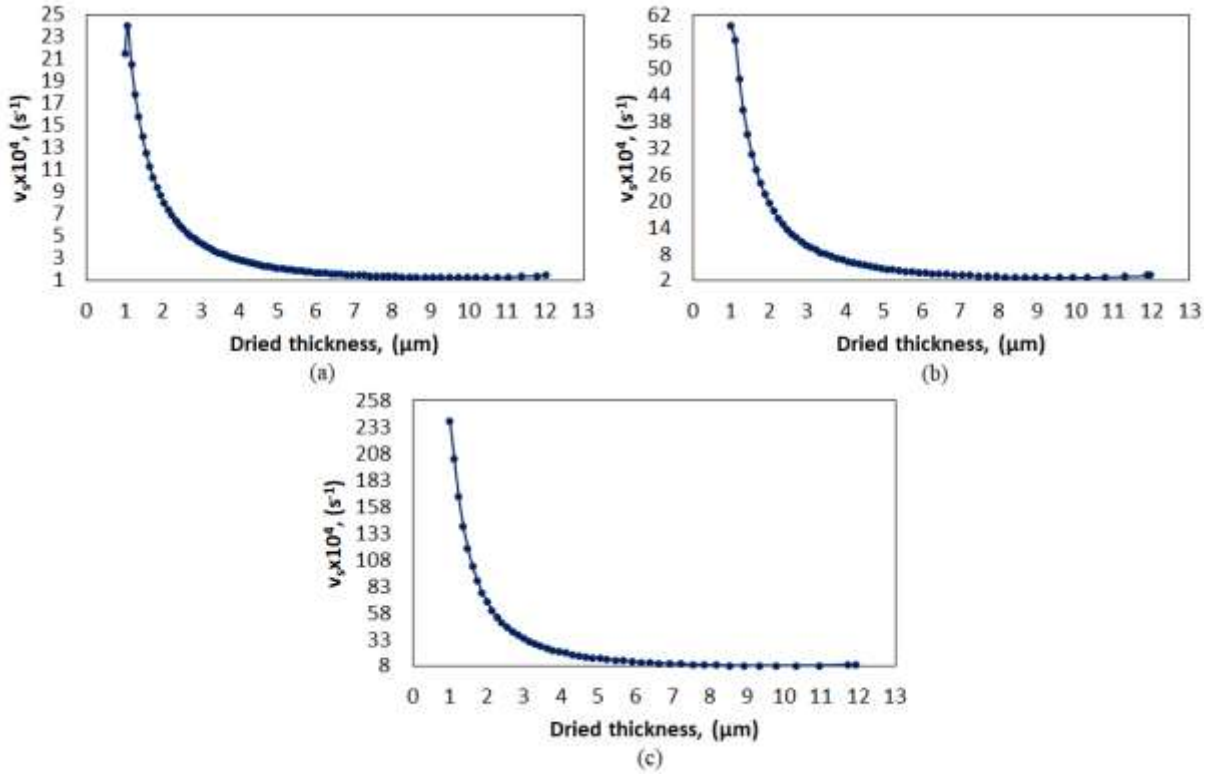

Figura 9: (a) SP.100, (b) SP.60, (c) SP.30 costante cinetica di sublimazione per Eq. (1).

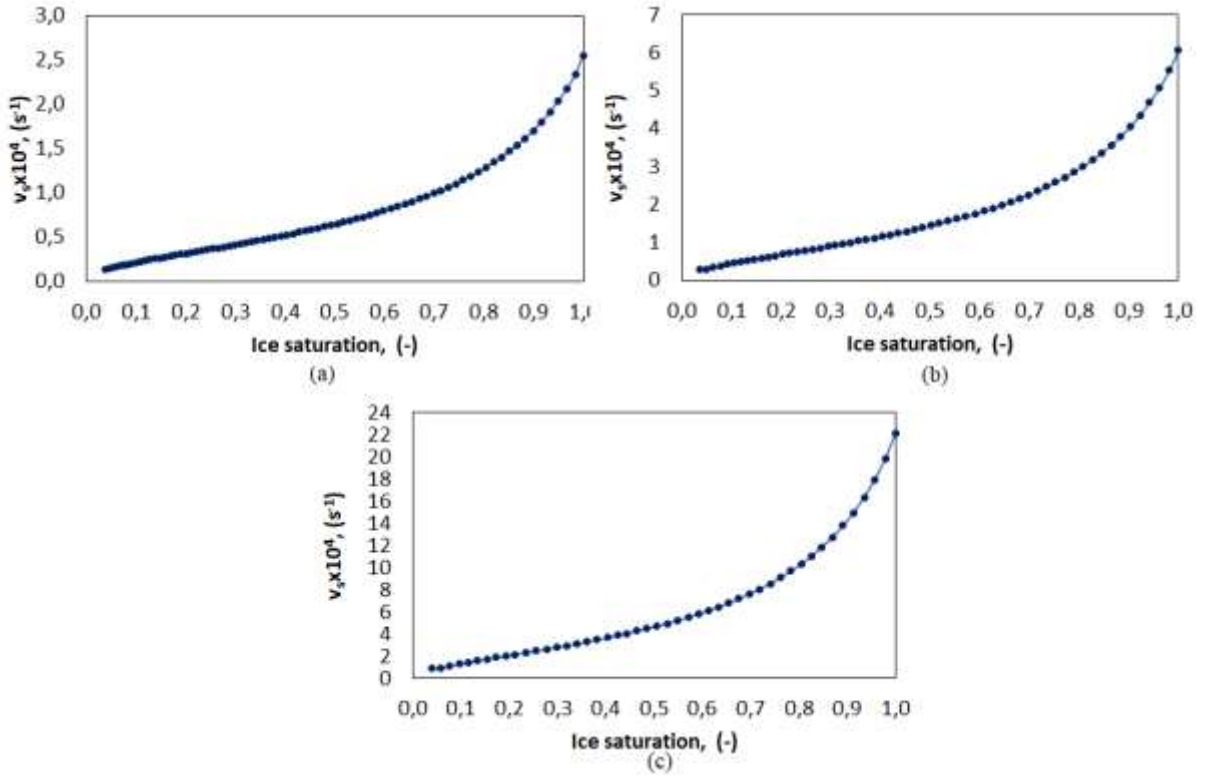

Figura 10: (a) SP.100, (b) SP.60, (c) SP.30 costante cinetica di sublimazione per Eq. (2).

A differenza del caso precedente, attraverso l'utilizzo dell'Eq. (2) sono stati ottenuti profili per la costante di sublimazione il cui andamento dipende dal grado di saturazione di ghiaccio (ovvero, la quantità di ghiaccio residua) all'interno della particella.

Gli andamenti mostrati in Fig. 10 sono stati direttamente inseriti nelle simulazioni del modello ad interfaccia diffusa per la descrizione del parametro ν_s. Per un valore di *S* nullo, la costante cinetica è stata posta uguale a 0. Per un valore di *S* maggiore di 1, la costante cinetica è stata posta essere costante e pari al valore raggiunto per il valore di *S* pari a 1.

Inoltre, dalle simulazioni del modello a singola particella si è potuto evincere come aumentando il diametro dei pori all'interno della particella, si passi da un meccanismo di controllo di trasporto di massa ad un meccanismo di controllo di trasporto di calore. Tale fenomeno è stato collegato alla minore resistenza al trasporto di materia offerta dalla particella all'aumentare del diametro dei pori, con conseguente aumento della permeabilità al vapore generato.

Risultati del modello ad interfaccia diffusa

Tutte le simulazioni sono state condotte avendo come fonte primaria di calore il ripiano su cui poggia la fiala contenente il letto impaccato. La temperatura del ripiano è stata impostata pari a 10°C fino a 36 ore di essicamento, per poi innalzarsi attraverso un gradino istantaneo alla temperatura di 20 °C per il tempo operativo rimanente.

Le simulazioni condotte aventi un valore di ν_s costante sono state etichettate con le diciture DIA.# e DINA.#, in base alle condizioni al contorno per il trasporto di calore (rispettivamente adiabatiche o non adiabatiche) imposte sulla superficie del letto impaccato.

Le simulazioni aventi un valore di ν_s che varia con il grado di saturazione del ghiaccio sono state etichettate DI.#. Per tali simulazioni, le condizioni al contorno per il trasporto di calore sono sempre state imposte non adiabatiche.

In tutte le etichettature, il simbolo # è composto da due numeri separati da un punto, indicanti rispettivamente il valore del parametro X nella simulazione del modello a singola particella da cui deriva il corrispettivo valore di ν_s, ed il valore di costante cinetica di condensazione utilizzato.

In Fig. 11 è riportato un esempio della distribuzione di *S* ottenuta con il modello ad interfaccia diffusa.

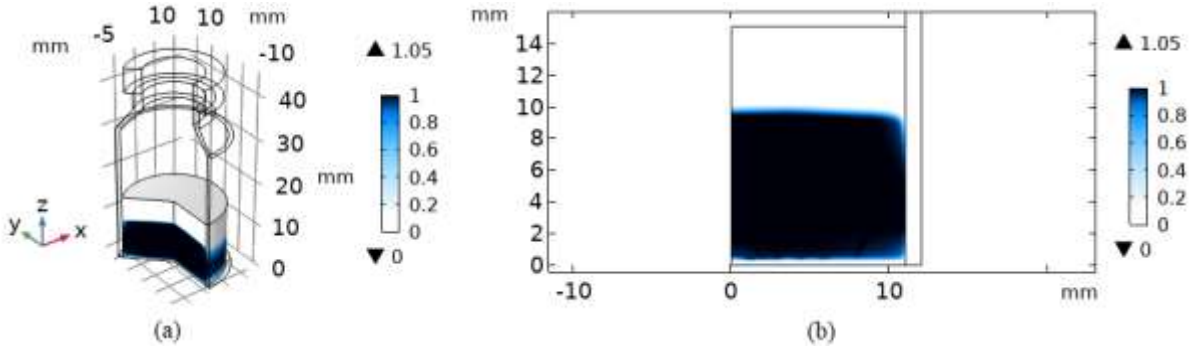

Figura 11: (a) vista 3D, (b) vista 2D della distribuzione della saturazione di ghiaccio nel letto impaccato. Tempo di essiccamento pari a 5h. Modello DI.60.100.

Dalla Fig. 11 è possibile osservare come le interfacce di sublimazione non siano rappresentate attraverso un salto netto tra il layer essiccato e layer congelato, bensì attraverso un gradiente.

In Fig. 12 è riportata la distribuzione di concentrazione d'acqua all'interno del letto impaccato, in cui le frecce nere rappresentano il flusso di materia. È possibile notare come il flusso attraverso l'interfaccia sia possibile.

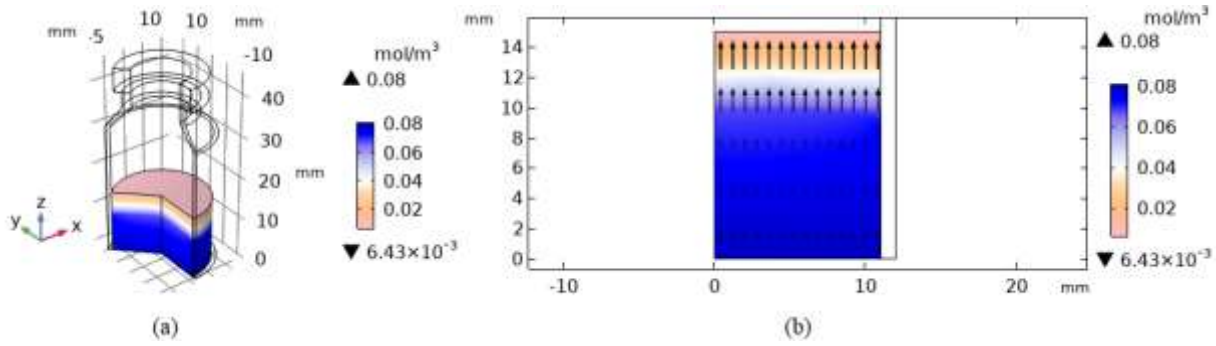

Figura 12: (a) vista 3D, (b) vista 2D della distribuzione di vapore acqueo nel letto impaccato. Tempo di essiccamento pari a 5h. Modello DI.60.100.

Aumentando il diametro dei pori, si ottiene una costante cinetica di sublimazione che aumenta anche di svariati ordini di grandezza. Tale fenomeno, descrive un aumento del numero di moli di vapore acqueo che si potrebbero generare durante l'essiccamento del letto, ma altresì descrive un aumento del quantitativo di calore richiesto affinché tali moli possano essere generate. Avendo condotto le simulazioni fornendo la stessa quantità di calore, è stato ottenuto un aumento del tempo di essicamento all'aumentare del diametro dei pori all'interno delle particelle.

In Fig.13 sono riportati i risultati ottenuti per le simulazioni DIA.#. La media riportata è stata ricavata prendendo come riferimento il volume del letto impaccato.

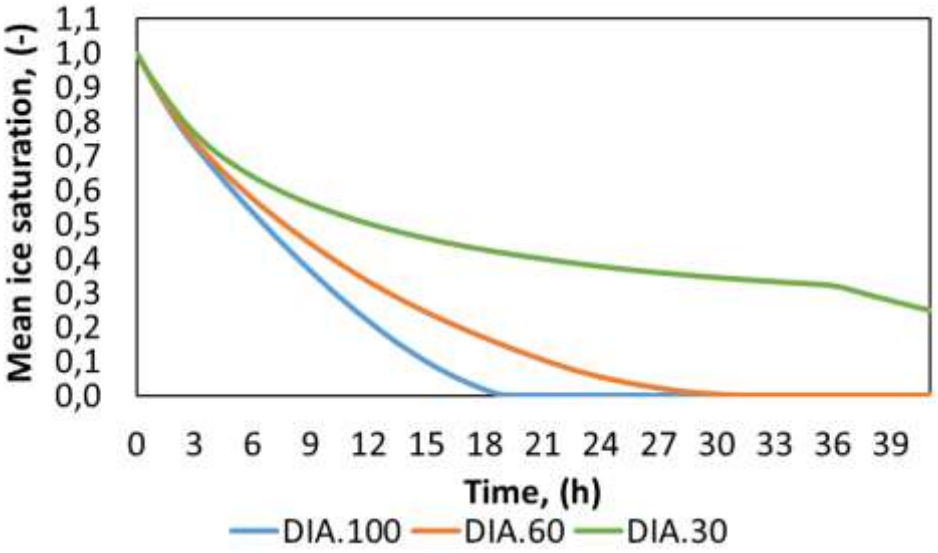

Figura 13: Andamento del grado di saturazione di ghiaccio medio durante l'essicamento. Modelli DIA.#.

Per la simulazione DIA.100.1, monitorando l'andamento di *S* in tre punti del letto impaccato ad altezze diverse, sono stati ottenuti gli andamenti riportati in Fig. 14.

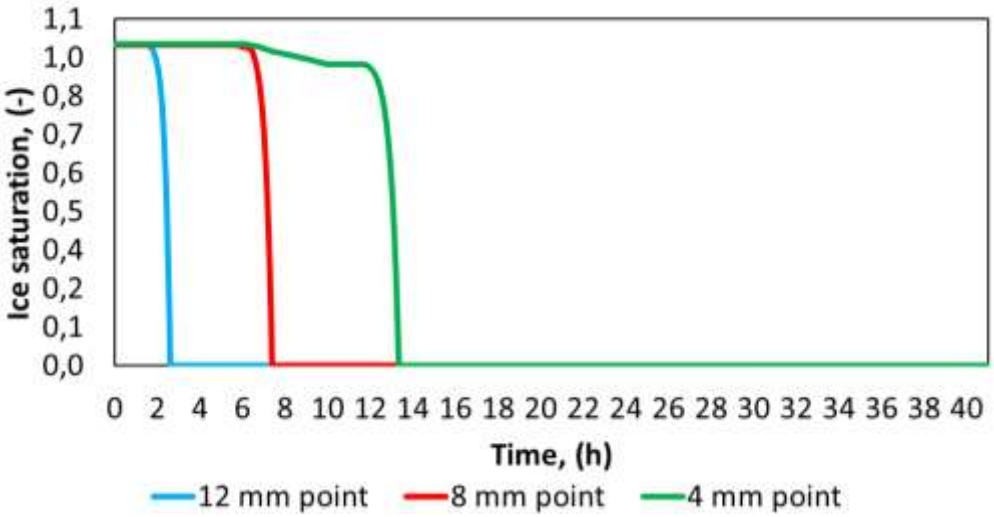

Figura 14: Grado di saturazione di ghiaccio per tre punti ad altezze differenti. Modello DIA.100.1.

Come si evince dall'istantanea discesa del profilo da valori prossimi ad 1 fino ad un valore nullo, il meccanismo di trasporto di massa controllante è la resistenza offerta dal letto impaccato. Il vapore generato non incontra un'eccessiva resistenza da parte delle particelle e, una volta raggiunte le condizioni termodinamiche tali per cui si verifichi l'essiccamento dei granuli, il ghiaccio viene istantaneamente sublimato.

In Fig. 15 è raffigurato il profilo di temperatura media nel letto impaccato ottenuto per la simulazione DIA.100.1. Come si evince dall'andamento riportato, il meccanismo complessivo di trasporto controllante risulta essere il trasporto di calore. Il letto, comincia la sua essicazione e raggiunge un valore medio di *S* nullo prima di raggiungere la temperatura del ripiano riscaldante.

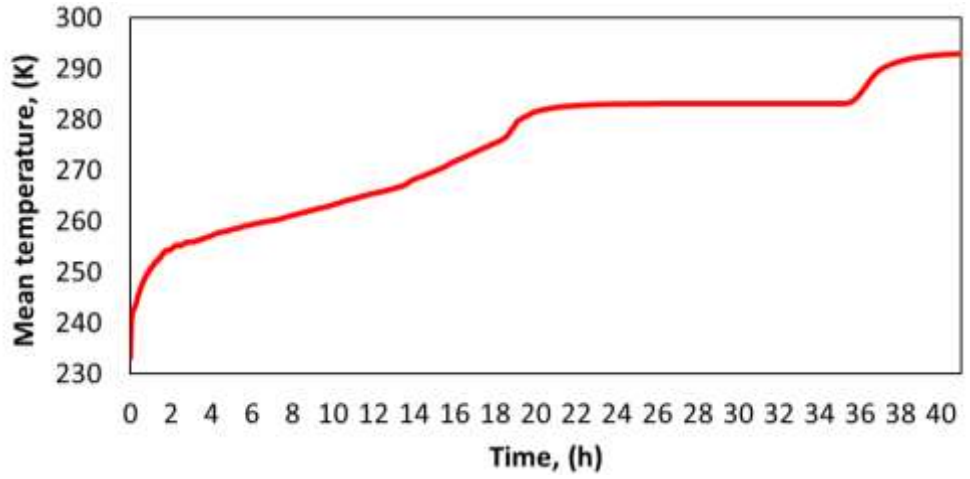

Figura 15: Profilo di temperatura media nel letto impaccato. Modello DIA.100.1.

In Fig. 16 è riportato un confronto tra i risultati ottenuti con le simulazioni DI.60.1 e DIA.60.1.

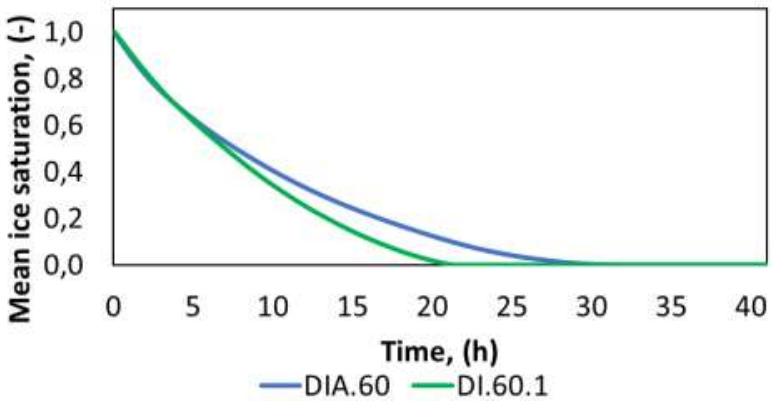

Figura 16: (blu) DIA.60.1, (verde) DI.60.1, andamento del grado di saturazione di ghiaccio medio durante l'essicamento.

Il tempo d'essicamento minore fatto registrare per la simulazione DI.60.1 è dovuto alla formazione di un terzo fronte di sublimazione. Tale fronte è generato dal calore proveniente dal vetro della fiala che, grazie alle condizioni non adiabatiche sulla superficie del letto, si riscalda assorbendo la radiazione proveniente dai ripiani superiori. Le temperature superiori raggiunte dal vetro della fiala rispetto a quelle presenti nel letto impaccato generano un terzo fronte di sublimazione grazie ad un meccanismo di trasporto conduttivo.

In Fig. 17 è riportato un confronto tra le distribuzioni di temperatura nei letti impaccati per le due simulazioni (DI.60.1 e DIA.60.1). Le frecce nere, del tutto assenti per la distribuzione corrispondente alla simulazione DIA.60.1, indicano il flusso di calore proveniente dal vetro della fiala e trasmesso al letto per conduzione.

I tempi di essiccamento fatti registrare dalle simulazioni DI.# sono stati minori rispetto alle altre simulazioni, a parità del diametro dei pori all'interno delle particelle. Tale fenomeno è riconducibile al minore calore richiesto per la sublimazione delle particelle al diminuire del grado di saturazione di ghiaccio. Per le simulazioni DIA.# e DINA.#, il calore richiesto per sublimare un granulo rimane costante a parità di forza spingente, anche qualora il valore di S diminuisse durante l'essiccamento.

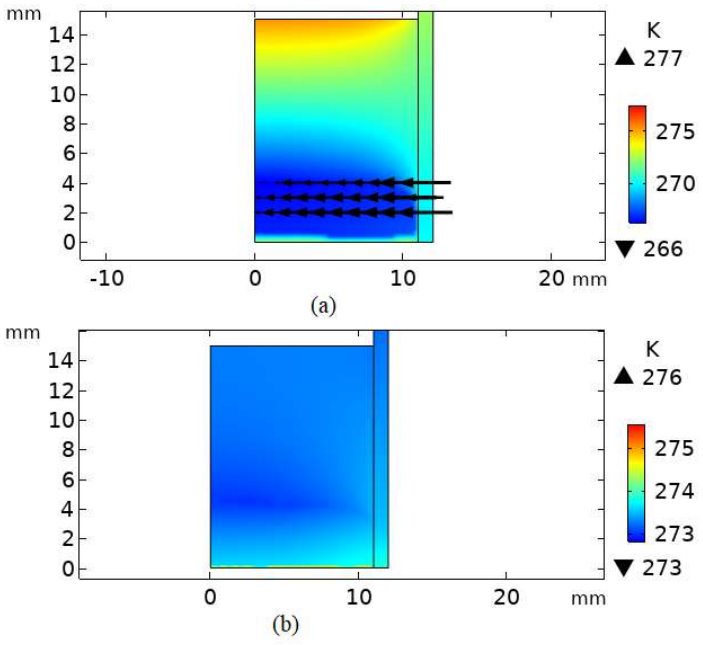

Figura 17: (a) DI.60.1, (b) DIA.60.1. Tempo di essiccamento pari a 15h.

Un ultimo aspetto analizzato è stato la variazione del meccanismo controllante il trasporto di massa nel letto al variare delle proprietà fisiche delle particelle. In particolare, è stato deciso di analizzare il comportamento del letto impaccato al variare del diametro delle particelle e del parametro X del modello a singola particella.

In Fig. 18 è riportato l'andamento del grado di saturazione di ghiaccio per tre punti ad altezze differenti per la simulazione DI250.100.100, in cui è stato utilizzato il valore di v_s derivante dal modello a singola particella SP250.100.

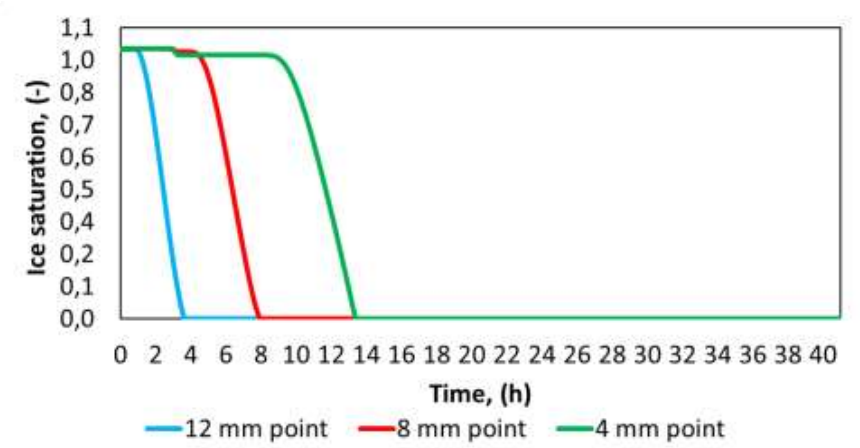

Figura 18: Grado di saturazione di ghiaccio per tre punti ad altezze differenti. Modello DI250.100.100.

A differenza dei profili riportati in Fig. 14, la transizione da valori di *S* prossimi a 1 ad un valore nullo non è istantanea ma richiede delle ore.

Tale fenomeno è sintomo che la resistenza al trasporto di massa offerta dalla particella aumenta rispetto al caso precedente, a causa del maggiore diametro dello strato essiccato che si forma nel granulo durante l'essicamento.

Per le simulazioni in cui, oltre ad accrescere il diametro delle particelle si riduce notevolmente il diametro dei pori all'interno dei granuli, il meccanismo controllante il trasporto di materia diviene la resistenza offerta dalla particella. Il vapore generato incontra difficoltà ad essere evacuato dai granuli, mentre fluisce con più facilità attraverso il letto. In Fig. 19 sono riportati gli andamenti ottenuti per la simulazione DI250.1000.100.

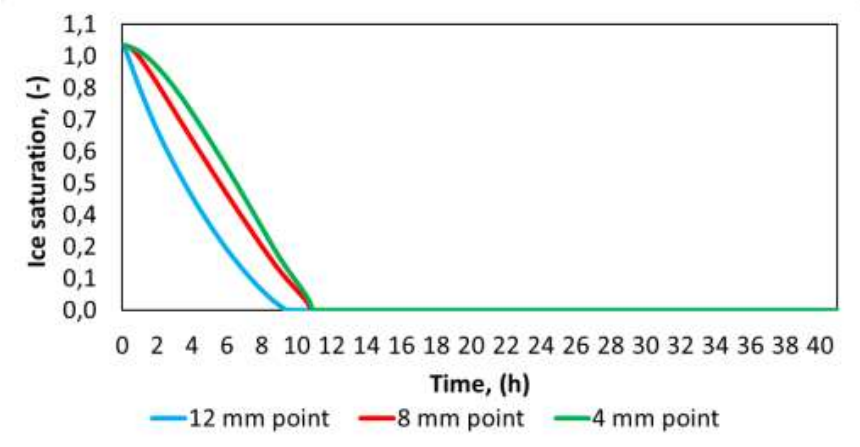

Figura 19: Grado di saturazione di ghiaccio per tre punti ad altezze differenti. Modello DI250.1000.100.

Come è possibile notare dalla Fig. 19, l'essicamento dei granuli richiede anche fino a 12h operative. Quando il meccanismo controllante il trasporto di materia diviene la resistenza offerta dal granulo, la distinzione tra layer essiccato e layer congelato perde di significato, in quanto la distribuzione di ghiaccio coinvolge tutto il letto impaccato come mostrato in Fig. 20.

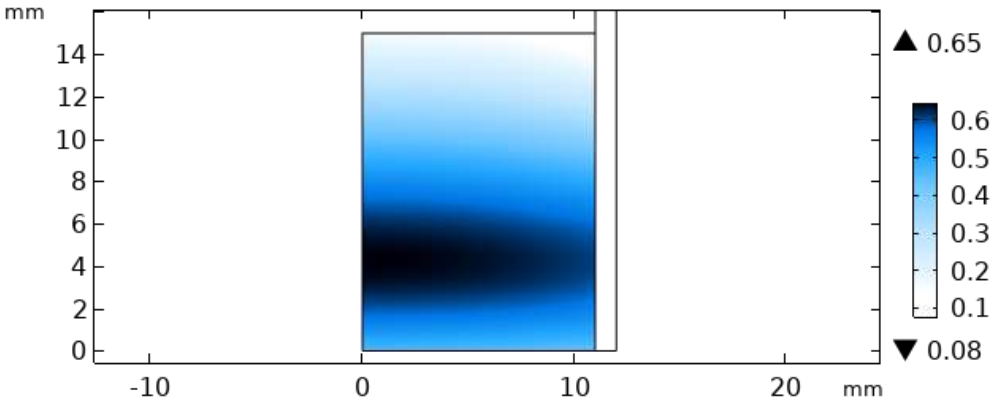

Figura 20: DI250.1000.100, distribuzione del grado di saturazione di ghiaccio nel letto impaccato. Tempo di essiccamento pari a 5h.

Conclusioni

Lo sviluppo di un modello ad interfaccia diffusa ha permesso di superare le difficoltà e gli andamenti non rispecchianti la fisica del sistema, riscontrati dai modelli ad interfaccia mobile precedentemente sviluppati.

È stato dimostrato che una maggiore permeabilità delle particelle al vapore generato non è sempre legata ad un tempo di essicamento del letto impaccato più basso, a causa del calore più elevato richiesto per consentire la sublimazione delle particelle. La possibilità di controllare la morfologia e le dimensioni dei prodotti attraverso la SFD potrebbe facilitare il controllo di tale aspetto in un ipotetico processo continuo.

Il comportamento dei meccanismi di trasporto è stato studiato confrontando diverse proprietà fisiche delle particelle. Si è ottenuto che una variazione della dimensione delle particelle può avere un enorme impatto sul meccanismo di controllo del trasporto di massa, con la resistenza delle particelle che diviene più importante all'aumentare del diametro del granulo.

Quest'ultimo aspetto può avere un enorme impatto sulla progettazione di un processo continuo a causa del diverso comportamento che i vari principi attivi possono avere con diverse concentrazioni di vapore. Se il principio attivo richiedesse di essere essiccato rapidamente senza tener conto della concentrazione locale di vapore, dovrebbe essere scelta una situazione in cui la resistenza al trasporto di massa attraverso la particella è il meccanismo di controllo. Invece, se il principio attivo è fortemente denaturato dal vapore acqueo, dovrebbe essere scelta una configurazione in cui i flussi vengono evacuati dalla particella non appena vengono generati (cioè, il meccanismo di controllo è la resistenza attraverso il letto imballato).

Lo sviluppo di un modello matematico in grado di descrivere i fenomeni fisici che si verificano durante l'essiccazione del letto impaccato è fondamentale per l'applicazione in una produzione continua delle diverse peculiarità offerte dalla SFD. Ad esempio, una possibile applicazione riguarderebbe lo studio di un campione di principi attivi e la loro denaturazione durante la SFD, ottimizzando le attrezzature utilizzate attraverso l'uso del modello ad interfaccia diffusa. L'utilizzo del modello matematico sarà fondamentale per accoppiare le esigenze della manifattura continua con gli standard farmaceutici.

Index

1. Introduction

1.1 Continuous manufacturing in the pharmaceutical industry

For over 50 years, the pharmaceutical industry has intensified and optimized the use of batch technology to answer the increasing demand of drugs. However, the use of batch processes brings to more probability in less quality end-product and higher inefficiency.

Batch processing requires multiple process steps which lead to hold times. One of the greatest problems in the pharmaceutical industry is the risk of degradation of the environment sensitive products during these intervals. Moreover, the length of these hold times could be around weeks or months which leads to large footprint equipment and higher capital costs.

Discontinuous processes are known to have very strict flexibility and wide end-product quality variance. Padmanabhan (2017) highlighted how these inefficiencies costed to the pharmaceutical industry about $50 billion/year. Also, strict flexibility causes the transition from new life science research discoveries to efficacious products to be much slower.

Continuous manufacturing may be a possible solution to rise the efficiency and the end-product quality. Continuous processes are easier to control and improve the uniformity of the quality of the final products, eliminating the hold times. Equipment would be much smaller, cutting down capital costs and the consume of large real estate. Furthermore, the possibility to optimize the logic control of the process would lead to a lower risk of failure and human error.

Continuous processes have a higher flexibility to better respond to production changes. The transition from laboratory scale to industrial scale would be much faster and the reduction of stockpiles would lead to lower wasting risk. A large number of drug products could be produced personalized or on demand.

Another important point is the possibility to monitor the product quality on-line without relying on the off-line sampling phase needed in batch mode. This could save major amount of product volumes that batch manufacturing is currently wasting due to the rigid pharmaceutical constrains.

The greatest problem to shift from batch to continuous manufacturing is the expensive cost that the transition would require. The hesitation of the regulatory environment makes the investment not a priority for major companies. According to Badman *et al.* (2019) some possible solutions to help the shifting would be taxes incentives and regulatory incentives that affect the product approval time.

Although the transition is still a challenge, some researchers and authorities have started to carefully look at the continuous manufacturing. U.S. Food & Drug Administration (FDA) is partnering with other authorities to fund the research and help industry to implement innovative technologies like the continuous ones (Lee, 2017).

The continuous production of active pharmaceutical ingredient (API) with small molecular dimension is no longer seen as a future technology. Mascia *et al.* (2013) presented the first integrated continuous manufacturing plant to produce the aliskiren hemifumarate. Starting from a chemical intermediate the authors were able to realize final tablets that meet drug product quality specifications. The number of units was reduced from 21 in batch mode to 14 in continuous mode, replacing steps such as mixing, granulation and compression with a single extrusion device. An automated control system guaranteed the final product quality, and the residence time was about one order of magnitude lower than the batch manufacturing. Also, tablets presented some better properties such as a faster dissolution.

Dream (2017) compared the continuous production of “Blue Sky” (API) to the batch production. He found a great reduction in capital and operative costs (from 25% to 60%) and a massive reduction of the equipment footprint (up to 90%).

Biopharmaceutical manufacturing is currently facing his major effort to shift from batch to continuous technology. A lot of different aspects must be considered compared to classical pharmaceutical manufacturing due to the presence of cells and their lifetime cycles. The days required to culture growth and the high stress sensitive are delaying the transition.

Dream (2017) highlighted how continuous manufacturing can work with higher cell density to lead to higher volumetric production rates at the same culture daytime. Moreover, the possibility to design a multi-protein facility plant, minimize the microbiological issues and realize a steady state metabolism process are a strong driving force towards the change. According to the author, new technologies should implement the feature to work with a continuous flow from the bioreactor to the capture and perform a continuous capture.

One of the most important steps in the (bio)pharmaceutical industry is the drying process. Currently batch manufacturing and all the technologies presented have a drying step which remove the excess moisture.

Lyophilization is one of the best methods to dry heat sensitive products and obtain the needed quality. Although this technology was successfully shifted from batch to continuous in food industry, a lot of regulatory obstacles and process standards problems are delaying the transition in the pharmaceutical industry.

1.2 *Examples of continuous units for the pharmaceutical industry*

1.2.1 Continuous crystallization

Most of the APIs in the pharmaceutical industry are crystals produced by batch technologies. To improve the productivity of the entire plant, a lot of studies were performed to speed up shifting to continuous crystallization step. According to Schaber *et al.* (2011), a continuous unit where the mother liquid is continuously flowed, and the slurry is continuously withdrawn could save from 9% to 40% of the cost production.

Actually, there are two types of continuous crystallizer: the mixed-suspension mixed-product removal (MSMPR) where well-mixed conditions can be adopted in the design, and the continuous tubular crystallizer. The first type of crystallizer could easily manage the transition from a batch to a continuous step; it provides low maintenance costs, but may lead to unstable process behaviour and it is hard to scale-up. The second type of crystallizer has higher efficiency than MSMPR; it has a narrower residence time distribution (RTD), but usually can be affected by fouling and requires higher maintenance costs.

1.2.1.1 MSMPR crystallizer

The MSMPR (Fig. 1.1) is assumed to be well-mixed. The driving force of the process is the supersaturation generated during the flow of the solution through the series of stirred tanks. Usually, a main goal in the design of this type of unit is to guaranty the highest possible degree of supersaturation to achieve the best crystal surface in the crystallizer.

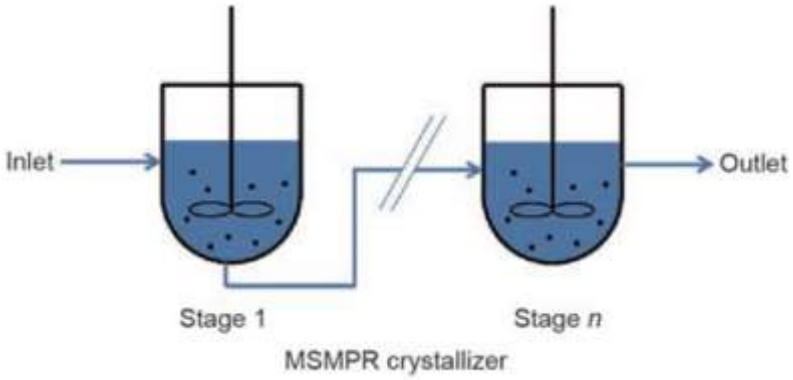

Figure 1.1: MSMPR crystallizer. Zhang *et al*., 2017.

The yield reached with a single pass MSMPR is lower than batch technology. To rise the productivity three main solutions could be adopted. Quon *et al.* (2012) shown how extending the resident time in the MSMPR production of aliskiren hemifumarate could improve the yield up to 93.6%. However, this method reduced the purity and the productivity. Another method is to upstream recycle the mother liquid. Although the yield can rise (Alvarez *et al.*, 2011) this method cannot deal with temperature sensitive APIs, and it can modify the solution composition. Ferguson *et al.* (2014) demonstrated that one of the best solutions to increase the yield without sacrificing the purity is a solvent nanofiltration membrane before the mother liquid recycling.

The proper design of residence time parameter in the MSMPR could also meet size requirements to have a fast drug delivery (small crystals size distribution) or an enhanced downstream process efficiency (large crystals size distribution). Vetter *et al.* (2014) demonstrated that increasing the number of MSMPR cascade unit to rise the maximum mean crystalline size leads to lower performances.

One of the clear advantages using MSMPR instead of batch technologies is the possibility to achieve process steady state condition. This makes the morphology modelling easier as demonstrated by Borchert *et al.* (2009) which were able to predict the shape evolution trajectory of a crystal. Also, the steady state condition simplifies a lot the governing equations making the equipment design much easier.

1.2.1.2 Tubular crystallizer

Continuous tubular crystallizer can be classified as a plug flow unit. The crystals produced are collected at the end of the tube. Due to his narrower RTD it would be easier to control the product size distribution, but the difficult control of supersaturation and temperature make it harder. This indirectly leads to unwanted sedimentation which is the first cause of fouling.

Two main solutions are adopted to increase the continuous crystallization productivity in plug flow units without taking the risk of unstable and hardly controlled process. Dombrowski *et al.* (2007) shown how segmented tubular crystallizer (Fig 1.2), where the flow is divided in many individual droplets, can control the crystals size by controlling the maximum droplet size. Zhao *et al.* (2014) reached a productivity of 350 g/h with a purity of 99% using an oscillatory baffled continuous crystallizer. A scheme of the unit is shown in Fig. 1.3. The diameter of this unit can be larger than the segmented one leading to higher productivities. However, the amplitude of oscillation of the tubular could affect the product properties, and the internal baffles could improve the fouling if the oscillatory frequency is lower enough.

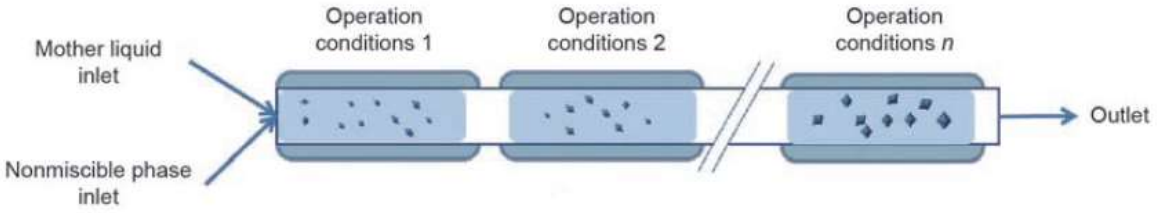

Figure 1.2: Segment flow crystallizer. Zhang *et al*., 2017.

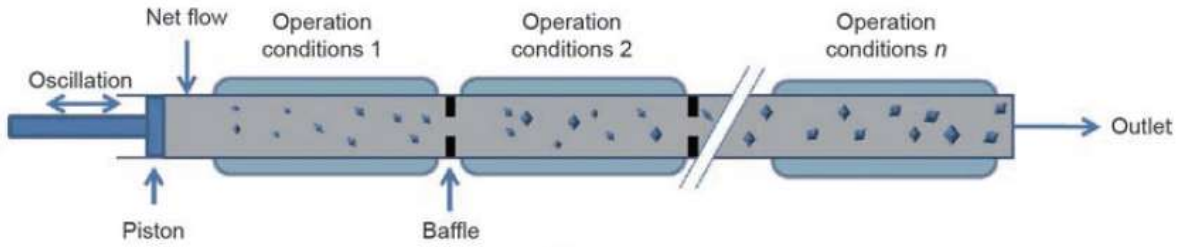

Figure 1.3: Oscillatory baffled crystallizer. Zhang *et al*., 2017.

1.2.2 Continuous granulation

In the last 20 years a lot of efforts were focused to transform the granulation step from a batch to continuous. This was necessary to allow the transition from a classic tableting process to a continuous manufacturing. Granulation was the critical step to properly answer to higher drug recalls (larger batch reactors). Also, the batch granulation flexibility was not high enough to allow process productivity changes from lower to full.

Continuous horizontal fluid bed agglomerators proposed by Bonde (1998) was the starting point to realize a multi-stage continuous system combining the drying stage with one or two fluidized beds. According to Masters (2002) a proper fixing of process parameters such as temperature, moisture residual content or spray characteristics could modify final particle size and properties to meet quality requirement or downstream operation specifications.

Extrusion was the most studied technique for continuous granulation step. Due to the yield to wet particles, continuous granulation by extrusion always must be coupled with a continuous drier such as fluidized bed or microwave. Usually, extrusion units present one or more rotating screws to transport and agglomerate the wetted granules.

Schroeder (2004) presented a planetary roller where a central main screw is surrounded by several intermeshing screws. The most useful feature of this technology was the possibility to introduce pressurized nitrogen into the ambient pressure unit. This step allows the induction of the foaming that enhance the yield to porous agglomerates and consequently modify the final tablet properties.

Padmanabhan (2017) proposed the "*true continuous, single pot manufacturing*" where a self-cleaning twin screw unit is able to minimize the RTD variance and avoid the hot-spots zones. This technology requires about 15 seconds to yield granules ready to be transformed into tablets. The absence of multi steps (granulation, drying and sizing) reduces the human error likelihood.

1.2.3 Continuous lyophilization

The increasing introduction of new biologic drug production technologies is consequently rising the demand of fast and efficient lyophilization technique.

Although batch lyophilization is a common and well-known process, due to its inefficiencies it can no longer satisfy the standards requirement of new drugs. Bad control of product quality of individual vial, limited productivity and long operational time were the driving force to move from batch to continuous lyophilization for the pharmaceutical industry.

The lyophilization process can be divided into two main steps. First, the freezing step in which there is the crystals nucleation. Then, the drying step where the heat provided to the sample and the degree of vacuum set in the drying chamber are able to remove of the excess water.

The stochastic nature of nucleation during the freezing step in batch lyophilization is the major responsible of non-homogeneity product quality across the same stock of vials or different batch volumes. During the drying, the variance of chamber pressure enhances the heterogeneity given by shelf to vial heat transfer. As a result, a lot of final products are rejected due to loss of active ingredient activity or too higher residual moisture content.

Downstream operations such as lyophilization have a major impact on the entire process productivity. Batch lyophilization could require up to some weeks to dry a single stock of vials. In addition, auxiliary operations like in-place sterilization and equipment testing increase the process time. All these constitute an important bottleneck on the process throughput.

The main advantages to adopt continuous lyophilization can be resumed in precise control temperature during nucleation, identical freeze-drying conditions and primary drying time reduction (Pisano, 2020).

Pharmaceutical industry still relies on batch lyophilization due to strict constrains that food industry does not have. Moreover, the conservative behaviour of the regulatory and the expensive transition from batch to continuous lyophilization which only large and consolidated companies can afford are delaying the transition. Lastly, new procedures and new skills requirement would need too.

Tax cuts, funding support to R&D programs and promotion of collaborations between manufacturing sectors are all incentives that must be considered to speed up the transition to continuous lyophilization (Pisano, 2020).

However, a lot of important pharmaceutical companies are showing interest in continuous lyophilization, and many technologies were proposed to satisfy the increasing demand. It is possible to distinguish between bulk freeze-drying continuous technology and unit doses ones (Pisano *et al.*, 2019).

In the continuous freeze-drying of bulk material, the final dosage of the drug is carried out at the end of the drying and the material transport across the different sections of the drying could easily be done (i.e., fluidized bed, vibrating or rotating system). In the continuous freeze-drying that work on unit doses, the dosage of solution into the drug container has to be done before the drying. In this last type of technology, it is easier to control the sterility during the entire drying phase, but the equipment design must consider the huge variety of dimensions and shapes that drug containers could have.

1.2.3.1 Continuous freeze-drying of bulk material

The technology proposed for continuous lyophilization finds its roots in food industry applications. First bulk continuous lyophilizer was proposed by Fuentevilla (1966) to dry food and pharmaceuticals. The system can only work with already frozen powders. First, the granular

material is loaded in a refrigerated chamber where the pressure is set equal to the vacuum chamber pressure. Then, the feeding hopper below the refrigerated chamber provide a fixed load on vibrating trays through multiple channels. Trays could be heated with electrical energy, circulating hot water or radiation. After the first drying, a microwave generator removes the excess residual moisture. A vapor sensitive control system regulate vibration and heating to achieve the best product quality.

According to Vigano (1966) a better solution to provide higher productivity was to feed the lyophilizer with liquid solutions instead of already frozen materials. He proposed a system where a controlled amount of the solution, after a preliminary degasification, is spread through a valve to the inner surface of a continuously evacuated cylinder. The liquid film formed is frozen thanks to the fast evaporation provided by the induced vacuum. Then, the collected frozen material can afford the primary drying phase. A scraped system with a vacuum cyclone is necessary to recover frozen material sticked to cylinder's walls.

Oetjen *et al.* (1971) proposed a system to avoid the thawing of products which occurs when comminuting is done outside the vacuum chamber. Already frozen materials are fed to a hopper linked with the drying chamber. The device loads the materials to vibrating screen conveyors that have openings equals to the desired size of particles to carry out the drying. If the particles have higher dimension than openings, they are forced into a comminution device located inside the vacuum chamber and then they are recirculated. After a proper comminuting phase the particles fall to vibrating heated beds that lead the dried products to a discharge hopper.

First approach to control product dimension and morphology of the dried product was proposed by Arsem (1986). A pressurized slurry is fed into a refrigerated tank with a perforated plate on the bottom. The diameter of the plate's holes is similar to the dimension of the ice crystals to form an aerosol of sublimated materials. The plates are refrigerated to freeze the inlet amount of slurry. At the outlet of the plate there is a heated screen, and the holes open to a vacuum chamber where drying is carried out.

The major problem with Arsem's system was the mechanically controlled morphology that forced downstream operations to ensure the product quality (i.e., granulation). Bruttini (1993) proposed a system to continuously control powder size and avoid human interventions. The solution to be dried is nebulized on the surface of a refrigerated revolving cylinder. Frozen materials are scrapped and fall on revolving planes. Each plane has gauged holes and is properly heated. When the frozen materials reach a proper dimension fall onto the under plane to continue the drying phase. At the bottom of the last plane is located a removable vessel.

Weisselberg (2013) registered a patent describing an ambient pressure lyophilizer that, according to the author, could be suitable for pharmaceutical purpose too. The apparatus is loaded with already frozen materials, and it is constituted by revolving plates with several holes. Meanwhile the frozen materials fall onto the under plate through the holes, it is dried by recirculated heated air or gas. To maintain into the air/gas the partial pressure of substance that has to be dried as low as possible, a series of filter, cooling system and desiccant system is provided to the apparatus. A set of funs force the air/gas into the recirculating path.

Following the idea of the above technologies, Rey (2010) proposed one of the most famous lyophilizer proposal for pharmaceutical purpose. Regular droplets of the solution are frozen and loaded, through a vacuum lock, to a vibrating heated conveyor. At the end of the first conveyor, it is located a second vacuum lock that discharge the material to a second vibrating conveyor for the secondary drying. In this section microwave or infrared can help the removing of the residual moisture. Finally, the granules are discharged into pre-sterilized vials which then are continuously capped. A scheme is presented in Fig. 1.3. Although this system seems promising, due to the direct contact between granules and mechanical parts of the lyophilizer a lot of

sterility problems come out. Moreover, even if small granules dimension ensures low drying time some particles could be cluster together or could be affected by mechanical erosion.

According to Hosokawa Micron BV company in Doetinchem (Van der Wel, 2015) the issues presented by Rey's lyophilizer could be solved operating the lyophilization under mixed conditions. The solution proposed was a two stirred tanks unit, the first one loaded with the active solution and a freeze medium to carry out the freezing step. In the second stirred tank is provided a proper pressure to realize the sublimation and a jacket guaranteed an adequate heating level. Fig. 1.4 shows a scheme of the unit. Mixing provides a better heat exchange to reduce drying time and a separation of possible clusters to avoid downstream crush operations. Overall, a better efficiency and a reduced risk of contamination is achieved. However, sublimated materials discharged from the unit often carry some dried dust contamination and a filter has to be designed.

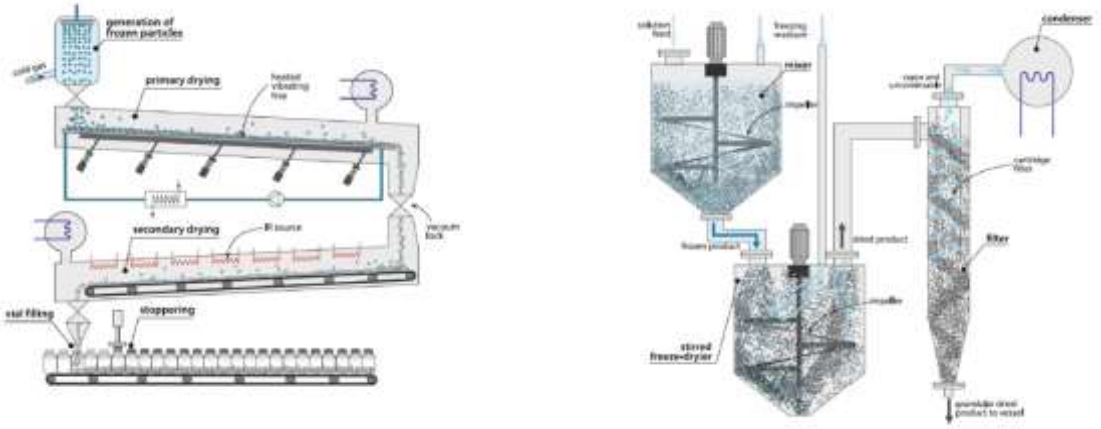

Figure 1.4: (left) Continuous freeze-dryer proposed by Rey, (right) Continuous freeze-dryer proposed by Hosokawa Micron BV company. From Pisano (2019), modified picture.

Recently, Telstar (Bullich, 2015) announced to start a codeveloping of a spray-freeze-drying device with Ulvac. The main idea of this technology is to spray the active solution and carry out a self-freezing to obtain microparticles with uniform size distribution. The high surface-to-volume ratio provides a much faster lyophilization than bulk lyophilization. Moreover, the particles can directly be deposited onto the surface of the heated tray, providing a closed system with sterilized conditions.

1.2.3.2 Unit dosage in the continuous freeze-drying

Most of the existing discontinuous pharmaceutical freeze-dryers work on unit-dosage to guaranteed sterility and a better dosage control. Although, as previously said, the design of a continuous apparatus of this type is very difficult, some approaches were presented.

One of the most successful technology proposed for unit-dosage lyophilization was Corver (2012) freeze-dryer. The unit starts with a spin-freezing section where filled vials are rotated along their longitudinal axis. The freezing is provided by a fixed temperature inert gas. Then, a load-lock system discharges the vials into the drying sections formed by two drying chambers at different pressure for primary and secondary drying. An endless belt transports the vials through the two chambers while heating is supplied by conduction and radiation. In Fig. 1.4 scheme of the apparatus is presented. The spin technology proposed spreads the solution over the vial surface which is larger than the one provided by classical freeze-drying. According to De Meyer *et al.* (2015) the process time could be reduced by a factor up to 40.

Trout (2018) in collaboration with MolE research group at Politecnico di Torino realized a continuous unit-doses freeze-dryer. They presented an apparatus where vials are continuously filled with a controlled amount of active solution and moved by a track system through sections at different temperature and pressure conditions (Fig. 1.5). According to authors, freezing of the vials can be achieved with both spontaneous nucleation and controlled nucleation with (VISF) vacuum induced surface freezing (Oddone *et al.*, 2014 and Oddone *et al.*, 2016). The controlled nucleation achieved with VISF reduces vial-to-vial ice morphology heterogeneity and enhance the final structure of the products. The drying is provided by low pressure and heat radiation hence very low vacuum level can be used without influencing the heat transfer. According to authors, the suspended configuration of these technology provides the same heat and mass transfer conditions for all the vials, drastically reducing the inhomogeneity in the final stock. Furthermore, the concept behind this process can potentially be suitable with new particle-based lyophilization such as spray freeze drying technique. Comparing the freeze-drying of 5% sucrose solution in both batch and suspended configuration, the authors achieved a 10 times reduction factor in lyophilization time with last configuration.

To achieve a continuous lyophilization it is needed a proper technology where mass and heat transfer are enhanced without compromising the structure and sterility of the final product. Moreover, homogeneity in both morphology and size of the drugs must be controlled.

The spray freeze-drying technology could solve the major problems that the proposed technologies are currently facing and give a proper answer to all the requirement of the future continuous pharmaceutical industry.

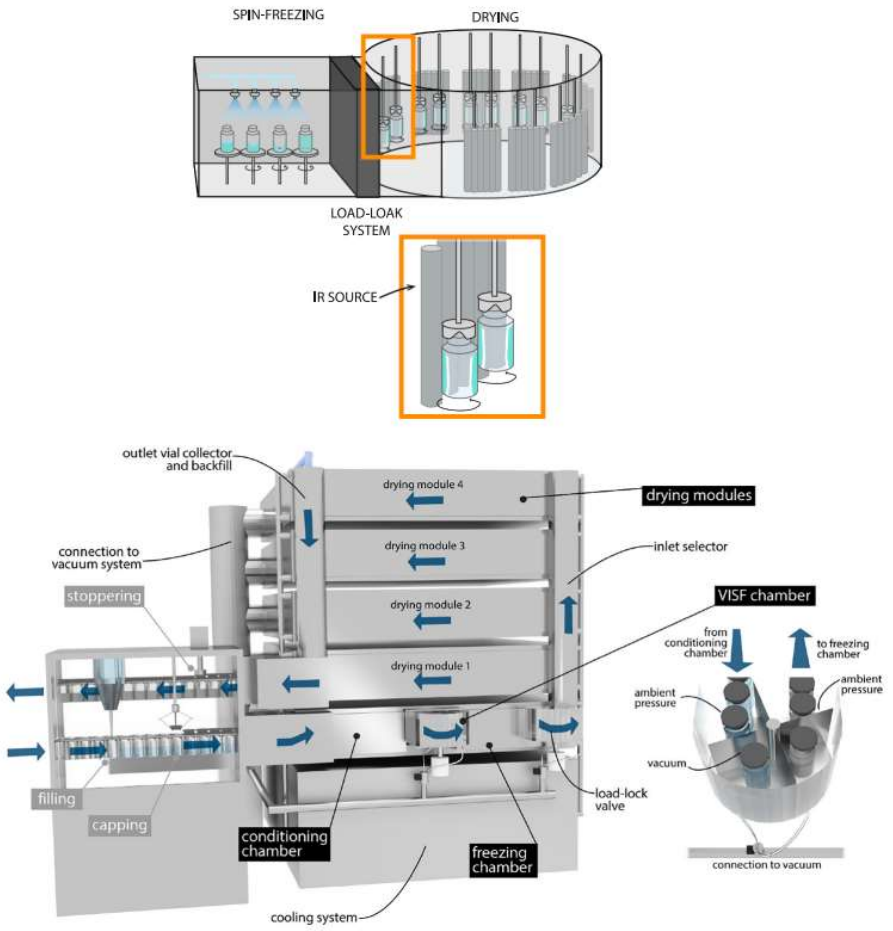

Figure 1.5: (Top) Continuous freeze-dryer proposed by Corver, (Bottom) Continuous freeze-dryer proposed by Trout *et al*. From Pisano (2019), modified picture.

1.2.3.3 Spray-Freeze-Drying

Spray-freeze-drying (SFD) it is a method ideal to freeze-dry proteins, vaccines, aerosol and nanoparticles where is essential to control size and porous shape. Thanks to a fast-freezing phase, denaturation of the active principle can be prevented. Different technologies can be selected and used to carry out the different steps of the method and obtain various formulations and high flexibility. Moreover, the spherical powders obtained with SFD provide very high mass and heat transfer rates, improved rehydration rates and encapsulation reliability.

According to Vishali (2019), the SFD technique could have a central role in the development of controlled and targeted delivery system of drugs. SFD provides a fast freeze reducing the risk of phase separations between active principles and excipients. Hence, temperature and pH sensitive active principles can be coupled with carriers providing improved human metabolism resistance and a better therapeutic effect.

Parthasarathi and Anandharamakrishnan (2016) used the vitamin E to confront SFD technique with classical freeze drying (FD) and spray drying (SD) method. They demonstrated higher oral availability of vitamin E in rats than SD and FD. D'Addio *et al.* (2013) studied mannitol carriers to compare SFD and SD lung delivery. They found that SFD gave enhanced delivery properties with lesser cluster formation. Schiffter *et al*. (2010) used ultrasonic SFD to show an improved penetration depth of insulin particles under the skin.

SFD principles

The spray-freeze-drying technique is a three steps method (Fig. 1.6). Initially, the active solution is sprayed through an atomizer into a cooling medium. Then, the direct contact between droplets and cooling medium provides to lock the atomized solution into spherical frozen particles. Finally, frozen particles can be transferred to the drying section to sublimate the solvent.

Size and morphology of the dried powders are mainly linked to the methods used to carry out the first two stages. Instead, the technique adopted to dry the particles affects the mass and heat transfer hence the drying time (Adali, 2020).

The peculiar characteristics of SFD products allow process flexibility through easier manipulation of parameters such as shelf temperature, composition of the active solution, atomizer selection, etc. Hence, the desired moisture content, particle shape and high morphology control can be achieved.

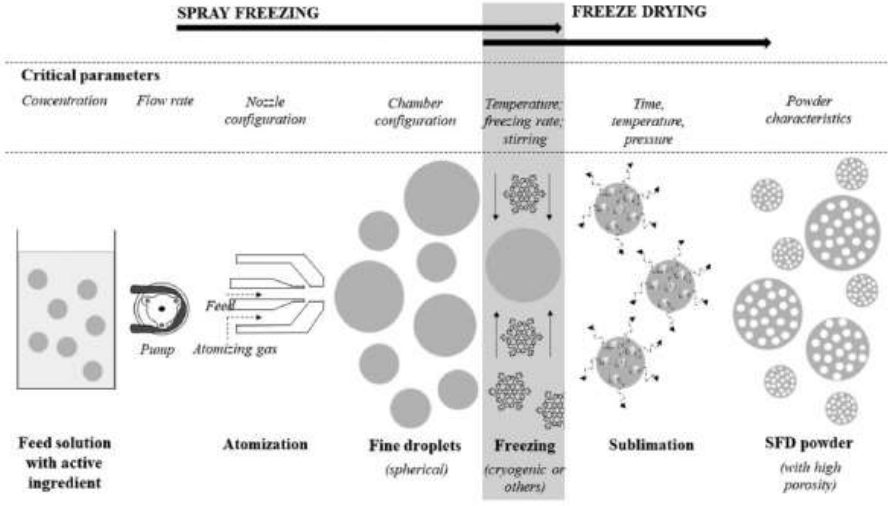

Figure 1.6: Spray freeze-drying process. Vishali *et al.*, 2019

Spray-Freezing

Particle size distribution is strongly determined by the spraying step. This is particularly important in drug delivery as shown by Engstrom *et al*. (2007). The authors demonstrated that 1-5 μm particle diameter is needed in pulmonary delivery through inhalation.

The choice of the atomizer and atomization parameters is critical to achieve the best drug quality. For example, according to Costantino *et al*. (2000) the flow ratio between feeding solution and atomizing gas influenced the particle final size.

There are different type of atomizer providing peculiar droplets characteristics. The most used nozzles are briefly presented below.

In the hydraulic nozzle the solution is forced through the orifice converting the liquid pressure into kinetic energy. It can produce a wide range of particle size. Usually, particles have high density and good aerodynamic properties. However, the particle size distribution has large variance, and the nozzles is usually affected by corrosion (Adali, 2020).

In the pneumatic nozzle the interaction between the feeding solution and a compressed gas gives the energy to atomize. When there are only one feeding solution and one compressed gas the configuration is the so called two-fluid nozzle. However, it is possible to work with one more feeding solution and one gas channel (three-fluid nozzle), and with one more gas channel (four-fluid nozzle). This type of nozzle has a narrower particle size distribution than hydraulic nozzles and can manage higher viscous solutions. However, it presents ingent operational costs due to high consumption of compressed gas, and the drying time of the frozen particles is influenced by the temperature gradients provided by the interaction between solution and gas stream (Adali, 2020).

In ultrasonic nozzles the energy is provided by high-frequency electrical signal that is converted into mechanical energy. The droplet size distribution depends on the electrical signal frequency. This type of nozzle it is able to obtain uniform particle size but can work only with low viscous Newtonian fluids (Adali, 2020).

Once the feeding solution is atomized, a cryogenic medium provides the droplets' freezing. Most used cryogenic medium is vapour or liquid nitrogen thanks to its inertness and desirable low bowling point. Fast freezing is allowed by high surface to volume ratio provided by atomization and low cryogenic medium temperature. Thanks to that, crystallization of excipients, phase separation and pH shift can be avoided hence structural damage of the active principle does not occur.

Freezing step could be carried out with different methods. The most consolidated are spray freezing into vapour (SFV), spray freezing into liquid (SFL) and spray freezing into vapour over liquid (SFV/L).

In the SFV configuration the atomized feeding solution is sprayed into a chamber containing the cold medium gas. Due to the counter-current configuration particles erosion, particles collection efficiency and elutriation are major problems. To avoid these issues, Wang *et al*. (2006) developed a system were cold nitrogen flows into the chamber from lateral holes and particles are collected to an external filter disc.

SFL technology was patented by Williams *et al*. (2005) and is commercialized by Dow Chemical Company. In this configuration the atomizer nozzle is located directly into a liquid cryogenic medium. Usually, to increase freezing rate and avoid particles clustering the liquid medium is stirred. The nozzle must have a very low thermal conductivity to avoid clagging. Thanks to this method very high freezing rates are obtained. According to Rogers *et al*. (2003) due to high surface area obtained by fast freezing, SFL danazol particles shown the best

dissolution behaviour. Instead, Yu *et al*. (2002) evidenced that high freezing rate hence increased water ice interface area enhance proteins denaturation.

According to Adali (2020) the most used spray freezing technique for pharmaceutical purposes is SFV/L. In this system, the nozzle is located at a fixed distance from a boiling cryogenic medium which could be stirred. Sprayed droplets start the freezing by falling through the cold vapour and achieve completed frozen state when reach the liquid surface. Then, frozen particles can be collected by sieving or inducing the evaporation of the cryogenic liquid. Otake *et al*. (2016) studied the particle size distribution of six different SFV/L ammino acids. They stated particle diameter always ranged between 5 μm up to 10 μm.

Freeze-Drying of frozen granules

Once frozen particles are collected, and the residual cryogenic medium is eventually removed the freeze-drying step can be performed. Usually, particles are transferred on pre-chilled trays or into pre-conditioned vials.

Vacuum freeze-drying is the most used in pharmaceutical applications. During this phase, very low pressure is used to perform primary and secondary drying to respectively remove water from formulation and boundary water. The vacuum step can be performed in fluidized bed, fixed chamber, or rotatory units.

Thanks to SFD flexibility, a lot of different solutions can be adopted to increase the overall drying phase efficiency. For example, Zhang *et al*. (2020) investigated how inert particles can be used as thermal conductors and particle bed void reducers. The feeding solution was directly sprayed and frozen on the surface of cold inert particles. The authors shown how the void reduction allowed higher vacuum level hence a shorted drying time required. The optimum was found to be using 5 mm inert particles.

Tunnel vacuum freeze-drying is currently on of the best solution to reduce drying time and product loss. The heat provided by infrared or microwave allow higher vacuum level. Although this technology is commonly used in food industry, the application in pharmaceutical manufactory is still challenging.

Some critical aspects of vacuum drying are the high operational costs and the presence of vacuum interlocks that does not well match with a continuous process. Meryman (1956) was the first to illustrate the possibility to work with atmospheric freeze-drying using a cold and dry air stream. From thermodynamically point of view atmospheric freeze-drying is possible until the water partial pressure is kept below the ice vapour tension. However, Claussen *et al*. (2007) shown how the controlling parameter was the molecular diffusion through porous structure in atmospheric freeze-drying. Hence, the high mass transfer resistance can negatively influence the drying time.

A promising solution could be the so called sub-atmospheric freeze-drying. Thanks to low vacuum conditions, the large amount of dry stream can be reduced without lowering the molecular diffusion. Anandharamakrishnan *et al*. (2010) proposed a pilot-scale spray freeze-dryer constituted by a sub-atmospheric fluidized bed. The authors found a ten-reduction factor in drying time when the same reduction is applied to atmospheric pressure. Moreover, according to authors low gas viscosity avoid particle elutriation and drag particle corrosion.

Although the development of a continuous spray-freeze-dry process is still a challenge for pharmaceutical manufacturing some of the existing batch technology can be converted with minimal modifications. Reducing capital and operational costs achieving higher process throughput are pushing towards a fully continuous spray freeze-dryer.

1.3 *Motivation of the thesis*

The aim of this work is to develop an innovative model able to predict the behaviour during primary drying of frozen particles packed-bed loaded into vials.

A mathematical model is needed to proper design process units and evaluate the impact of SFD process parameters to the drying phase. Thanks to software simulations of the model, it is possible to observe temperature and concentration profiles along vials and avoid active ingredient denaturation. Furthermore, it is possible to study when mass or heat transfer become the controlling mechanism. Overall, accurate predictions make it possible to study the impact of operational and equipment type choices on the SFD results. This would hopefully facilitate the transition from batch to continuous manufacturing.

At first, edits on the already existing models were made to achieve a more realistic description of bed behaviour during drying hence a first mathematical model was obtained. Then, a particle model was developed to estimate some key parameters necessary to solve the first model. Finally, a comparison between experimental data and first model predictions were made.

In the first part of this work a briefly review of why continuous pharmaceutical manufacturing should be achieved was presented, the current technologies that are trying to do that and why spray-freeze-drying it is a promising technique to reach a continuous process.

In chapter 2 the existing models will be presented to describe the primary drying step and the issues linked to them. Then, the particle and the developed mathematical models will be described in detail. After that, a brief software description will be given with the configurations used and a list of all the simulations. At the end it will be explained how the experimental validation of the first mathematical model was realized.

In chapter 3 simulation results will be shown. In particular, it will be possible to observe how the frozen particles characteristics influence mass and heat transfer across the granules. Furthermore, an equilibrium between sublimation and condensation during the drying phase and how the controlling transport mechanism is influenced by the granules physical properties will be presented.

Chapter 4 summarizes the results obtained and highlights what are the most critical parameters to obtain the desired conditions during primary drying. Moreover, a conclusion of how these parameters can impact on continuous pharmaceutical manufactory will be presented at the end of the work.

2 Models and methods

2.1 *Mathematical modelling of the drying step of frozen particles packed bed drying*

To facilitate the comprehension of the following derivation, a nomenclature list of the major symbols present in the model is reported at the end of the section in Fig. 2.2.

Frozen particles obtained from spray-freezing generates a packed-bed usually loaded in trays or in vials on temperature-controlled shelves. During drying, the transport of solvent vapour across the bed is provided by channels formed by the packed particles. In order to satisfy local thermodynamic equilibrium in these channels, the frozen solvent can sublimate, or the solvent vapour can condense. Thus, the voids between packed particles are partially filled with frozen solution and gas mixture. Overall, the saturation level can both increase and decrease.

The drying mechanism of packed-bed of frozen granules is significant different from classical bulk drying that involves a non-porous saturated frozen solution.

In addition, each dried product particles have a porous structure which depends on the initial frozen solvent crystals (Fig. 2.1). This porous structure is completely different from the porous structure of the packed-bed, hence a bidisperse system has to be adopted to describe the dried zones of the packed-bed.

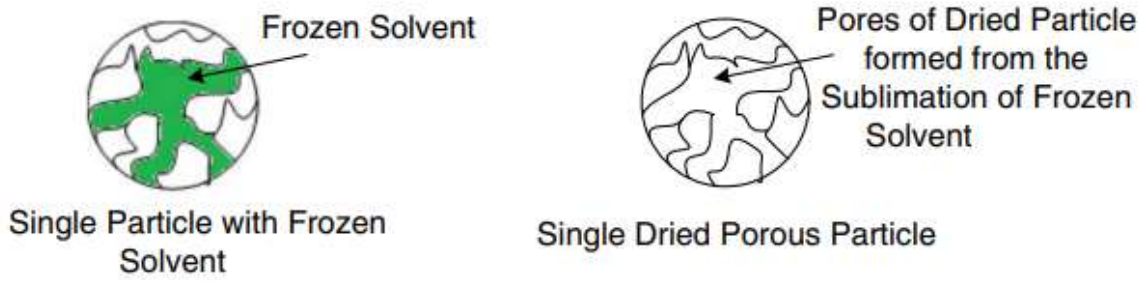

Figure 2.1: (left) Frozen and (right) Dried particle. Liapis and Bruttini, 2007.

It is clear that, in order to control the operational conditions in the drying chamber, hence achieve increased productivity and lower operational costs, knowledge about the heat and mass transfer mechanisms involved is required. A dynamic mathematical model describing both these mechanisms by Liapis and Bruttini (2009) is presented below.

2.1.1 Liapis and Bruttini model: Primary and secondary drying

Liapis and Bruttini presented a model for both packed-bed in trays and packed-bed in vials on trays. They divided the bed into two domains: an unsaturated porous frozen region (Layer II) and a dried bidisperse region (Layer I). As shown in Fig. 2.3, the two domains are sharply separated by a moving sublimation front. The variables X and Z=H(r,t) represent the position of the moving interface for materials dried in trays and materials dried in vials, respectively. When the front reaches the bottom of the tray/vial the primary drying is considered completed. The variables q_I, q_{II} and q_{III} are the heat fluxes supplied to the material. All the equations are reported taking water as solvent.

The model core parameter is the so called ice saturation *S*, defined as the fraction of the frozen volume to the void volume of the particle.

$$S = \frac{\frac{4}{3}\varepsilon_p \pi d_{ice}^3}{\frac{4}{3}\varepsilon_p \pi d_p^3} = \left(\frac{d_{ice}}{d_p}\right)^3 \tag{2.1.1}$$

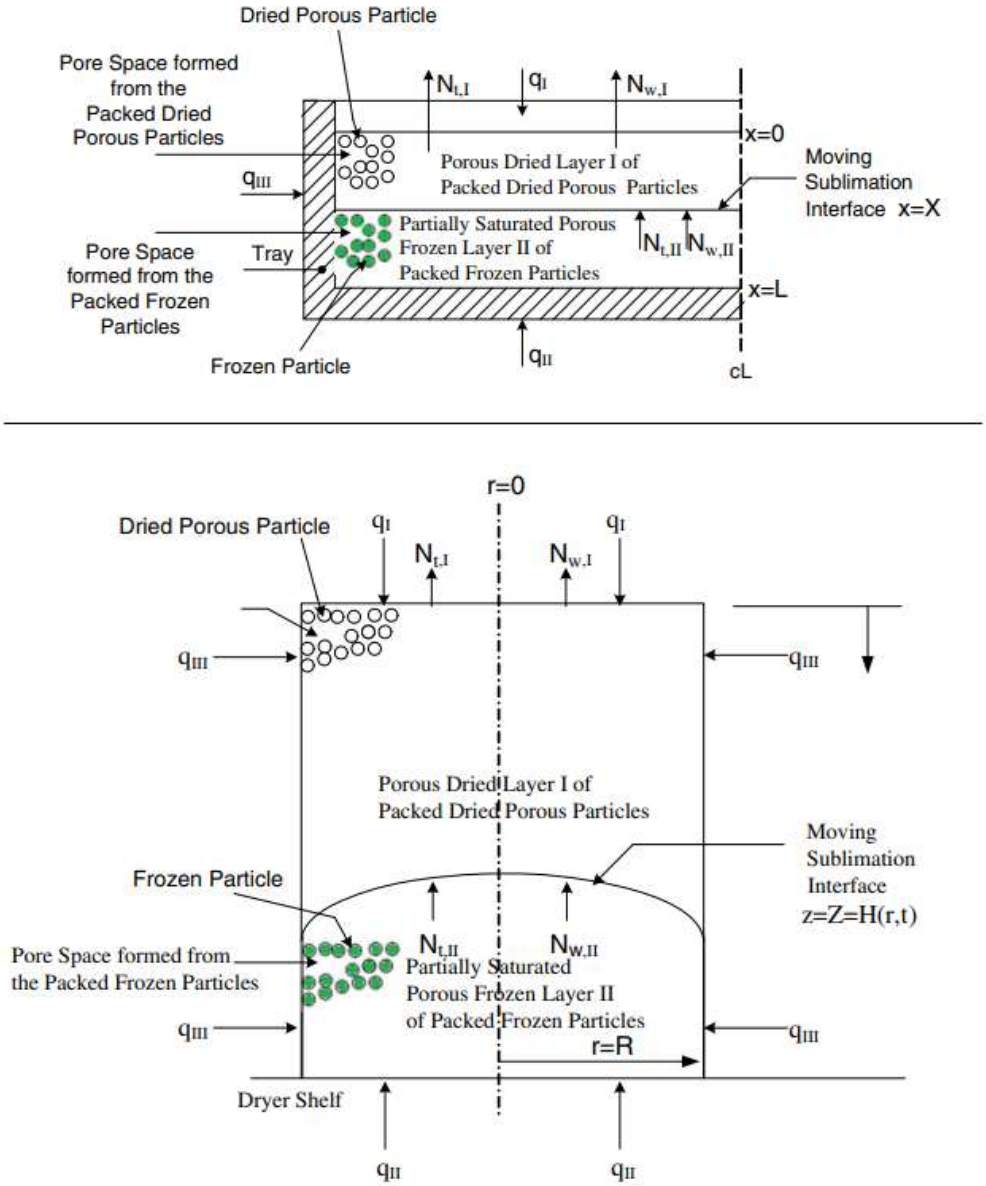

Figure 2.3: (top) Drying step in trays, (bottom) Drying step in vials on trays. Reprinted from Liapis and Bruttini (2009) with modifications.

The parameter d_{ice} represents the diameter of a frozen core which decreases while the drying goes on. Thanks to the value of *S*, it is possible to understand for each particle in which kind of situation they are (Fig. 2.4). When *S* it is equal to 1, the pore volume into the particle it is completely frozen. Instead, when *S* it is lower than 1 the particle is partially dried. Finally, when *S* it is greater than 1 a frozen layer is formed on the surface of the particle and the void space between particles is lower. Furthermore, the value of the time derivative of *S* can describe what phenomenon is currently occurring in the particle. If the solvent vapour tension is greater than the vapour pressure, the solvent will sublimate, and the derivative will be lower than 1. Instead,

condensation will occur when the solvent vapour tension is lower than the vapour pressure, hence the derivative is greater than 1.

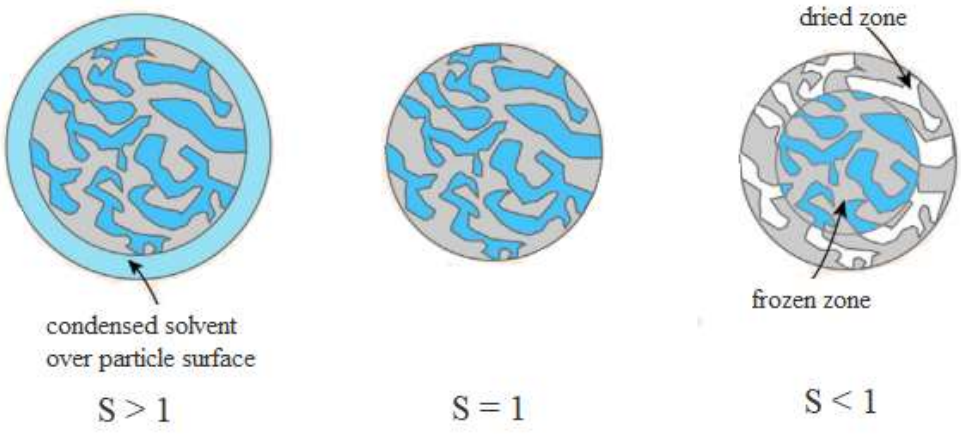

Figure 2.4: Schematic illustration of ice saturation behaviour. From Capozzi *et al*. (2019a), modified picture.

The volume-averaged ice saturation is given by Eq. (2.1.2). The volume averaged is just the porous frozen domain because dried layer has always a null ice saturation value.

$$S_{av} = \frac{1}{V_{II,p}} \int_0^{V_{II,p}} S \, dV_{II,p} \tag{2.1.2}$$

Thanks to the use of Eq. (2.1.2) the authors defined some physical properties of the packed-bed that will be used to describe the transport mechanisms.

$$\rho_f = (1 - \varepsilon_{pb})\rho_{f,s} \tag{2.1.3}$$

$$\rho_d = (1 - \varepsilon_{pb})\rho_{d,s} \tag{2.1.4}$$

$$\rho_I = (1 - \varepsilon_{pb})\rho_{d,s,f} \tag{2.1.5}$$

$$\rho_{II} \cong S_{av}\rho_f + (1 - S_{av})\rho_d \tag{2.1.6}$$

$$\rho_{II} C_{p_{II}} \cong S_{av}\rho_f C_{p_f} + (1 - S_{av})\rho_d C_{p_d} \tag{2.1.7}$$

$$k_{II} = S_{av}k_f + (1 - S_{av})k_d \tag{2.1.8}$$

According to authors, Layer I does not present condensed solvent (i.e., *S*=0). Thus, during primary drying, the energy balance equation for the dried region is as follows:

$$\rho_{I_e} C_{p_{Ie}} \frac{\partial T_I}{\partial t} = \boldsymbol{\nabla} \cdot \left(k_{I_e} \boldsymbol{\nabla T_I}\right) - C_{p_g} \left(\boldsymbol{\nabla} \cdot \left(\boldsymbol{N_{t,I}} T_I\right)\right) + \Delta H_v \rho_I \left(\frac{\partial C_{sw}}{\partial t}\right) \tag{2.1.9}$$

The last term accounts for the amount of bounded water that could desorb during primary drying (usually neglected). The expressions to estimate the effective parameters (i.e., ρ_{Ie}, C_{pIe} and k_{Ie}) is reported in Table 1 of Liapis and Bruttini (2009) work.

The term $N_{t,I}$ in Eq. (2.1.9) represents the total mass flux vector in Layer I and is given by the sum of the mass flux vectors of water vapor and inert (Eq. 2.1.10). Both mass flux expressions (Eqs. 2.1.11 and 2.1.12) derive from the dusty-gas model (Manson and Malinauskas, 1983).

$$\boldsymbol{N_{t,I} = N_{w,I} + N_{in,I}} \tag{2.1.10}$$

$$\boldsymbol{N_{w,I}} = -\frac{M_w}{R_g T_I}\left(k_{1,I}\boldsymbol{\nabla p_{w,I}} + k_{2,I} p_{w,I}\boldsymbol{\nabla P_I}\right) \tag{2.1.11}$$

$$\boldsymbol{N_{in,I}} = -\frac{M_{in}}{R_g T_I}\left(k_{3,I}\boldsymbol{\nabla p_{in,I}} + k_{4,I} p_{in,I}\boldsymbol{\nabla P_I}\right) \tag{2.1.12}$$

The expressions to calculate $k_{1,I}$, $k_{2,I}$, $k_{3,I}$ and $k_{4,I}$ are reported in Fig. 2.2. These parameters account to the various mass transport mechanisms that are present during the drying (i.e., Darcy's flow, Knudsen diffusion, and bulk binary diffusion).

The continuity equations for water vapour and inert gas allow to calculate the corresponding partial pressures in Layer I (Eqs. 2.1.14 and 2.1.15). The sum of the partial pressures corresponds to the term P_I (Eq. 2.1.13).

$$P_I = p_{w,I} + p_{in,I} \tag{2.1.13}$$

$$\frac{\varepsilon_{t,I} M_w}{R_g T_I}\left(\frac{\partial p_{w,I}}{\partial t}\right) = -\boldsymbol{\nabla \cdot N_{w,I}} - \rho_I \frac{\partial C_{sw}}{\partial t} \tag{2.1.14}$$

$$\frac{\varepsilon_{t,I} M_{in}}{R_g T_I}\left(\frac{\partial p_{in,I}}{\partial t}\right) = -\boldsymbol{\nabla \cdot N_{in,I}} \tag{2.1.15}$$

The term $\varepsilon_{t,I}$ in Eqs. (2.1.14) and (2.1.15) represents total porosity of the dried layer. Eq. (2.1.16) accounts to the bidisperse nature of Layer I.

$$\varepsilon_{t,I} = \varepsilon_{pb} + \left(1 - \varepsilon_{pb}\right)\varepsilon_p \tag{2.1.16}$$

Mass and heat transport in Layer II is similar to Layer I, but the equations account the possibility that S can be different from 0. The energy balance equation (Eq. 2.1.17) has to consider the unsaturation state in Layer II, hence the time derivative of S should be present.

$$\rho_{II} C_{p_{II}} \frac{\partial T_{II}}{\partial t} = \boldsymbol{\nabla \cdot}\left(k_{II}\boldsymbol{\nabla T_{II}}\right) - C_{p_g}\left(\boldsymbol{\nabla \cdot}\left(\boldsymbol{N_{t,II}} T_{II}\right)\right)$$
$$+\Delta H_s\left(\rho_f - \rho_d\right)\frac{\partial S}{\partial t} + \Delta H_v \rho_I \left(\frac{\partial C_{sw}}{\partial t}\right) \tag{2.1.17}$$

The term $N_{t,II}$ in Eq. (2.1.17), as in Layer I, represents the total mass flux vector in Layer II and is given by the sum of the mass flux vectors of water vapor and inert (Eq. 2.1.18). Once again, both mass flux expressions (Eqs. 2.1.19 and 2.1.20) derive from dusty-gas model.

$$\boldsymbol{N_{t,II} = N_{w,II} + N_{in,II}} \tag{2.1.18}$$

$$\boldsymbol{N_{w,II}} = -\frac{M_w}{R_g T_{II}}\left(k_{1,II}\boldsymbol{\nabla p_{w,II}} + k_{2,II} p_{w,II}\boldsymbol{\nabla P_{II}}\right) \tag{2.1.19}$$

$$\boldsymbol{N_{in,II}} = -\frac{M_{in}}{R_g T_{II}}\left(k_{3,II}\boldsymbol{\nabla p_{in,II}} + k_{4,II} p_{in,II}\boldsymbol{\nabla P_{II}}\right) \tag{2.1.20}$$

The expressions to calculate $k_{1,II}$, $k_{2,II}$, $k_{3,II}$ and $k_{4,II}$ are reported in Fig. 2.2. The sum of water and inert partial pressures corresponds to the term P_{II} (Eq. 2.1.21).

According to authors, it should be noted that a non-constant value of S during time means variation in both water partial pressure and Layer II total porosity. Thus, the water continuity

equation has to provide the evolution of the ice saturation (Eq. 2.1.22). Instead, the inert continuity equation has the same form reported for Layer I (Eq. 2.1.23).

$$P_{II} = p_{w,II} + p_{in,II} \tag{2.1.21}$$

$$\frac{M_w}{R_g T_{II}}\left(\frac{\partial(\varepsilon_{t,II} p_{w,II})}{\partial t}\right) = -\boldsymbol{\nabla}\cdot\boldsymbol{N_{w,II}} - \left(\rho_f - \rho_d\right)\frac{\partial S}{\partial t} - \rho_I \frac{\partial C_{sw}}{\partial t} \tag{2.1.22}$$

$$\frac{M_{in}}{R_g T_{II}}\left(\frac{\partial(\varepsilon_{t,II} p_{in,II})}{\partial t}\right) = -\boldsymbol{\nabla}\cdot\boldsymbol{N_{in,II}} \tag{2.1.23}$$

In Layer II $p_{w,II}$ is equal to the ice vapour tension $p_w^{sat}(T_{II})$. To solve Eq. (2.1.22), $p_w^{sat}(T_{II})$ is provided by Marti and Mauersberger expression (Marti and Mauersberger, 1993).

The variation in time of the total porosity $\varepsilon_{t,II}$ is taken into account using Eq. (2.1.2) in the definition (Eq. 2.1.24).

$$\varepsilon_{t,II} = \varepsilon_{pb} + \left(1 - \varepsilon_{pb}\right)\varepsilon_p(1 - S_{av}) \tag{2.1.24}$$

The initial and boundary conditions to solve energy and continuity equations in both layers depend on the operative conditions used to carry out the drying phase. To solve Eqs. (2.1.22) and (2.1.23), the authors suggest to use the following conditions in the porous of Layer II to determine the inert partial pressure distribution.

$$t = 0, S = 1 \tag{2.1.25}$$

$$t = 0, p_{in,II} = p_{in,II}^0 \tag{2.1.26}$$

$$t \geq 0, \nabla p_{in,II} = 0 \tag{2.1.27}$$

According to the authors, Eq. (2.1.27) should be applied just at impermeable surfaces or at a centreline of symmetry.

Starting from initial and boundary conditions, the energy balance equations can be first solved. Then, partial pressures and continuity equations can be calculated to provide new values for the mass fluxes and ice saturation. Finally, the iterative count restarts by solving again the energy equations.

As anticipated before, the authors used a moving sublimation front to simulate the bed drying. A combination of energy (Eq. 2.1.28) and material (Eq. 2.1.29) balances across the moving interface, is needed to determine its velocity. The thickness of the sublimation front is taken to be infinitesimal.

$$\begin{aligned}\left(\rho_{II} C_{p_{II}} T_{II} - \rho_I C_{p_I} T_I\right)\boldsymbol{V}\cdot\boldsymbol{n_{interf}} \\ = -\Delta H_s N_{w,interf} - C_{p_g} T_{interf} N_{t,interf} \\ + \left(-k_{II}\boldsymbol{\nabla T_{II}}\right)\cdot\boldsymbol{n_{interf}} - \left(-k_{I_e}\boldsymbol{\nabla T_I}\right)\cdot\boldsymbol{n_{interf}}\end{aligned} \tag{2.1.28}$$

$$\boldsymbol{V} = -\frac{\boldsymbol{N_{w,interf}}}{\rho_{II} - \rho_I} \tag{2.1.29}$$

The term n_{interf} in both the above equations, represents the normal vector to the moving sublimation front. The balances are directly correlated to the derivative of ice saturation through the mass flux terms, hence the interface velocity depends on how fast the sublimation occurs in the packed-bed.

According to the authors, the model can be used to describe the secondary drying phase too. During this stage, there is no longer a Layer II and the value of S in the entire bed is null. Thus, Eqs. (2.1.9), (2.1.11) and (2.1.12) can be used.

The concentration profile of bound water is obtained by solving Eq. (2.1.30). Note that this equation is required if it is necessary to take into account bound water during primary drying too.

$$\frac{\partial C_{sw}}{\partial t} = -k_{des} C_{sw} \tag{2.1.30}$$

The value of k_{des} is reported in Table 1 of Liapis and Bruttini (2009) work.

Nomenclature

c_p	heat capacity (kJ/kg)
c_{sw}	concentration of bound (sorbed) water (kg water/kg solid)
C_{01}	constant dependent only upon the structure of the porous medium and giving relative Darcy flow permeability (m^2)
C_1	constant dependent only upon the structure of the porous medium and giving relative Knudsen flow permeability (m)
C_2	constant dependent only upon the structure of the porous medium and giving the ratio of bulk diffusivity within the porous medium to the free gas bulk diffusivity (dimensionless)
d_{ice}	diameter of ice core in particle (m)
d_p	diameter of particle (m)
d_{pore}	mean pore diameter of porous layer formed from the packing of the particles (m)
$D_{w,in}$	free gas mutual diffusivity in a binary mixture of water vapor and inert gas (m^2/s)
$D^0_{w,in}$	$D_{w,in}P$ (N/s)
$H(t,r)$	geometric shape of the moving interface, a function of time and radial distance (m)
k	thermal conductivity (W/K m)
k_1	bulk diffusivity constant, $k_1 = C_2 D^0_{w,in} K_w/(C_2 D^0_{w,in} + K_{mx}P)$ (m^2/s)
k_2, k_4	self-diffusivity constant, $k_2 = k_4 = (K_w K_{in}/(C_2 D^0_{w,in} + K_{mx}P)) + (C_{01}/\mu_{mx})$ (m^4/N s)
k_3	bulk diffusivity constant, $k_3 = C_2 D^0_{w,in} K_{in}/(C_2 D^0_{w,in} + K_{mx}P)$ (m^2/s)
k_{des}	rate constant in the desorption mechanism of bound water, (s^{-1})
K_w	Knudsen diffusivity for water vapor, $K_w = C_1(R_g T/M_w)^{0.5}$ (m^2/s)
K_{in}	Knudsen diffusivity of inert gas, $K_{in} = C_1(R_g T/M_{in})^{0.5}$ (m^2/s)
K_{mx}	mean Knudsen diffusivity for binary gas mixture, $K_{mx} = y_w K_{in} + y_{in} K_w$ (m^2/s)
L	length (height) of material in tray or vial (m)
m_w	amount of free water in material (kg/m^2)
M	molecular weight (kg/kmol)
N	mass flux (kg/m^2 s)
p	partial pressure (Pa)
p_w^{sat}	saturated water vapor pressure (Pa)
P	total pressure (Pa)
P_{dcham}	pressure in drying chamber (Pa)
q	heat flux (W/m^2)
r	space coordinate of radial distance (m)
R	radius of vial (m)
R_g	ideal gas constant (J/K mol)
S	ice saturation, (dimensionless)
S_{av}	volume-averaged ice saturation, (dimensionless)
t	time (s)
T	temperature (K)
T_X	temperature at surface of moving interface (K)
V	velocity of moving interface (m/s)
x	space coordinate of distance along the length (height) of the material in the tray (m)
X	position of moving interface in the material in the tray (m)
y	mole fraction (dimensionless)
z	space coordinate of distance along the length of the vial (m)
Z	value of z at the moving interface in the vial (m)

Greek letters

ΔH_s	heat of sublimation of ice (J/kg)
ΔH_v	heat of vaporization of bound water (J/kg)
ε_p	particle porosity (dimensionless)
ε_{pb}	porosity of the bed formed by the packed particles (dimensionless)
μ_{mx}	viscosity of vapor phase in the pores (kg/m s)
ρ	density (kg/m^3)
τ	tortuosity (dimensionless)

Superscripts

o	initial value

Subscripts

d	dried particle based material after primary drying
d,s	dried solution based material after primary drying
d,s,f	dried solution based material when frozen and sorbed water have been removed
e	effective
f	frozen particle based material
f,s	frozen solution based material
g	gas
I	region I, porous dried layer
II	region II, unsaturated porous frozen layer
in	inert gas
interf	moving interface
lp	lower heating plate
m	melting
mx	binary mixture of water vapor and inert gas
pd	primary drying stage
scor	scorch
t	total
up	upper heating plate
w	water vapor

Figure 2.2: Nomenclature. Liapis and Bruttini (2009), modified picture.

2.1.2 A multiscale approach

Some parameters present in the Liapis and Bruttini model can be calculated based on the chemical and physical properties of the sprayed solution (i.e., particle porosity), or obtained from the literature (i.e., permeability of the packed-bed for Darcy's physics, and the mean pore diameter formed from the packing of particles). However, these parameters can be very case-specific depending on the particles atomization conditions and their value can sensitively affect the model results.

A multiscale approach was proposed by Capozzi *et al*. (2019a) which firstly consists of generating realistic particles packings through computer simulation and, then, evaluate the packed-bed properties at the pore scale thanks to computational fluid dynamics (CFD) simulations. The properties obtained was used in a modified Liapis and Bruttini model for primary drying simulations. The workflow presented in Capozzi *et al*. (2019a) work is shown in Fig. 2.5.

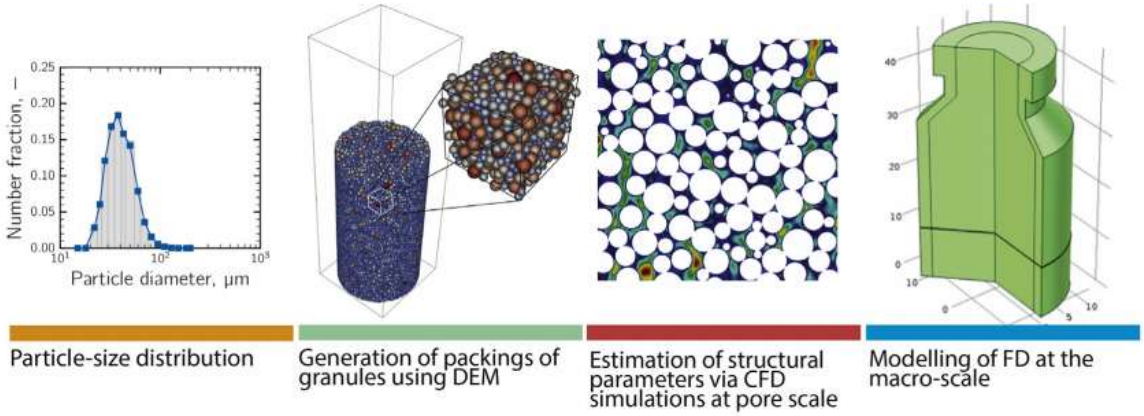

Figure 2.5: Workflow used to estimate packed-bed properties and primary drying behaviour. Reprinted from Capozzi *et al*., 2019a with modifications.

The generation of packed-bed of particles was conducted using the discrete element method (DEM). The particles were let falling into a cylindrical container. Newton's second law was used to describe translation and rotation and an evolution of the Hertz contact theory (Machado *et al*., 2012) was used to describe particle-to-particle and particle-to-walls interactions.

Once the packed-bed was generated, a cubic central portion was selected (representative elementary volume, REV). The extracted volume was used to conduct CFD simulations. According to authors, this method could provide four packed-bed properties (i.e., bed porosity, bed tortuosity, mean pore diameter, and bed permeability).

The voids between particles are responsible for the value of the properties estimated, hence an accurate mesh was needed as highlighted by authors. Note that during simulations particles were not meshed and were let as rigid spheres. The expressions to estimate the bed porosity and the mean pore diameter are reported below (Eqs. 2.1.31, and 2.1.32).

$$\varepsilon_b = \frac{V_{void}}{V_{tot}} \cong \frac{V_{mesh}}{V_{REV}} \tag{2.1.31}$$

$$d_p = \frac{4V_{void}}{S_{wetted}} \cong \frac{4V_{mesh}}{S_{mesh}} \tag{2.1.32}$$

The term V_{mesh} in Eqs. (2.1.31) and (2.1.32) represents the volume meshed. The term V_{REV} is the volume extracted from the cylindrical container. Eq. (2.1.32) is the mean hydraulic diameter of a porous material, hence S_{wetted} corresponds to the surface meshed.

To calculate the tortuosity factor, the authors used the tortuosity geometrical definition (i.e., the ratio of the path travelled by the fluid flowing in the REV to the shortest distance between REV inlet and outlet). Thus, the velocity field of the fluid was used in Eq. (2.1.33).

$$\tau_b = \frac{\int_{REV} |\boldsymbol{u}| dV}{\int_{REV} u_z dV} \tag{2.1.33}$$

The flowing direction was taken to be the z-direction.

At low Reynolds number the governing equation for a fluid flowing through a porous medium is the Darcy's law. Thus, to evaluate the permeability (Eq. 2.1.34) the authors solved the laminar Navier-Stokes equation imposing as boundary condition the pressure drop across the REV.

$$B_0 = \mu \left(\frac{\Delta p_z}{L_z}\right)^{-1} \frac{1}{V_{REV}} \int_{REV} u_z dV \tag{2.1.34}$$

In Eq. (2.1.34) the term μ represents the fluid viscosity and the flow direction is again taken to be the *z*-direction.

The authors obtained parameter values greatly similar to the one estimable from the literature.

Finally, after all the necessary parameters were evaluated, primary drying simulations were run. Some modifications to the Liapis and Bruttini model were done to carry out the drying. In the ice saturation definition, a distinction between greater and lower ice core diameter than particle diameter is made (Eq. 2.1.35).

$$\Phi_s = \begin{cases} \dfrac{\frac{4}{3}\varepsilon_p \pi {D^*}_p^3}{\frac{4}{3}\varepsilon_p \pi D_p^3} = \left(\dfrac{D_p^*}{D_p}\right)^3, & \text{for } D_p^* \le D_p \\ \dfrac{\frac{4}{3}\varepsilon_p \pi {D^*}_p^3 + \frac{4}{3}\pi\left({D^*}_p^3 - D_p^3\right)}{\frac{4}{3}\varepsilon_p \pi D_p^3}, & \text{for } D_p^* > D_p \end{cases} \tag{2.1.35}$$

In the energy balance equations (Eqs. 2.1.9, and 2.1.17) and in the water continuity equations (Eqs. 2.1.14, and 2.1.22) the bound water content was neglected.

2.1.3 Issues with the moving sublimation front

Fig. 2.6 shows the ice saturation behaviour during the primary drying of the packed-bed of particles in vial. The particles have a 90 μm diameter, the temperature of the heating shelf is 253 K, and the chamber pressure is 10 Pa.

The term L_p is the heigh of the packed-bed and was used by authors to normalize the ordinates. The moving sublimation front goes downward along the *z*-direction.

Across the moving interface there is not an ice saturation gradient, but a sharply change from Φ_s equal to 0 to Φ_s greater than 1 is obtained. This should be possible only if the water mass flux might not cross the sublimation front.

Furthermore, if the presence of the moving sublimation front involves a no flux condition across the interface, then the mean ice saturation in the frozen layer should not decrease during primary

drying. This is clearly shown in Fig. 2.7. The primary drying was carried out in the same conditions of Fig. 2.6, but with a shelf temperature of 238 K.

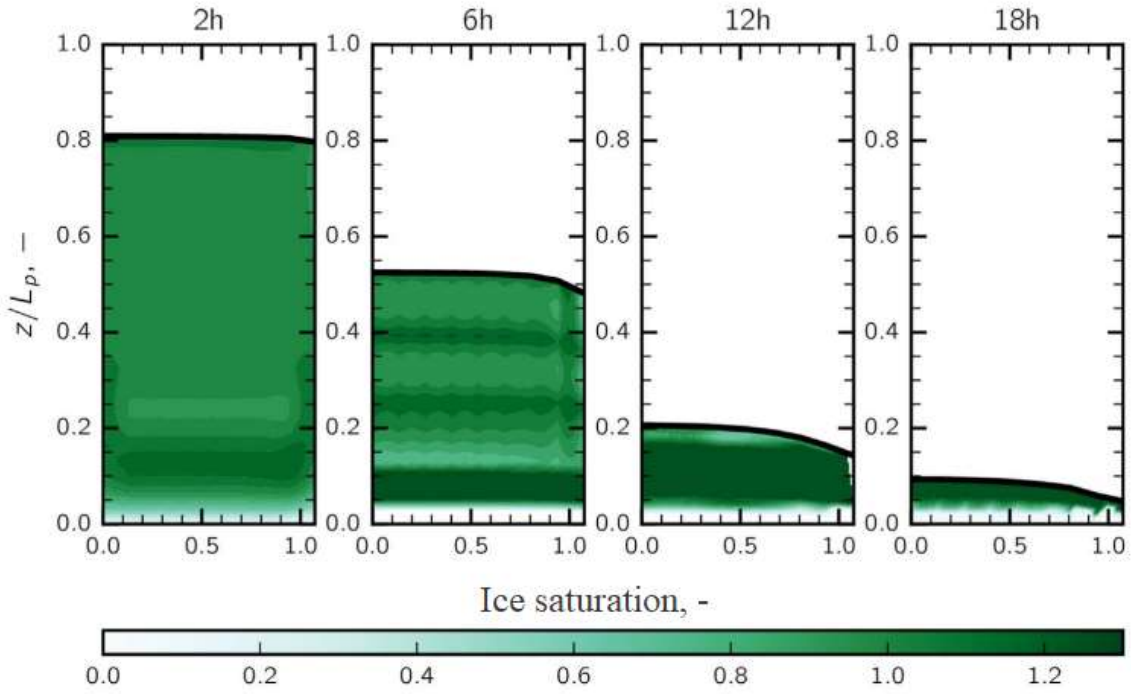

Figure 2.6: Ice saturation evolution of a particles packed-bed in vial.
Reprinted from Capozzi *et al*. (2019b) with modifications.

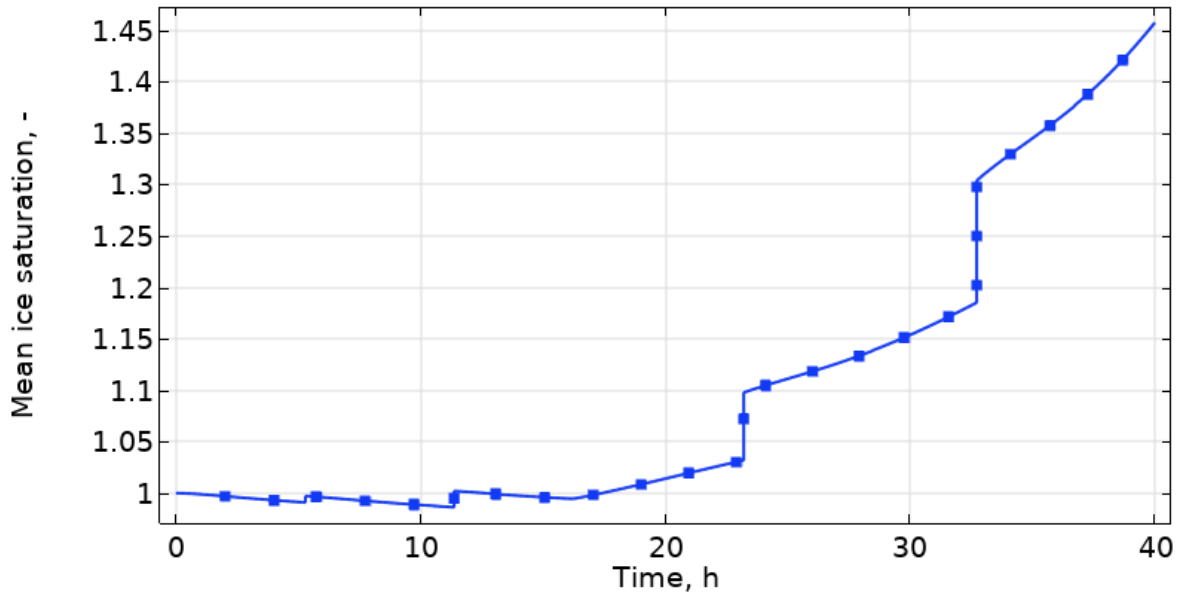

Figure 2.7: Evolution of the mean ice saturation in the frozen layer during primary drying.

The sublimated water is not able to cross the moving interface and starts recondensing in different zones of the frozen layer. The volume reduction of Layer II is forced by the velocity imposed at the moving front. The decreasing of the volume and the impossibility to reduce the initial mass of water bring to an uncontrolled condensation which results in too high values for the ice saturation as reported in Fig. 2.8. Therefore, an increasing trend for the mean ice saturation is obtained (Fig. 2.7). To plot the evolution shown in Fig. 2.6, the authors capped the ice saturation maximum value to 1.3.

In section 2.3 an alternative model developed to overcome the issues will be presented correlated to the use of a moving sublimation front thanks to a diffuse interface. Before, in section 2.2 a model for a single particle sublimation will be illustrated in detail. The development of this model was necessary to estimate a core parameter of the diffuse model (see Sec. 2.3), and to understand in which conditions heat transport mechanism become the controlling one instead of mass transport mechanism.

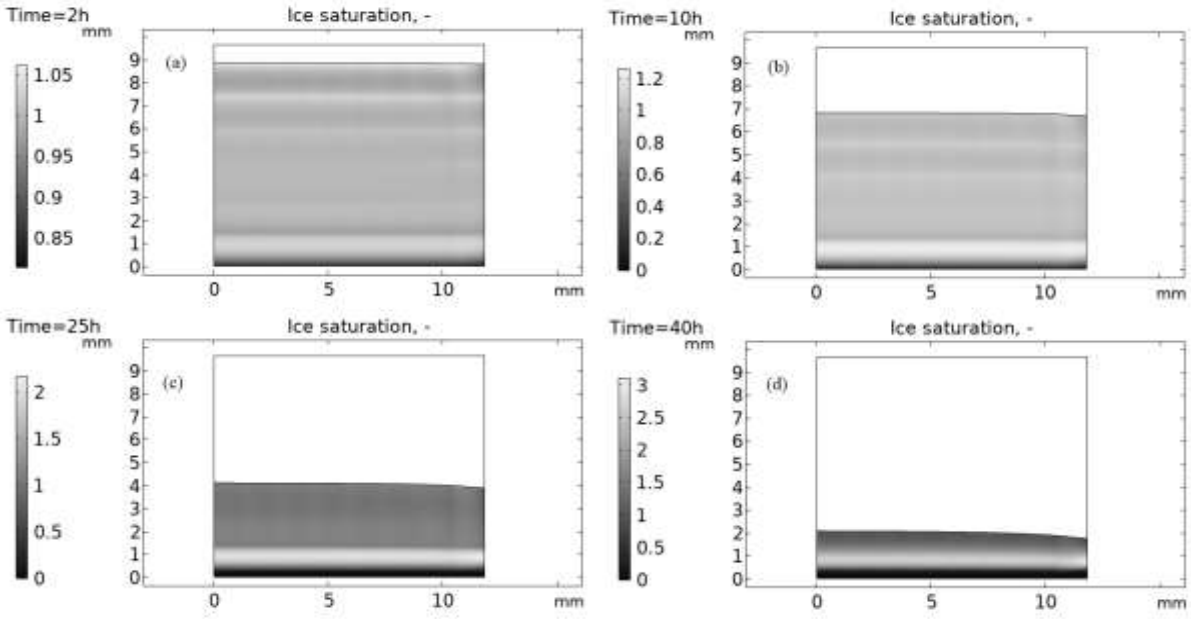

Figure 2.8: Ice saturation of a particles packed-bed in vial, shelf temperature 238 K. Non-capped evolution. (a) Time 2 h, (b) Time 10 h, (c) Time 25 h, (d) Time 40 h.

2.2 Model for single spherical particle lyophilization

In this section a model for single spherical particle lyophilization will be presented. The model was developed to estimate the so called sublimation kinetic constant (ν_s). This parameter will be a key one of the developed model for the primary drying of a packed-bed.

Fig. 2.9 shows a schematic representation of the spherical porous particle, which is divided into two domains (i.e., dried layer Ω_I, and frozen layer Ω_{II}) by a sublimation front. The interface moves along the r-direction through the centre of the sphere.

A list of symbols will be found at the end of the work to better understand nomenclature and how equation terms were estimated.

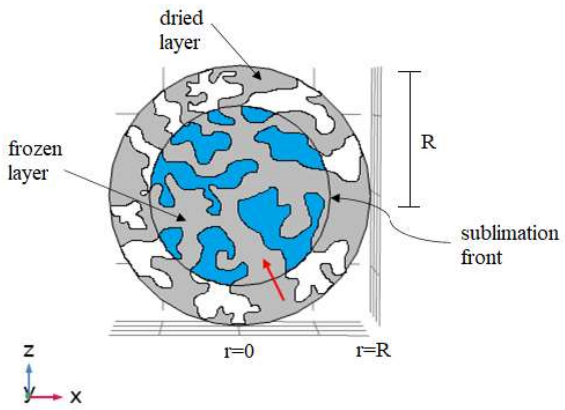

Figure 2.9: Spherical porous particle, schematic representation.

2.2.1 Heat transport in the frozen particle

In domain Ω_I, the energy balance equation (Eq. 2.2.1) must take into account the convection provided by the water vapour escaping from the inner pores of the particles.

$$\rho_I C_{p_I} \frac{\partial T_I}{\partial t} + \rho_{wv} C_{p_{wv}} \boldsymbol{u} \cdot \boldsymbol{\nabla T_I} + \boldsymbol{\nabla} \cdot (-k_I \boldsymbol{\nabla T_I}) = 0 \tag{2.2.1}$$

The term u in Eq. (2.2.1) represents the water vapour velocity. A weighted average where the weigh is the particle porosity ε_{p_I} was used to estimate the physical properties of layer Ω_I (Eqs. 2.2.2, and 2.2.3).

$$\rho_I C_{p_I} = \rho_{sol} C_{p_{sol}} (1 - \varepsilon_p) + \rho_{wv} C_{p_{wv}} \varepsilon_p \tag{2.2.2}$$

$$k_I = k_{sol}(1 - \varepsilon_p) + k_{wv} \varepsilon_p \tag{2.2.3}$$

In domain Ω_{II}, the energy balance equation (Eq. 2.2.4) does not present the convection term due to the presence of ice which full fills the pores.

$$\rho_{II} C_{p_{II}} \frac{\partial T_{II}}{\partial t} + \boldsymbol{\nabla} \cdot (-k_{II} \boldsymbol{\nabla T_{II}}) = 0 \tag{2.2.4}$$

Note that in Eq. (2.2.4) there is not a generation term because the latent heat contribution will be provided by the phase change interface velocity λ_{int} (Eq. 2.2.14) described in the following. Physical properties in Ω_{II} was estimated in the same way of Ω_{I}, switching from water vapour to ice.

The heat transfer initial condition depends on operative conditions of the spray-freezing step. If the final particle temperature of the frozen particles after the freezing step is T_i, the initial condition reads as follow (Eq. 2.2.5).

$$T_I = T_{II} = T_i \quad \text{for t} = 0, \ \ \forall \text{x, y, z} \tag{2.2.5}$$

The heat necessary to provide the lyophilization of the frozen particle has to be supplied as boundary condition. A raw estimation of this quantity can be done thinking of the single frozen particle as a bottom particle in a vial.

If K_v is the overall heat transfer coefficient between the heating shelf and the vial bottom (see Appendix B for further details), in steady-state condition it is possible to think that the heat exchanged at the frozen particle surface is equal to the heat provided by the shelf at the bottom of the vial (Q_{shelf}, Eq. 2.2.6) rescaled for a single particle (Eq. 2.2.7).

$$Q_{shelf} = K_v S_{bottom} (T_{source} - T_{bottom}) \tag{2.2.6}$$

$$-\boldsymbol{n} \cdot (-k \boldsymbol{\nabla T}|_{r=R_0}) = \frac{Q_{shelf}}{S_{part} N_{part}} \tag{2.2.7}$$

Note that, according to the definition of the K_v, the temperature at the bottom of the vial (packed-bed side) has been assumed to be equal to the frozen particle temperature at $r = R_0$.

In Eq. (2.2.6) the term S_{bottom} corresponds to the external surface of the vial bottom. The driving force is equal to the difference between the temperature of the shelf (i.e., T_{source}) and the temperature at the vial bottom. In Eq. (2.2.7) the term S_{part} represents the frozen particle surface, and N_{part} corresponds to the number of particles that are equally receiving the heat $\mathrm{Q_{shelf}}$ (see Appendix A for further details).

2.2.2 Mass transport in the frozen particle

To solve the energy balance equation in Ω_I (Eq. 2.2.1) the water vapour velocity must be estimated. Due to the presence of a porous matrix and low Reynolds number, the governing equation for mass transport is the Darcy's law (Eq. 2.2.9). Water vapour is a compressible fluid thus the continuity equation in layer Ω_I (Eq. 2.2.8) must take into account the density variation.

$$\varepsilon_p \frac{\partial \rho}{\partial t} + \left(\boldsymbol{\nabla} \cdot (\rho \mathbf{u})\right) = 0 \tag{2.2.8}$$

$$\boldsymbol{u} = -\frac{B_0}{\mu} \boldsymbol{\nabla p} \tag{2.2.9}$$

Note that in Eq. (2.2.8) it is possible to take out from the argument of the time derivative the porosity because in domain Ω_I it is a constant value.

The initial and boundary conditions are linked to the operative pressure at which the primary drying is carried out (Eqs. 2.2.10, and 2.2.11).

$$p = p_{vac} \text{ for } t = 0, \text{ in } \Omega_I \tag{2.2.10}$$

$$p|_{r=R_0} = p_{vac} \text{ for } t \geq 0 \tag{2.2.11}$$

The term p_{vac} is the vacuum pressure of the drying chamber.

2.2.3 Moving sublimation front

The estimation of the interface velocity is a major step to right evaluate the water quantity sublimated for unit time, the temperature distribution in both domains (i.e., Eqs. 2.2.1, and 2.2.4), and the volume reduction of the frozen layer.

To calculate the velocity λ_{int} a combination of heat (Eq. 2.2.12) and material (Eq. 2.2.13) balance across the interface must be performed. The energy balance equation is written thinking the thickness of the sublimation front to be infinitesimal.

$$-\Delta H_s N_{w,interf} + (-k_{II} \boldsymbol{\nabla T_{II}}) \cdot \boldsymbol{n_{interf}} - (-k_I \boldsymbol{\nabla T_I}) \cdot \boldsymbol{n_{interf}} = 0 \tag{2.2.12}$$

The term n_{interf} in Eq. (2.2.12) represents the normal vector to the moving sublimation front.

Thanks to the heat provided at the surface particle, the ice in domain Ω_{II} starts to sublimate. The mass flux generated flows from Ω_{II} to Ω_I passing through the sublimation front. This phenomenon has to be translated into the continuity equation at the interface.

$$-\boldsymbol{n}_{interf} \cdot \boldsymbol{N_{w,interf}} = \lambda_{int} \rho_{ice} \varepsilon_p \tag{2.2.13}$$

Note that the λ_{int} presents in Eq. (2.2.13) is the magnitude of the sublimation front velocity. The direction is opposite to the normal vector n_{interf}.

The combination of Eqs. (2.2.12), and (2.2.13) gives the expression to calculate the phase change interface velocity (Eq. 2.2.14).

$$\lambda_{int} = \frac{(-k_{II} \boldsymbol{\nabla T_{II}}) \cdot \boldsymbol{n_{interf}} - (-k_I \boldsymbol{\nabla T_I}) \cdot \boldsymbol{n_{interf}}}{\Delta H_s \rho_{ice} \varepsilon_p} \tag{2.2.14}$$

Lastly, to solve Eq. (2.2.14) a boundary condition at the interface is needed to calculate both temperature gradients. To express the thermodynamic equilibrium during the phase change at the interface, the Clausius-Clapeyron equation for water (Eq. 2.2.15) can be used.

$$\log p_{interf} = 28.89 - 2.19 \times 10^{-3} \frac{\Delta H_s}{T_{interf}} \tag{2.2.15}$$

The vapor tension p_{interf} is equal to the pressure of the water vapour at the boundary, which is known solving the mass transport equations in Ω_I. Note that Eq. (2.2.10) is valid in the entire dried domain, thus an initial condition to solve Eq. (2.2.15) is provided. Then, the T_{interf} value estimated from Eq. (2.2.15) can be used to solve temperature gradients in Eq. (2.2.14).

2.2.4 Sublimation kinetic constant estimation

In chemical reactions the time derivative of reactants concentration can be related to the same concentrations thanks to reaction kinetic constant (Eq. 2.2.16).

$$\frac{d[A]}{dt} = [A]^n [B]^m \nu \tag{2.2.16}$$

In Eq. (2.2.16) the terms *[A] ([B])* and ν are the reactant concentration and the kinetic constant respectively.

The same can be done with the mass flux at the interface, which can be seen as the time derivative of the water vapour surface generation in a first order chemical reaction system. To do that it is necessary to define a sublimation kinetic constant (Eq. 2.2.17).

$$N_{w,interf} = \left(\frac{p_{inter}}{RT_{inter}} - \frac{p_{vac}}{RT_{r=R_0}} \right) d_{dried} M_w \nu_s \tag{2.2.17}$$

The term d_{dried} in Eq. (2.2.17) represents the thickness of domain Ω_I, and it is used to guarantee the independence of the kinetic constant from mass transport resistance.

Thanks to Eq. (2.2.17) it is possible to correlate the sublimation kinetic constant to the physical properties of the frozen particle by solving the model presented in this section.

The value of ν_s represents the number of ice moles that are sublimating at the interface for unit of time.

As it will be shown in Chapter 3, the evaluation of ν_s from Eq. (2.217) brings to an asymptotic value. During the particle drying, the physical properties of the granule are changing due to the generation of the dried domain Ω_I, hence the value of ν_s must vary in time. A correct evaluation of the sublimation kinetic constant must give a value which decrease as long as the particle drying goes on (i.e., as long as the dried thickness increases).

To take into account this aspect and the generation of a new mass transfer resistance during the drying (i.e., d_{dried}) another equation to evaluate the sublimation kinetic constant was defined (Eq. 2.2.18).

$$\nu_s = \frac{N_{w,interf} S_{interf}}{\left(\frac{p_{inter}}{RT_{inter}} - \frac{p_{vac}}{RT_{r=R_0}} \right) M_w V_{ref}} \tag{2.2.18}$$

The term S_{interf} in Eq. (2.2.18) represents the surface of the sublimation front during the drying. Note that both values of the sublimation kinetic constant estimated from Eqs. (2.2.17), and (2.2.18) can be correlated to the ice fraction into the frozen particle through the dried layer thickness.

From Eq. (2.2.18) was obtained a decreasing behaviour of ν_s. When the particle is fully dried the value was set to be equal to zero.

The term V_{ref} in Eq. (2.2.18) represents a reference volume. As will be presented in Sec. 2.4, the software used to carry out the simulation of the packed-bed run a finite element method. The equations in the software are always referred to the finite element volume of the mesh, hence as reference volume for the sublimation kinetic constant evaluation was chosen to consider also the packed-bed porosity (Eq. 2.2.19).

$$V_{ref} = \frac{\frac{4}{3}\pi R_0^3}{1 - \varepsilon_{pb}} \tag{2.2.19}$$

In Eq. (2.2.19) the term ε_{pb} represents the packed-bed porosity.

The single particle model was used to transfer a microscopic information (i.e., the particle behaviour during the drying) to a bidisperse macroscopic system (i.e., the packed-bed) through the evaluation of the sublimation kinetic constant.

Both the values calculated for v_s will be used in the primary drying model to describe the mass generation in a particles packed-bed.

2.3 *Diffuse interface model*

In this section a model for the primary drying step of particles packed-bed in vial is presented. Compared to the previous models (see Secs. 2.1, and 2.2), the moving sublimation front is removed. Thus, one single domain in which physical properties change with the value of ice saturation has to be realized. Moreover, the interface is no longer imposed but obtained from a diffusive mechanism described in the following.

Fig. 2.10 shows a schematic representation of the packed-bed during drying.

A bidisperse system was adopted to describe the entire packed-bed. The model was developed assuming that a controlled amount of inert gas (nitrogen) is sent to the system to manipulate chamber pressure. The following equations are presented thinking water as solvent.

A list of symbols will be found at the end of the work.

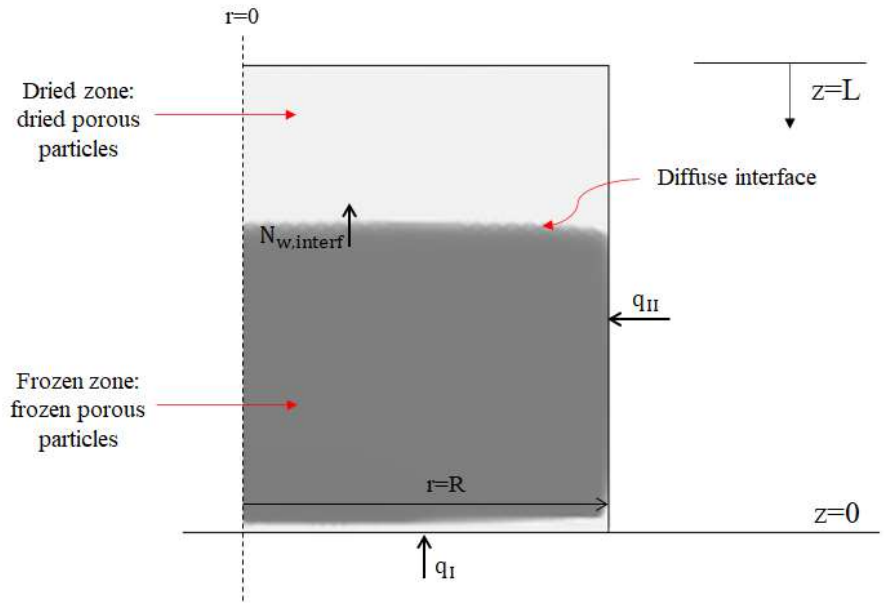

Figure 2.10: Packed-bed in vial during drying, diffuse interface.

2.3.1 Ice saturation in the frozen packed-bed

The physical properties of the bed and the transport equations are all linked to the ice saturation variable. To define this quantity, it is necessary to estimate the initial amount of water that has to be sublimated during the drying (Eq. 2.3.1).

$$C_{w,i} = \frac{\left(1 - \varepsilon_{pb}\right)\varepsilon_p \rho_{ice}}{M_w} \tag{2.3.1}$$

In the Eq. (2.3.1) it has been supposed that the frozen particles pores are full filled with ice (i.e., $\varepsilon_p \rho_{ice}$). Thanks to the bidisperse system adopted, it is possible to express the amount of volume occupied by particles as $1 - \varepsilon_{pb}$.

The ice saturation is defined through the fraction between the amount of water that is phase changing during the primary drying to the initial amount of water that has to be sublimated (Eq. 2.3.2).

$$S = 1 - \frac{C_{w,int}}{C_{w,i}} \tag{2.3.2}$$

Both $C_{w,i}$ and $C_{w,int}$ are intensive variables, thus the ice saturation value estimated through Eq. (2.3.2) can be used to describe the mechanisms that are occurring in the bed at particles scale level. If in some bed zones the amount of sublimated water is lower than the condensed one, the variable $C_{w,int}$ will be negative and the ice saturation will assume a value greater than 1.

Note that the term ε_{pb} in Eq. (2.3.1) corresponds to the packed-bed porosity when the channels between particles are not filled with ice. This is equivalent to say that the starting condition for the packed-bed is an ice saturation value equal to 1.

Thanks to the use of Eq. (2.3.2) it is possible to define the physical properties of the packed-bed in relations with the ice saturation level.

The total bed porosity ε_{tot} of the bidisperse system (Eq. 2.3.3) must decrease if the pores between particles are filled with ice.

$$\varepsilon_{tot} = \begin{cases} \varepsilon_{pb} & \text{for } S < 1 \\ \varepsilon_{pb} + \left(1 - \varepsilon_{pb}\right)\varepsilon_p (1 - S) & \text{for } S \geq 1 \end{cases} \tag{2.3.3}$$

Note that when the channels are full of ice, the ice saturation reach a value that is able to null the total porosity. This will provide a local stop condition for mass transport.

Bed specific heat capacity (Eq. 2.3.4), bed thermal conductivity (Eq. 2.3.5), and total bed density (Eq. 2.3.6) can be defined using both Eqs. (2.3.2), and (2.3.3). The physical properties of the entire bed changes according to the amount of ice still present in the particles and bed pores.

$$C_{p_{bed}} = (1 - \varepsilon_{tot}) \left(C_{p_f} S + C_{p_d} (1 - S) \right) + \varepsilon_{tot} C_{p_{gas}} \tag{2.3.4}$$

$$k_{bed} = (1 - \varepsilon_{tot}) \left(k_f S + k_d (1 - S) \right) + \varepsilon_{tot} k_{gas} \tag{2.3.5}$$

$$\rho_{bed} = (1 - \varepsilon_{tot}) \left(\rho_f S + \rho_d (1 - S) \right) + \varepsilon_{tot} \rho_{gas} \tag{2.3.6}$$

The terms C_{p_f} and C_{p_d} in Eq. (2.3.4) correspond to the specific heat capacity of the frozen part of the bed and the specific heat capacity of the dried part of the bed, respectively. The term

$C_{p_{gas}}$ in Eq. (2.3.4) is the specific heat capacity of the gas mixture flowing through the porous matrix. The same can be assumed for the terms in Eqs. (2.3.5), and (2.3.6). For further details on how these quantities are estimated, see Appendix B.

2.3.2 Heat transport in the frozen packed-bed

In the energy balance equation (Eq. 2.3.7) of the packed-bed has to be considered the convective mechanisms provided by the gas flowing in the porous matrix and the heat source generated by the phase change of the water.

$$\rho_{bed} C_{p_{bed}} \frac{\partial T}{\partial t} = \boldsymbol{\nabla} \cdot (k_{bed} \boldsymbol{\nabla T}) + \boldsymbol{\nabla} \cdot \left(k_{glass} \boldsymbol{\nabla T}\right) - C_{p_{gas}} \left(\boldsymbol{\nabla} \cdot (\boldsymbol{N_t} T)\right) + Q_{gen} \tag{2.3.7}$$

The term N_t in Eq. (2.3.7) represents the total mass flux of the gas phase. Due to the presence of the vial, usually made by glass, a term for heat transfer in a different material it is present.

The quantity Q_{gen} is the heat generated by sublimation or condensation (Eq. 2.3.8) and can be described as the amount of heat exchanged for unit of volume to provide the phase change of water.

$$Q_{gen} = -G_w \Delta H_s M_w \tag{2.3.8}$$

Note that the term G_w in Eq. (2.3.8) describes the moles of water for unit of time and volume that are sublimating or condensing (see Sec. 2.3.3 for further details).

The boundary condition needed to carry out the primary drying is the heat flux at the bottom of the vial, coming from the heating shelf where the stock of vials is placed (Eq. 2.3.9).

$$-\boldsymbol{n} \cdot (-k_{bed} \boldsymbol{\nabla T}|_{z=0}) = K_v \left(T_{shelf} - T_{z=0}\right), \quad \text{for} \quad t > 0, \quad \forall r \tag{2.3.9}$$

In Eq. (2.3.9) the term K_v corresponds to the overall heat transfer coefficient between the bottom of the vial and the shelf. This quantity needs to be estimated taking into account not only the contact area between the heating source and the vial, but also the void that can be present due to the bottom shape of the vial. According to the type of vial, hence the bottom shape, the value of the K_v can be different even if the external vial bottom diameter and the temperature of the heating shelf (T_{shelf}) are the same (see Appendix B for further details about how the heat transfer coefficient has been evaluated).

The primary drying can be carried out in different apparatus. Some of them are able to minimize the interaction between vials and the surrounding environment to remove external heat flux source by radiations. If the primary drying is carried in equipment where these interactions are not mitigated, an additional heat flux has to be provided at the vial surface.

Additive boundary conditions can be provided to describe the heat exchange during the drying. Two main configurations were explored for the simulated packed-bed. First, a set up where the top bed surface is adiabatic (i.e., no heat by radiation was supplied). Then, a configuration where the top bed surface was described as a blackbody which take the radiation by the vial cap (Eq. 2.3.10). In this last set up, the vial cap was thought as a blackbody who receive the irradiated heat from the upper shelf (Eq. 2.3.11).

$$-\boldsymbol{n} \cdot (-\boldsymbol{k_{glass}} \boldsymbol{\nabla T}|_{z=H_{tot}^-}) = \sigma \left(T_{shelf}^4 - T_{z=H_{tot}^-}^4\right), \quad \text{for} \quad t > 0, \quad \forall r \tag{2.3.10}$$

$$-\boldsymbol{n} \cdot (-\boldsymbol{k}_{bed} \boldsymbol{\nabla T}|_{z=L^-}) = \sigma (T_{irr}^4 - T_{z=L^-}^4), \quad \text{for} \quad t > 0, \quad \forall r \tag{2.3.11}$$

In Eq. (2.3.10) H_{tot} represents the total height of the vial until the top surface of the vial cap. The term T_{irr} in Eq. (2.3.11) represents the mean temperature reached in the vial cap during the drying.

The initial condition depends on the operative conditions of the spray-freeze stage. It has been supposed that in both packed-bed and vial material the initial condition (i.e., initial temperature) is the same (Eq. 2.3.12).

$$T_{bed} = T_{glass} = T_i \quad \text{for} \quad t = 0, \ \forall r, z \tag{2.3.12}$$

2.3.3 Mass transport in the frozen packed-bed

In the porous matrix of the packed-bed there are two flowing components that constitute the gas phase. One of them is the water vapour, generated thanks to the ice sublimation. The other one is the inert gas (usually nitrogen) used to control the vacuum level in the drying chamber. The material balances in the packed-bed must be expressed for both the components (Eqs. 2.3.13, and 2.3.14).

$$\frac{\partial(\varepsilon_{tot} C_w)}{\partial t} = -\boldsymbol{\nabla} \cdot \boldsymbol{N_w} + G_w \tag{2.3.13}$$

$$\frac{\partial(\varepsilon_{tot} C_{in})}{\partial t} = -\boldsymbol{\nabla} \cdot \boldsymbol{N_{in}} \tag{2.3.14}$$

Both the mass fluxes terms in Eqs. (2.3.13), and (2.3.14) are estimated thanks to the dusty-gas model (DGM). The expressions of the coefficients needed to solve the DGM equations (Eqs. 2.3.15, and 2.3.16) are reported in Appendix B.

$$\boldsymbol{N_w} = -\frac{M_w}{RT}(c_1 \boldsymbol{\nabla p_w} + c_2 p_w \boldsymbol{\nabla P}) \tag{2.3.15}$$

$$\boldsymbol{N_{in}} = -\frac{M_{in}}{RT}(c_3 \boldsymbol{\nabla p_{in}} + c_4 p_{in} \boldsymbol{\nabla P}) \tag{2.3.16}$$

When the ice saturation reaches a value able to null the total bed porosity, the DGM coefficients go to zero and the water (or inert) transport through the bed is no longer possible (see Appendix B for further details).

Note that to solve both the expressions above, it is necessary to express the total pressure in the bed (Eq. 2.3.17).

$$P = p_w + p_{in} \tag{2.3.17}$$

The partial pressure of the two components can be estimated thanks to the use of the ideal gas law. The total mass flux across the bed needed to solve Eq. (2.3.7) can be expressed as follow (Eq. 2.3.18).

$$\boldsymbol{N_t} = \boldsymbol{N_w} + \boldsymbol{N_{in}} \tag{2.3.18}$$

In Eq. (2.3.1) is present the water generation term G_w. To evaluate this term a thermodynamic equilibrium must be considered. If the partial pressure of water vapour is lower than the ice vapor tension, the ice in the bed starts to sublimate, the G_w term is positive and a fraction of the heat supplied to the bed is subtracted for the sublimation (i.e., endothermic phenomenon, Eq. (2.3.8) is negative). Instead, if the partial pressure of water vapour is higher than the ice vapour tension, the vapour starts to condense providing exothermic phenomena and a negative G_w.

Thus, the water generation expression (Eq. 2.3.19) needs to separate these two different phenomena.

$$G_w = \begin{cases} \left(\frac{p_w^{sat}}{RT} - C_w\right)\nu_s & \text{if } \left(\frac{p_w^{sat}}{RT} - C_w\right) \geq 0 \\ \left(\frac{p_w^{sat}}{RT} - C_w\right)\nu_c & \text{if } \left(\frac{p_w^{sat}}{RT} - C_w\right) < 0 \end{cases} \tag{2.3.19}$$

The terms ν_s and ν_c in Eq. (2.3.19) are the lyophilization and condensation kinetic constants, respectively. These represent the water moles that are sublimating (or condensing) for unit of time. As previous discussed in Sec. 2.2, the kinetic constant ν_s has been evaluated thanks to the single particle model. The generation term G_w is an intensive quantity, hence it was possible to pass from a microscale evaluation of the kinetic constant (single particle model) to a macroscale application. To do that, it has been supposed that the number of water moles which leave the particle sublimation interface (see Sec. 2.2.4) is equal to the number of water moles that sublimate in the packed-bed for unit of volume.

The condensation kinetic constant ν_c has been fixed as a parameter value for the model simulations.

The ice vapour tension needed in Eq. (2.3.19) is given by Marti and Mauersberger expression (Eq. 2.3.20).

$$\log_{10} p_w^{sat} = -\frac{2663.5}{T} + 12.537 \tag{2.3.20}$$

The boundary condition chosen is a constant composition of the gas phase at the top surface of the packed-bed (Eq. 2.3.21). There, the composition is equal to that in the drying chamber. It has been supposed an atmosphere of 95% of water vapour and 5% of inert gas.

$$C_{w,top} = \frac{0.95 p_c}{RT}, \quad C_{in,top} = \frac{0.05 p_c}{RT} \quad \text{for } t > 0, \qquad z = L, \qquad \forall r \tag{2.3.21}$$

The initial condition (Eq. 2.3.22) is linked to Eq. (2.3.12) thanks to the ideal gas law. Note that when the drying stage starts, the packed-bed is in saturated conditions and the overall bed pressure corresponds to the vacuum pressure chosen.

$$C_{w,i} = \frac{p_w^{sat}(T_i)}{RT_i}, \quad C_{in,i} = \frac{p_c - p_w^{sat}(T_i)}{RT_i} \quad \text{for } t = 0, \qquad \forall r, z \tag{2.3.22}$$

2.3.4 Phase changing water

To solve Eq. (2.3.2), it is necessary to estimate the amount of water that is phase changed in time.

The generation term G_w represents the amount of water that is phase changed for unit of time. Thus, the time integral of Eq. (2.3.19) gives the amount of water (Eq. 2.3.23) needed to calculate the ice saturation value.

$$C_{w,int} = \int_0^t G_w dt \tag{2.3.23}$$

The initial conditions must be consistent with the previous assumptions (i.e., Eq. 2.3.1), hence the initial amount of water that is phase changed should be null (Eq. 2.3.24). Moreover, it is necessary to give a consistent integral argument initial condition (Eq. 2.3.25).

$$C_{w,int,i} = 0 \quad \text{for} \quad t = 0, \ \forall r, z \tag{2.3.24}$$

$$G_{w,i} = 0 \quad \text{for} \quad t = 0, \ \forall r, z \tag{2.3.25}$$

When sublimation occurs the water generation G_w is positive, the amount of water phase changed rise and the ice saturation starts to decrease. Instead, when condensation occurs, the term G_w is negative and a decreasing $C_{w,int}$ increases the ice saturation value.

Note that, when the condensation is predominant compared to sublimation, a negative value of Eq. (2.3.23) it is possible. Thus, the ice saturation value (Eq. 2.3.2) can reach values higher than 1, slowing the mass transport until channels in the bed will be full of ice and ε_{tot} will become null.

When the previous described phenomenon occurs, the sublimation kinetic constant value was set to be equal to the one evaluated for an ice fraction equal to 1.

2.4 *Software and models simulations*

The simulations were run on COMSOL Multiphysics, a software based on the finite element method (FEM). After the parameters and the geometry of the simulations were loaded, a mesh, which divides the entire object of study into numerous finite elements, were created.

The FEM method evaluate the solution of the numerical problem into each finite element as a linear combination of functions.

If not indicated, the parameters in Tables 2.1 and 2.2 were not changed in the various simulations.

2.4.1 Single particle model parameters

The particle simulated was a mannitol porous granule. In Table 2.1 a list of the input parameters and their value is presented.

The particle radius R_0 was evaluated as mean value from particle size distribution. The distribution and the final value were obtained by Dott.ssa M. A. Adali (see Sec. 2.5 for further detail).

The parameter Zi is the initial dried domain thickness. The software is not able to generate new domain, hence an initial gap value must be provided to COMSOL in order to allow the expansion of domain Ω_I during the drying.

The value X in the d_{pore} definition is the number of pores which can be present in the particle if they would be lined up along the particle diameter direction. In this work will be presented four simulations, each one with a different value of X.

The Carman-Kozeny expression was used to evaluate the particle permeability.

Last, the following expressions were used to evaluate the specific heat capacity and the thermal conductivity of the solid phase (Eqs. 2.4.1, and 2.4.2) and the water vapour viscosity (Eq. 2.4.3).

$$C_{p_{sol}} = 0{,}003437T + 1{,}272966 \tag{2.4.1}$$

$$k_{sol} = (0{,}0047 + 0{,}0027)T + 0{,}5509 - 0{,}096 \tag{2.4.2}$$

$$\mu = 18{,}4558 \times 10^{-7} \frac{T^{1,5}}{T + 650} \tag{2.4.3}$$

The expression of Eq. (2.4.3) was taken from the work of Liapis and Bruttini (2009). To further details on how Eqs. (2.4.1), and (2.4.2) were obtained see Sec. 2.5.1.

Table 2.1: Single particle model input parameters.

Parameter	Value	Unity	Description
ΔHs	2.79E+06	J/kg	Latent heat of sublimation
B_0	$d^2_{pore}/180 \cdot d^3_{pore}/(1-\varepsilon_p)^2$	m²	Particle permeability
Cp_{ice}	1967.8	J/(kg·K)	Ice specific heat capacity
Cp_{wv}	1674.7	J/(kg·K)	Vapor specific heat capacity
d_{pore}	$2 \cdot R_0/X$	m	Particle pore diameter
D_{vial}	0.024	m	External vial diameter
D_v	D_{vial}-s	m	Internal vial diameter
k_{ice}	2.1	W/(m·K)	Ice thermal conductivity
k_{wv}	0.025	W/(m·K)	Vapor thermal conductivity
Mw	0.018	kg/mol	Water molecular weight
Pc	15	Pa	Vacuum chamber pressure
R_0	1.62E-05	m	Particle radius
s	0.001	m	Vial thickness
T_i	233.15	K	Initial temperature
T_{source}	253.15	K	Source temperature
Zi	1.00E-06	m	Initial dried gap
ε_p	0.95	-	Particle porosity
ρ_{ice}	913	kg/m³	Ice density
ρ_{sol}	1468	kg/m³	Solid phase density

2.4.2 Single particle model geometry and physics

The single particle simulation has been run using a 3D spherical geometry. Only half of the sphere with symmetry boundary conditions were used to lower the computational cost. Fig. 2.11 shows a representation of the granule in COMSOL.

The Darcy's law COMSOL physic was set to simulate the mass transport in the particle. Note that the physic must be selected only for domain Ω_I, because in the frozen domain there is no flowing fluid. Fig. 2.12 shows all the conditions set in the COMSOL physic.

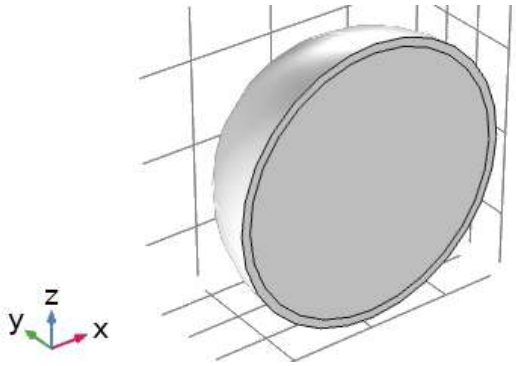

Figure 2.11: 3D half-sphere simulated.

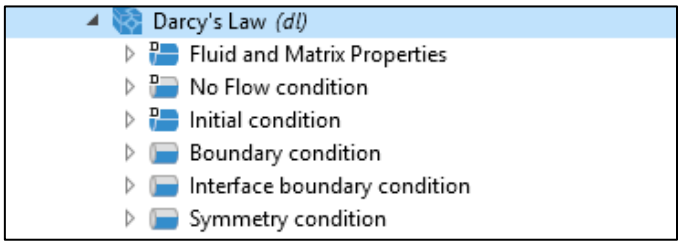

Figure 2.12: Darcy's Law COMSOL physic.

Note that the no flow condition in the mass transport COMSOL physic has not applications. All the boundaries have different conditions and the no flow one is overridden.

To simulate the heat transport, the heat transfer in porous media COMSOL physic was set. It is necessary to separate dried and frozen domains to impose different physical properties. Fig. 2.13 shows all the conditions set in the COMSOL physic.

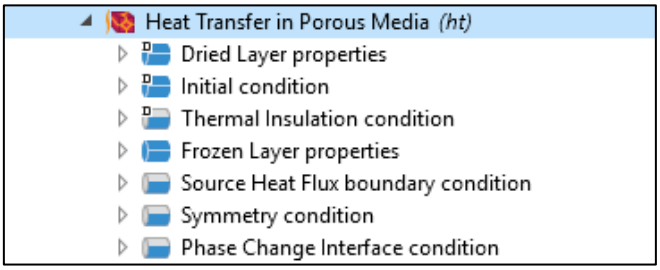

Figure 2.13: Heat transfer in porous media COMSOL physic.

Note that the thermal insulation condition in the heat transport COMSOL physic has not applications. All the boundaries have different conditions and the thermal insulation one is overridden.

Lastly, the deformed geometry mathematics COMSOL physic was set to allow the expansion of the dried domain during the drying. Fig. 2.14 shows all the conditions set in the COMSOL physic.

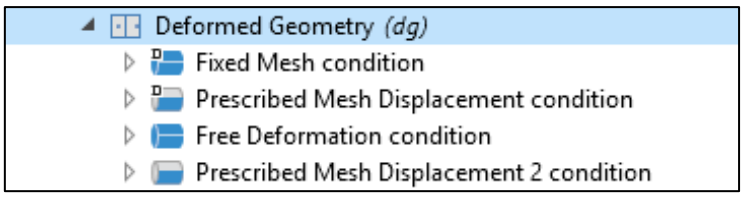

Figure 2.14: Deformed geometry COMSOL physic.

The first prescribed mesh displacement condition was applied at the particle surface. To avoid a total volume change during the drying, the displacement in all the possible directions was set to be null. The second prescribed mesh displacement was applied to both dried and frozen domains to allow the expansion of Ω_I.

Note that the fixed mesh condition in the deformed geometry COMSOL physic has not applications. All the boundaries have different conditions and the fixed mesh one is overridden.

2.4.3 Single particle model mesh

A free tetrahedral predefined setting was used to mesh the geometry. Fig. 2.15 shwows a representation of the granule mesh in COMSOL.

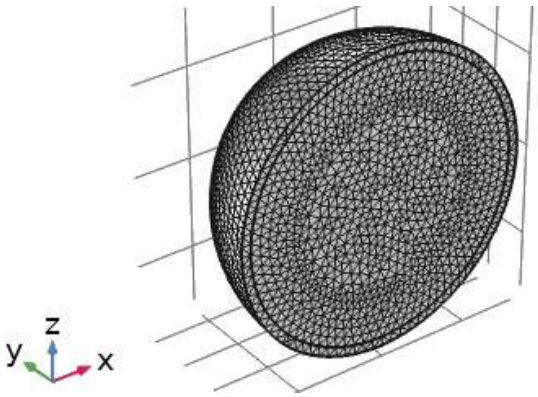

Figure 2.15: Particle mesh.

The mesh independence study will be presented in the following chapter. Fig. 2.16 shows the finite element size parameters.

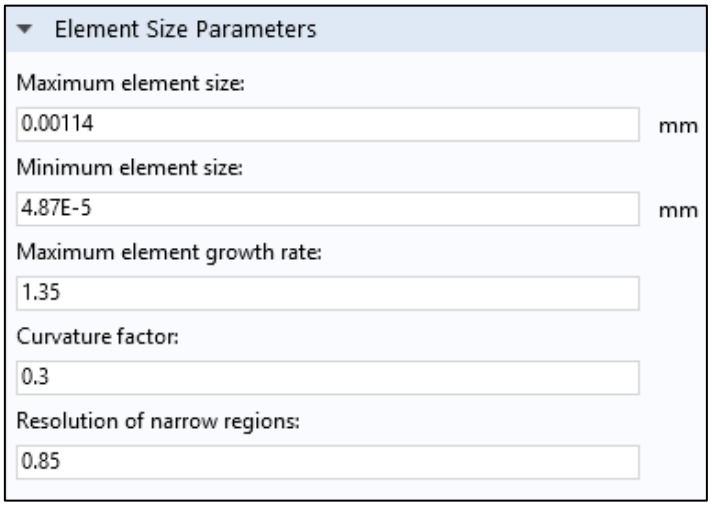

Figure 2.16: Finite element size parameters.

Note that to maintain the mesh accuracy a remeshing while the simulation runs is required. A remeshing condition after every 20 seconds was set.

To stop the simulation when the particle is dried and avoid simulation errors a stop conditions is needed (Eq. (2.4.4)).

$$Stop\ condition:\ \frac{\left(\frac{d_{dried}}{2}\right)^3 \varepsilon_p}{R_0^3} - 0.02 < 0 \tag{2.4.4}$$

The condition imposed in Eq. (2.4.4) is equivalent to say that the residual frozen water in the entire particle volume is lower than 2%.

2.4.4 Diffuse interface model parameters

The packed-bed simulated was constituted by frozen mannitol particles. In Table 2.2 a list of the input parameters and their value is presented.

Table 2.2: Diffuse interface model input parameters.

Parameter	Value	Unity	Description
ΔHs	2.79E+06	J/kg	Latent heat of sublimation
B_0	1.87E-11	m²	Dried bed permeability
Cp_{ice}	1967.8	J/(kg·K)	Ice specific heat capacity
Cp_{glass}	840	J/(kg·K)	Glass specific heat capacity
D_{part}	32.48E-06	m	Particle diameter
d_{pore}	1.90E-05	m	Bed pore diameter
D_{vial}	0.024	m	External vial diameter
D_v	D_{vial}-s	m	Internal vial diameter
k_{ice}	2.1	W/(m·K)	Glass thermal conductivity
k_{glass}	1.0014	W/(m·K)	Ice thermal conductivity
M_w	0.018	kg/mol	Water molecular weight
M_{in}	0.02888	kg/mol	Nitrogen molecular weight
Pc	15	Pa	Vacuum chamber pressure
s	0.001	m	Vial thickness
T_i	233.15	K	Initial temperature
Z_0	0.015	m	Initial loaded product height
ε_p	0.95	-	Particle porosity
ε_{pb}	0.39	-	Bed porosity
ρ_{ice}	913	kg/m³	Ice density
ρ_{sol}	1468	kg/m³	Solid phase density
ρ_{glass}	2600	kg/m³	Glass density
τ	1.33	-	Bed tortuosity

To further details on how the bed physical properties (i.e., porosity, tortuosity, dried bed permeability, and diameter of the pores within the bed) were obtained, see Sec. 2.5.1.

The value of the overall heat transfer coefficient at the bottom of the vial was evaluated according to Eq. (2.4.5).

$$K_v = 5.07 + \frac{1.22 p_c}{1 + 0.021 p_c} \tag{2.4.5}$$

Note that the gravimetric value of K_v (i.e., Eq. 2.4.5) was used in the adiabatic simulation of the bed. When the simulated vial was irradiated by additive heat fluxes, a reduction of the 40% was applied to the overall heat transfer coefficient to provide the same total amount of heat in all the simulations.

To further details on how the coefficients present in Eq. (2.4.5) were obtained, see Sec. 2.5.1.

The gas viscosity, the specific heat capacity of mannitol, and the thermal conductivity of mannitol used in the simulation were the same presented for the single particle model (Eqs. 2.4.1, 2.4.2, and 2.4.3).

The binary diffusivity (Eq. 2.4.6) necessary to evaluate the effective diffusivity (see Appendix B) were obtained according to Reitzle *et al*. (2019).

$$D_{w,in} = 0.2315 \left(\frac{T}{273.15}\right)^{2.5595} \left(\frac{101325}{p}\right) \tag{2.4.6}$$

Last, the thermal conductivity of the gas phase at atmospheric pressure (Eq. 2.4.7) was taken from the model of Capozzi *et al.* (2019a).

$$k_{gas}^{atm} = 3.94 \cdot 10^{-3} \sqrt{T} \Bigg/ \left(\frac{1.16145}{\left(\frac{T}{809.1}\right)^{0.14874}} + \frac{0.52487}{e^{\left(0.7732\left(\frac{T}{809.1}\right)\right)}} + \frac{2.16178}{e^{\left(2.43787\left(\frac{T}{809.1}\right)\right)}} \right) \tag{2.4.7}$$

Fig. 2.17 shows the temperature shelf profile imposed. To further detail see Sec. 2.5.

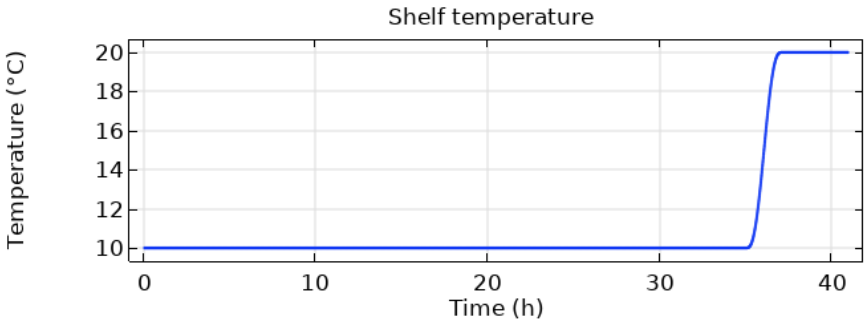

Figure 2.17: Shelf temperature during drying.

2.4.5 Diffuse interface model geometry and physics

The packed-bed simulations have been run using a 2D axisymmetric geometry. The vial simulated was a 10R vial which has an internal diameter of 22 mm and thickness of 1 mm. In Fig. 2.18 is shown a representation of the vial in COMSOL.

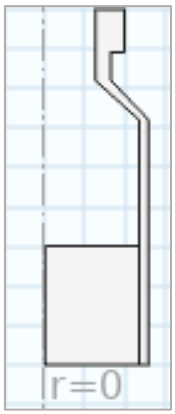

Figure 2.18: 2D axisymmetric vial simulated.

The transport of diluted species in porous media COMSOL physic was used to simulate the mass transfer in the packed-bed. It was necessary to express the water generation term in this physic to provide Eq. (2.3.17) to the software. Fig. 2.19 shows all the conditions set in the COMSOL physic.

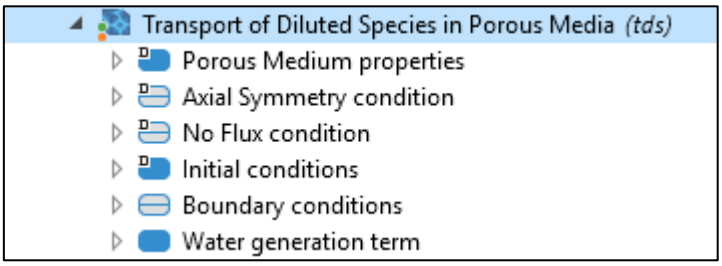

Figure 2.19: Transport of diluted species in porous media COMSOL physic.

Note that the no flux condition applies only at vial walls. At the other boundaries, initial conditions, boundary conditions or axial symmetry condition override the no flux one.

The heat transfer in porous media COMSOL physic was used to simulate the heat transport in the packed-bed. The heat transfer in glass applies only at the vial material, instead the heat flux at bottom describes the interaction between heating shelf and vial bottom. Fig. 2.20 shows all the conditions set in the COMSOL physic.

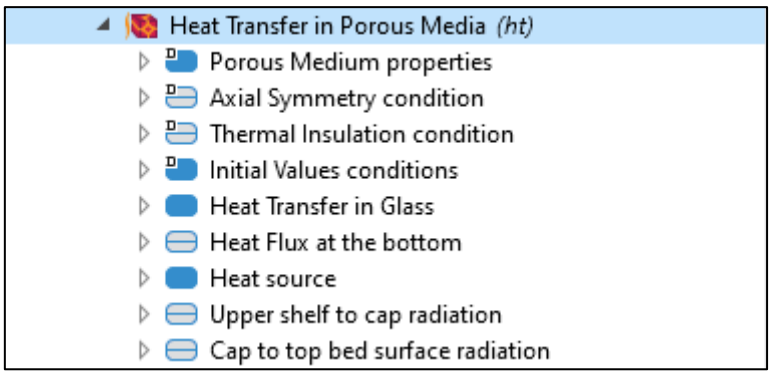

Figure 2.20: Heat transfer in porous media COMSOL physic.

The heat source is linked to the water generation term in the mass transport physic. The amount of water that should phase change is evaluated by the software, then the value is transmitted to

the heat transport physic which estimate the heat necessary to allow the sublimation or the condensation.

Note that to simulate the adiabatic condition at the top bed surface, the radiation physics were disabled.

The thermal insulation condition applies only at the perimetral vial walls (heat transfer through the internal vial walls is allowed). When in the simulation are set radiation boundary conditions too, the thermal insulation condition is overridden at the perimetral vial walls of interest.

To evaluate the amount of water phase changed during time, hence the ice saturation term (Eqs. 2.3.1, and 2.3.2) it was necessary to run an ordinary differential equation (ODE) COMSOL physic (Fig. 2.21).

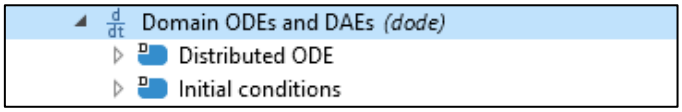

Figure 2.21: Ordinary differential equation COMSOL physic.

Note that in the ODE, the concentration of water phase changed during time was set as dependent variable and the water generation term was set as source term.

2.4.6 Diffuse interface model mesh

According to Alexeenko *et al*. (2009), the mesh element should be fine enough that the gas properties change in each cell is small. Fig. 2.22 shows a representation of the bed mesh in COMSOL.

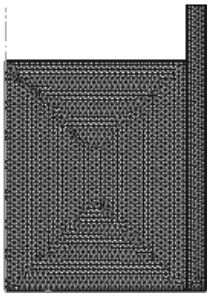

Figure 2.22: Packed-bed mesh.

A free tetrahedral customized setting was used to mesh the geometry. Fig. 2.23 shows the finite element size parameters.

The mesh independence study will be presented in the following chapter.

Figure 2.23: Finite element size parameters.

2.4.7 Design of simulations

In Table 2.3 a schedule of the simulations carried out is presented. Each simulation is identified by a label which will be used to properly refer in the following chapters.

Table 2.3: Simulation schedule.

Model	**Parameter 1**	**Parameter 2**	**Label**
Single particle	X=1000	-	SP.1000
Single particle	X=100	-	SP.100
Single particle	X=60	-	SP.60
Single particle	X=30	-	SP.30
Single particle	X=10	-	SP.10
Single particle	X=5	-	SP.5
Single particle	X=100	Pc=10 Pa	SP.100.10
Single particle	X=1000	$R_0 = 250$ μm	SP250.1000
Single particle	X=100	$R_0 = 250$ μm	SP250.100
Diffuse interface, adiabatic	ν_s from SP.100, Eq. (2.2.17)	ν_c=1 s^{-1}	DIA.100
Diffuse interface, adiabatic	ν_s from SP.60, Eq. (2.2.17)	ν_c=1 s^{-1}	DIA.60
Diffuse interface, adiabatic	ν_s from SP.30, Eq. (2.2.17)	ν_c=1 s^{-1}	DIA.30
Diffuse interface, not adiabatic	ν_s from SP.100, Eq. (2.2.17)	ν_c=1 s^{-1}	DINA.100
Diffuse interface, not adiabatic	ν_s from SP.60, Eq. (2.2.17)	ν_c=1 s^{-1}	DINA.60
Diffuse interface, not adiabatic	ν_s from SP.30, Eq. (2.2.17)	ν_c=1 s^{-1}	DINA.30
Diffuse interface, not adiabatic	ν_s from SP.60, Eq. (2.2.18)	ν_c=1 s^{-1}	DI.60.1
Diffuse interface, not adiabatic	ν_s from SP.60, Eq. (2.2.18)	ν_c=50 s^{-1}	DI.60.50
Diffuse interface, not adiabatic	ν_s from SP.60, Eq. (2.2.18)	ν_c=100 s^{-1}	DI.60.100
Diffuse interface, not adiabatic	ν_s from SP.60, Eq. (2.2.18)	ν_c=150 s^{-1}	DI.60.150
Diffuse interface, not adiabatic	ν_s from SP.60, Eq. (2.2.18)	ν_c=200 s^{-1}	DI.60.200
Diffuse interface, not adiabatic	ν_s from SP.1000, Eq. (2.2.18)	ν_c=100 s^{-1}	DI.1000.100
Diffuse interface, not adiabatic	ν_s from SP.100, Eq. (2.2.18)	ν_c=100 s^{-1}	DI.100.100
Diffuse interface, not adiabatic	ν_s from SP.30, Eq. (2.2.18)	ν_c=100 s^{-1}	DI.30.100
Diffuse interface, not adiabatic	ν_s from SP250.100, Eq. (2.2.18)	ν_c=100 s^{-1}	DI250.100.100
Diffuse interface, not adiabatic	ν_s from SP250.1000, Eq. (2.2.18)	ν_c=100 s^{-1}	DI250.1000.100

2.5 *Model validation*

The experiments used to validate the diffuse interface model was carried out by Dott.ssa M. B. Adali, Molecular Engineering (MolE) laboratory, at Politecnico di Torino. MolE is a research group who investigate various areas of chemical engineering through computational and experimental analysis. The main target of MolE is the development of new technologies for the process industry, in particular for the pharmaceutical manufacturing.

All the experiments that Dott.ssa M. B. Adali conducted were full spray-freeze drying cycles of mannitol solutions. The operative conditions at which these experiments were carried out are reported in Table 2.4.

Table 2.4: Spray-freeze drying operative conditions.

Parameter	**Value**	**Unit**
Vial type	10R	-
Mannitol formulation	5%	-
Bed height	1.5	cm
Initial mass load	2.15	g
Solution flow rate through the nozzle	5	mL/min
Initial load temperature	233.15	K
Drying step overall time	41	h
Shelf temperature up to 36h	283.15	K
Shelf temperature until the end	293.15	K

Note that the drying time reported in Table 2.4 is the overall step time and not the time required to dry the packed-bed, which will be shown to be lower.

2.5.1 Models' parameters evaluation

The parameter which differentiates the simulations carried out with the single particle model is the number X (i.e., the number of pores which can be present in the particle if they would be lined up along the particle diameter direction). In order to evaluate this parameter, SEM images of mannitol frozen granules were observed (Fig. 2.24).

It has been observed that the structure of the pores can vary from granule to granule. Moreover, along the surface of each particle, different pore dimensions can be found. However, the highest and the lowest value of X observed were 100 and 30, respectively. Thus, it has been decided to investigate this interval with three different simulations.

The physical properties of the packed-bed (i.e., tortuosity, porosity, dried bed permeability and pore size within the bed) were obtained by Ing. F. Etiopia (2021) during his work of master thesis.

According to the author, starting from the packing generation thanks to the Yade python tool it was possible to obtain the packing descriptors through computational fluid dynamics simulations carried out to OpenFOAM.

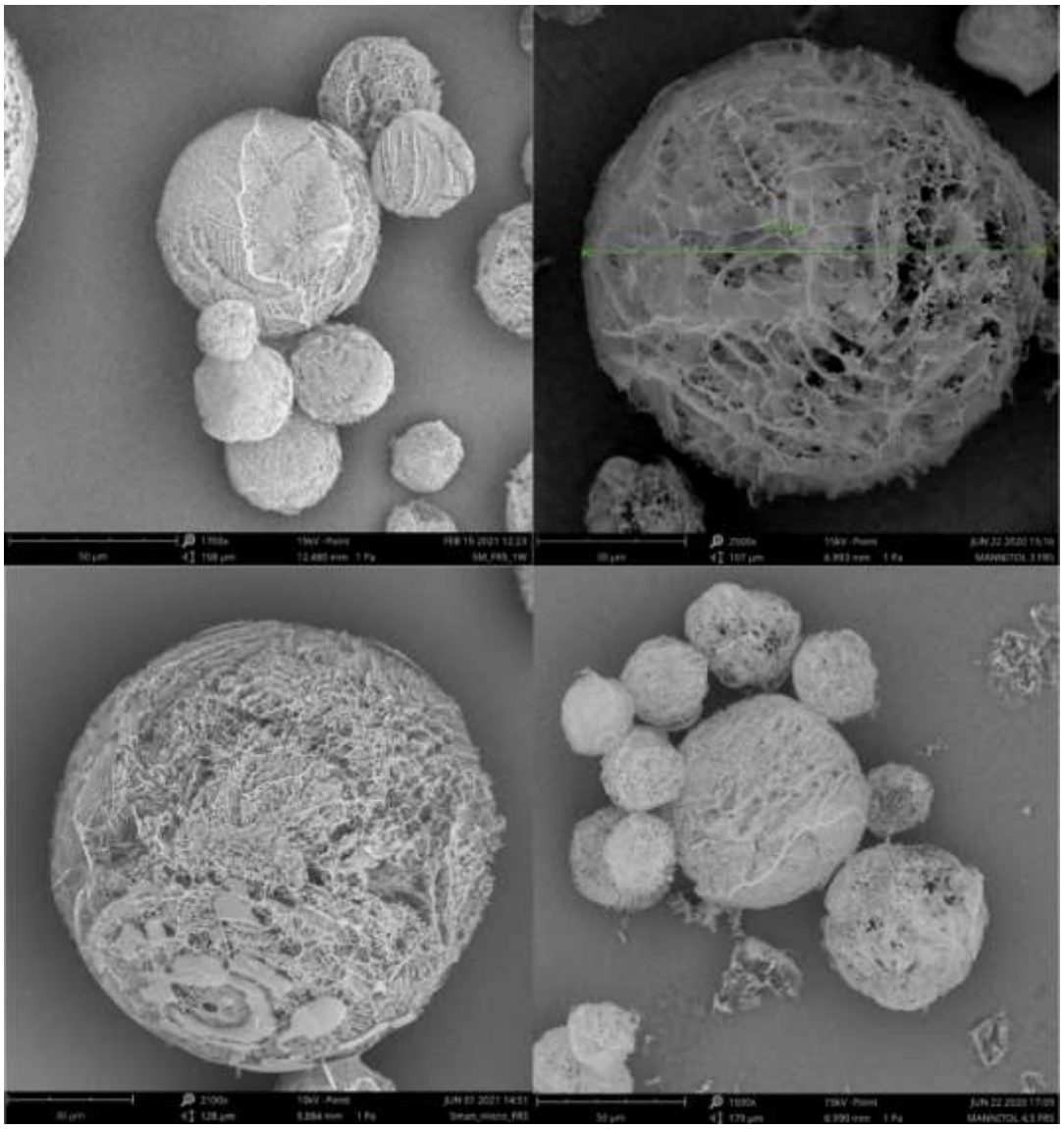

Figure 2.24: Mannitol frozen particles SEM images.

To evaluate the bed permeability, the laminar Navier-Stokes equations were solved with an imposed Reynolds number equal to 0.1. From the solution of these equations, the author obtained the fluid velocity field and the outlet fluid area (A_s). Known the total outlet area (At, square width of the cubic REV), the surface velocity of the fluid has been evaluated (Eq. 2.5.1).

$$U_s = |U|\frac{A_s}{A_t} \tag{2.5.1}$$

Then, from the Darcy's law the author calculated the bed permeability known the pressure drop across the bed and the fluid viscosity.

To evaluate the bed porosity the author described two possible methods. One, evaluating the fraction between the void volume (obtained through a python script) to the REV volume. Second, dividing the packing into 3D pixels thanks to Trimesh and Porespy python tools. This last method provides a numerical matrix in which the void is associated to the number 1, instead the solid space is associated to null. The fraction between the number of values equal to 1 to the total numbers in the matrix correspond to the bed porosity.

This second method was used by the author also for the evaluation of the pore size within the bed. Thanks to Porespy a pore size distribution (Fig. 2.25) was obtained, then a mean pore size value was evaluated knowing the magnitude of a single pixel.

The tortuosity was evaluated by author directly in OpenFOAM simulations. He obtained the magnitude of the velocity field at the outlet of the REV thanks to a software tool. Then, Eq. (2.1.33) was applied.

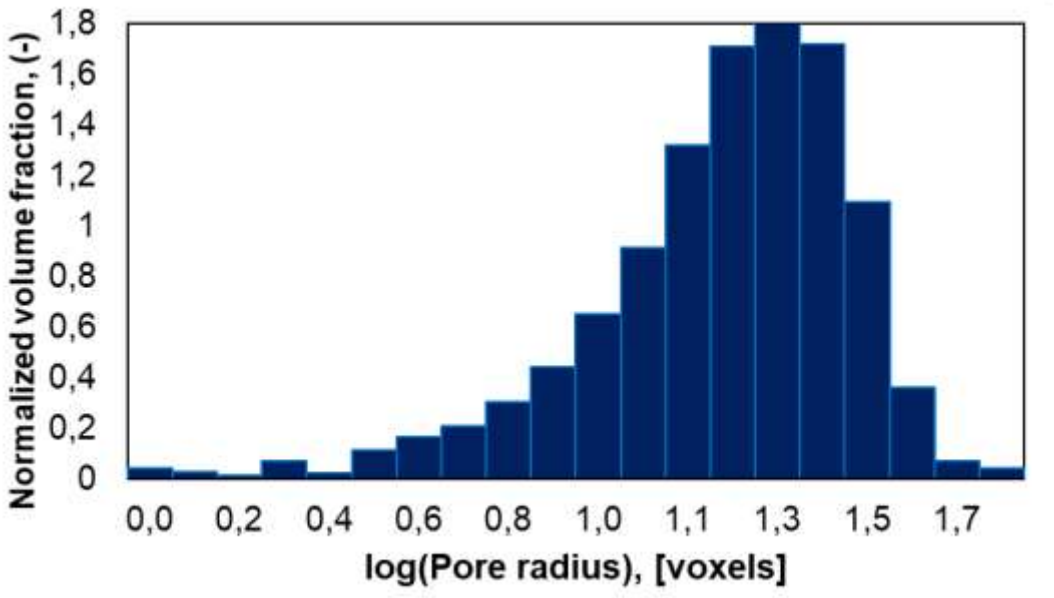

Figure 2.25: Pore size distribution within the REV.

Differential Scanning Calorimetry (DSC) was used to evaluate the mannitol specific heat capacity. The experimental part was conducted by Dott. L. Stratta, who is working in MolE laboratory.

The experiment was set to run at different temperature ramps (*TR*, °C/min) and Eq. (2.4.1) was obtained from the least square errors method.

From DSC it was possible to obtain the temperature profile of mannitol powder in function of the heat provided to the sample. For the same temperature ramp, the experiment was carried out for both heating and cooling cycles.

Knowing the sample mass load, the heat provided, and the temperature ramp it was possible to correlate the specific heat capacity to the temperature profile (Eq. 2.5.2).

$$C_{p_{sol}} = \frac{Q}{m \cdot TR} \tag{2.5.2}$$

In Fig. 2.26 is shown the profile obtained for the mannitol specific heat capacity at different temperature ramps.

It has been observed that at lower temperature ramps (i.e., lower heat provided to the sample) the distance between heating and cooling cycles is larger. This should be accountable for the equipment sensitivity.

Eq. (2.4.1) was obtained minimizing the square distance between heating and cooling cycles at temperature ramp equal to 16 °C/min. Fig. 2.27 shows the specific heat capacity profile obtained with Eq. (2.4.1).

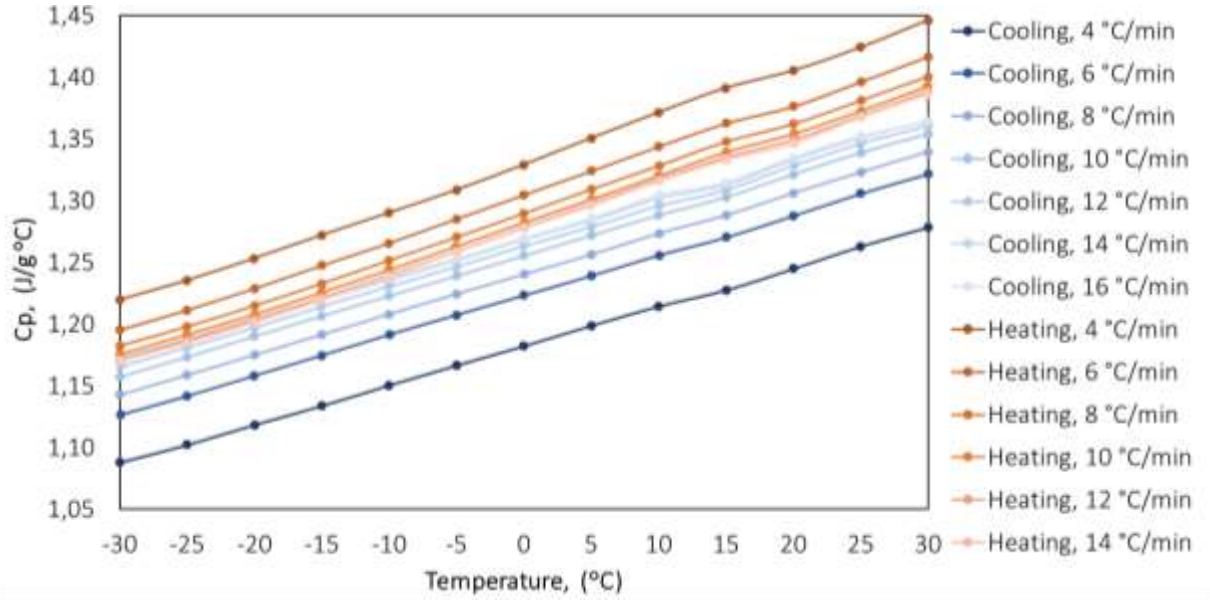

Figure 2.26: Specific heat capacity at different temperature ramps.

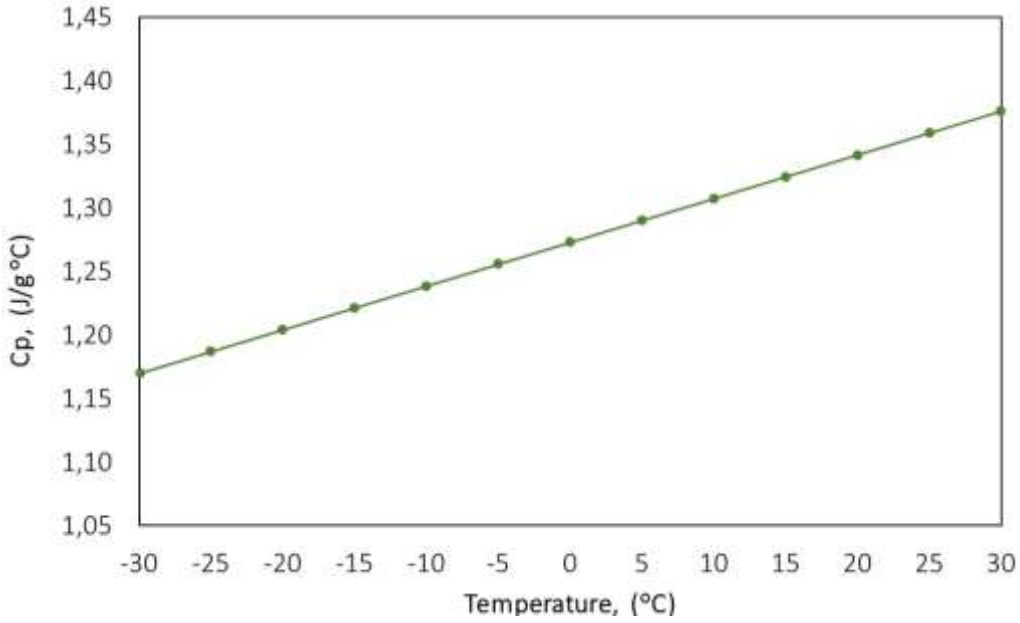

Figure 2.27: Mannitol specific heat capacity from Eq. (2.4.1).

Krok *et al*. (2017) developed a linear model to evaluate the thermal conductivity of pharmaceutical excipients in the range of 20 °C up to 200 °C. According to authors, the linear model (Eq. 2.5.3) correlates the thermal conductivity of compacted excipients with their relative density (i.e., the fraction between bulk density to dried solid density).

$$k = A + B\Phi \tag{2.5.3}$$

Fig. (2.28) shows the results obtained by authors for the mannitol excipient. Starting from these, the value of A and B constants were evaluated to obtain the thermal conductivity profile at different temperatures (Eq. 2.4.2).

Note that the value of thermal conductivity of interest for both single particle and diffuse interface models is the one at relative density equal to 1.

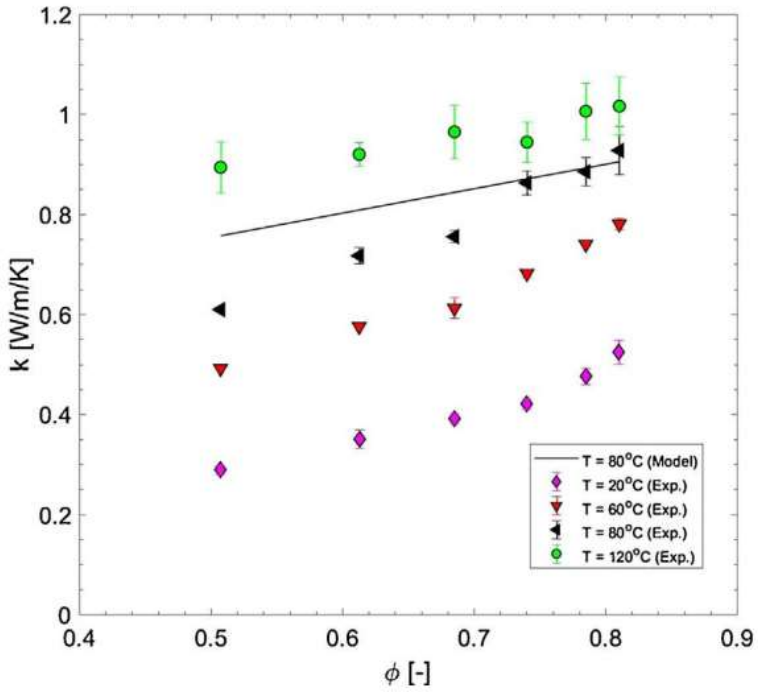

Figure 2.28: Thermal conductivity at various measurement temperatures. Krok *et al*., 2017.

Firstly, the value of *A* and *B* constants at 20 °C, 60 °C, and 80 °C were estimated (Table 2.5), linearly interpolating the results shown in Fig. (2.28).

Table 2.5: A and B values at different temperatures.

Temperature	20 °C	60 °C	80 °C
A	0.65	0.82	0.94
B	-0.04	0.07	0.12

Then, a linear correlation was assumed for the temperature dependence of the *A* and *B* constants (Fig. 2.29).

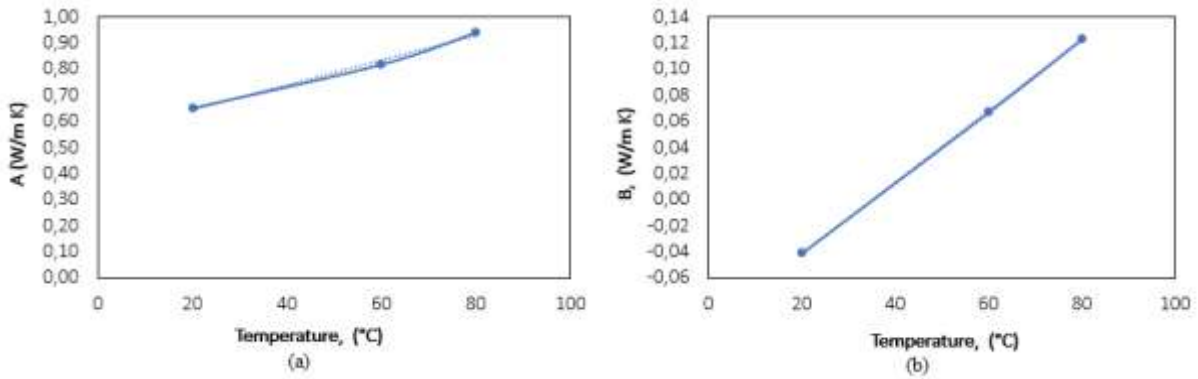

Figure 2.29: A (a) and B (b) profiles at various temperatures.

From the previous assumption it was possible to obtain a mathematical expression for *A* and *B* constants (Eqs. 2.5.4, and 2.5.5).

$$A = 0.0047 \cdot T + 0.5509 \quad (2.5.4)$$

$$B = 0.0027 \cdot T - 0.096 \quad (2.5.5)$$

Lastly, from the sum of Eqs. (2.5.4), and (2.5.5), imposing a relative density value equal to 1, it was obtained Eq. (2.4.2). Note that it was implicitly assumed that Eqs. (2.5.4), and (2.5.5) are still valid at temperature extrapolations lower than 20 °C.

The drying step of all the spray-freeze drying tests were conducted in the MicroFD apparatus (see Sec. 2.5.2 for further detail). To evaluate the value of the overall heat transfer coefficient between the shelf and a vial 10R bottom, it has been necessary to start from a comparison between the values obtained in REVO and MicroFD® technologies. This, because the available measurement of the K_v value was just one obtained in the REVO at vacuum pressure equal to 22 Pa.

Fig. 2.30 shows a comparison between the K_v values obtained at various pressure in REVO and MicroFD for 20R vials. All the experiments were carried out by the MolE group.

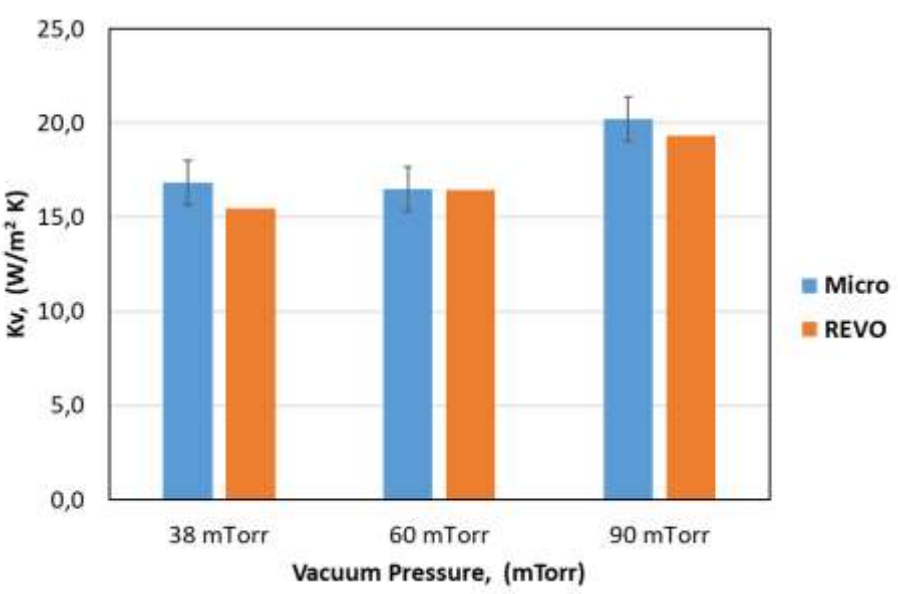

Figure 2.30: Comparison between K_v values in different technologies. 20R vials.

From the comparison, it has been observed that the value difference is in the range of the test variance. Thus, no statistical relevant difference was assumed. Note that in the data from the MolE group, there was no indication of the variance estimated for the REVO experiments.

A full set of data was available for the K_v evaluation in MicroFD with 6R vials (Table 2.6). From the previous assumption it was possible to state that the evaluated heat transfer coefficient has the same value in REVO apparatus.

Table 2.6: Data set in MicroFD for 6R vials.

Pressure, (Pa)	K_v, (W/m^2 K)
8	16.84
12	20.19
26.6	29.37

From the data in Table 2.6, it was possible to obtain a mathematical expression (Eq. 2.5.6) imposing Eq. (B.2.1) and minimizing the square error.

$$K_v = 8.46 + \frac{1.22 p_c}{1 + 0.021 p_c} \tag{2.5.6}$$

The Eq. (2.5.6) evaluate the overall heat transfer coefficient in MicroFD apparatus where 6R vials are drying. These types of vials and the one used by Dott.ssa M. A. Adali (10R, see Table 2.4) have a comparable external diameter (i.e., 22 mm and 24 mm for 6R and 10R vials, respectively). Thus, it has been decided to keep the value of *B* and *C* constants (see Appendix B for further detail) and evaluate the value of *A* constant with the only available measurement for 10R vials in REVO (Table 2.7).

Table 2.7: Data set in REVO for 10R vials.

Pressure, (Pa)	**K_v, (W/m^2 K)**
22	23.5

From the data in Table 2.7, it was possible to obtain an equation for the overall heat transfer coefficient in MicroFD (Eq. 2.4.5) using the same procedure as for Eq. (2.5.6).

2.5.2 Spray-freeze drying tests

The equipment used by Dott.ssa M. A. Adali to carry out the spray-freeze drying tests is the same described in the master thesis work of Ing. C. Lombardo (2021), but using the MicroFD instead of the REVO apparatous.

The atomization phase was conducted in ultrasonic nozzle (Buchi, Switzerland) to guarantee the best controlled particle size distribution (Fig. 2.31). The frequency and the power of the atomizer were set at 60 Hz and 3 W, respectively.

The nozzle was fed with 5 mL/min solution pumped by kdScientific pump (KDS 200 model, KD Scientific, Holliston, MA). The atomization was conducted directly into the vials.

The vials were filled with liquid nitrogen which vapours froze the sprayed solution. The drying step was carried out in MicroFD at vacuum pressure equal to 15 Pa.

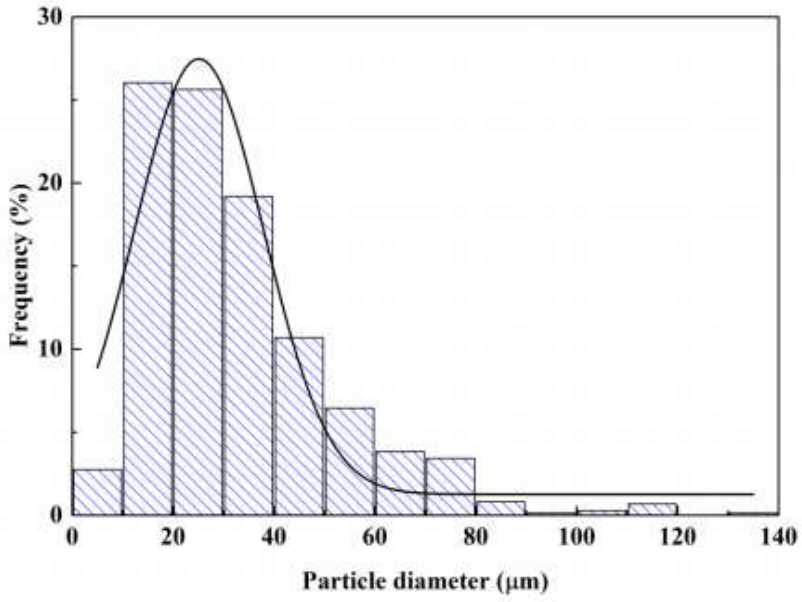

Figure 2.31: Particle size distribution of 5% Mannitol solution.
Reprinted from C. Lombardo (2021), Fig. 16.

2.5.3 Diffuse interface model validation

The parameter used to validate the model was the time needed to dry the packed-bed. This value was evaluated from the tests conducted by Dott.ssa M. A. Adali and then compared to the time obtained from the simulations.

The drying time from experimental data was determined by using a Pirani vacuum gauge. This type of probe was calibrated on a full nitrogen composition in the chamber to incorrect evaluate the chamber pressure during the drying stage. When the drying is ended, the composition in the chamber goes to 100% nitrogen. At this point, the ratio between the pressures measured by Pirani probe and Baratron manometer (i.e., capacitance manometer) should be around unity, thus the drying time is determined. Fig. 2.32 shows the pressure profiles measured by both the pressure gauges.

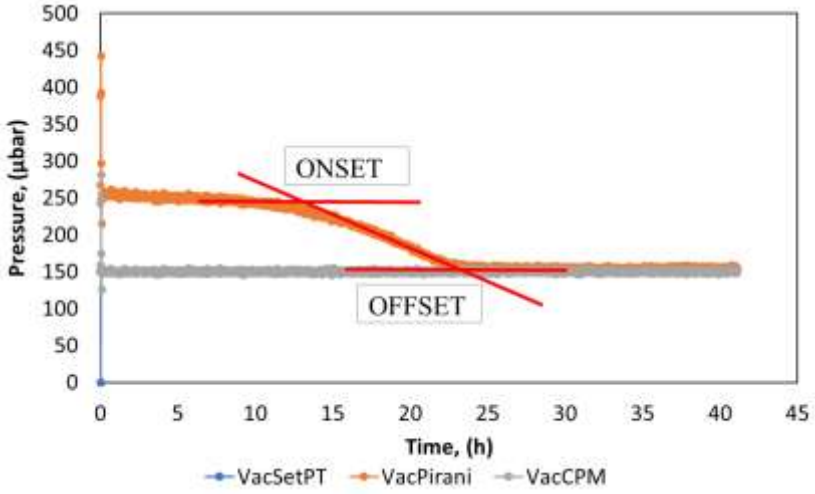

Figure 2.32: Comparison between Pirani and Baratron measurements.

To evaluate the OFF-SET (i.e., the drying time) a straight line interpolating three points taken from the experimental data, was forced to intercept the 150 µbar ordinate value. The three points were chosen in the decreasing trend of the Pirani gauge profile (Tab. 2.8).

Table 2.8: Data set from Pirani gauge measurements.

Pressure, (µbar)	**Time, (h)**
195	18.490
183	19.812
168	21.615

The straight line evaluated (Eq. 2.5.7) and the drying time obtained (Eq. 2.5.8) are presented in the following.

$$y = -8.6212x + 354.18 \tag{2.5.7}$$

$$T_{drying} = 23.68 \text{ (h)} \tag{2.5.8}$$

3 Simulation results

The results obtained from the models' simulations will be presented in the following. First, the single particle model simulations will be reported to show how the granule pore size can affect the mass and heat transport. Then, the results obtained from the diffuse interface model simulations will be shown.

3.1 *Single particle model results*

To accurately describe the drying step of the frozen particles packed-bed and determine the physics regulating the granule lyophilization, a microscale approach has been necessary.

Thanks to the single particle model simulations, it has been possible to obtain the kinetic constant linked to the mass and heat transport during the sublimation phase and understand how operative parameters and physical granule properties can impact on this key variable.

Firstly, the model mesh independency study will be presented. Then, the estimation of the sublimation kinetic constant related to different particle pore sizes will be shown. Lastly, the impact of the chamber pressure on the ν_s, and dependency of the controlling transport mechanism on the pore size will be illustrated.

3.1.1 Single particle model mesh independency

The set up used to carry out the mesh independency was the SP.100. All the mesh predefined settings, excluding the finest one, that COMSOL includes in its software were compared. The finite element minimum and maximum size used in the various configurations are reported in Table 3.1.

Table 3.1: Minimum and maximum finite element size.

Predefined setting	Minimum element size, (mm)	Maximum element size, (mm)
Extra fine	4.87E-5	0.00114
Finer	1.30E-4	0.00179
Fine	3.25E-4	0.0026
Normal	5.85E-4	0.00325
Coarse	9.09E-4	0.00487
Coarser	0.0013	0.00617

To analyse the impact of the mesh quality on the heat transport, the particle surface temperature was monitored. It has been necessary to evaluate a mean temperature value due to the unsteady nature of the phenomena occurring in the particle. The values calculated for each mesh configurations were compared to the one evaluated for the extra fine setting.

The same procedure was adopted to evaluate the impact of the mesh quality on the mass transport. The mass flux across the sublimation front was the variable monitored.

Fig. 3.1 shows the relative error (Eq. 3.1.1) between the mean value calculated with the extra fine mesh and the one calculated with the other settings. The values obtained from all the simulations are reported in Table 3.2.

$$rel\ err = \frac{\left|\overline{x_{ef}} - \bar{x}\right|}{\left|\overline{x_{ef}}\right|} \tag{3.1.1}$$

In Eq. (3.1.1) the $\overline{x_{ef}}$ term represents the mean value of a generic variable evaluated for the simulation with the extra fine mesh setting. Instead, the $\bar{x}$ term represents the mean value of a generic variable calculated for the other settings.

Table 3.2: Temperature and mass flux mean values evaluated.

Predefined setting	Temperature mean value, (K)	Mass flux mean value, (kg/(m^2 s))
Extra fine	242.79	2.99E-05
Finer	242.84	3.05E-05
Fine	242.77	2.95E-05
Normal	242.77	2.95E-05
Coarse	242.64	2.84E-05
Coarser	242.61	2.74E-05

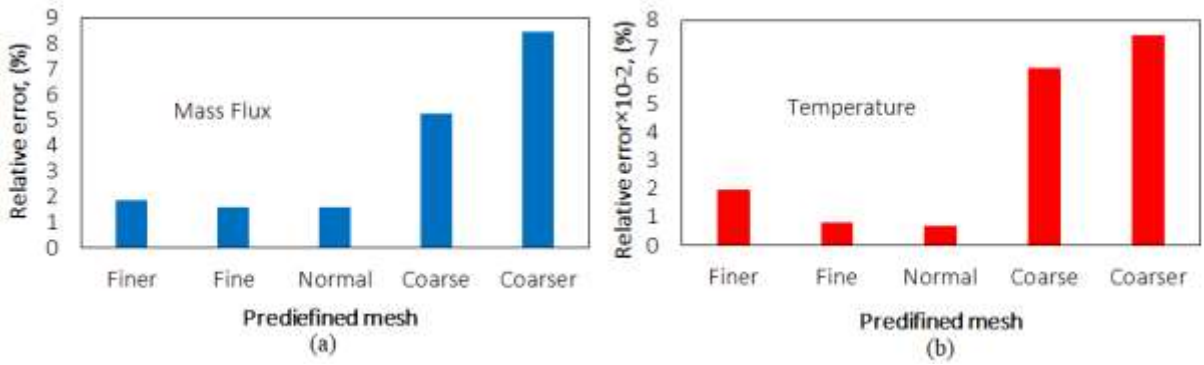

Figure 3.1: Mass flux (a) and Temperature (b) relative error.

The temperature relative error (Fig. 3.1.b) was never higher than 0.1%. From the values reported in Table 3.1, it was observed that the variation affects only the first decimal. Since the difficulty to experimentally evaluate a temperature value with a standard deviation lower than $\pm$ 1°C, it is possible to state that even the coarser quality of the mesh was fitted to accurately simulate the heat transport.

Instead, the mass flux relative error (Fig. 3.1.a) shown higher numbers. The error started to affect the third digit from the normal mesh setting and was constant with higher quality settings. Since a numerical propagation error is unavoidable in all computer simulations, it has been decided that a relative error affecting the third digit give sufficiently accurate results.

To be completely safe with the results obtained from the model, considering also the impact that the kinetic constant evaluated has to the diffuse interface model, the extra fine setting was adopted as default mesh set up (see Sec. 2.4.3). This choice, because the simulation time required to carry out all the simulations with the various mesh settings varied in the range of 7 up to 9 minutes, so the computational effort has not been a limiting parameter.

3.1.2 Sublimation kinetic constant dependencies

A huge step to correctly describe the primary drying of the packed-bed with the diffuse interface model is to accurately evaluate the sublimation kinetic constant.

One of the features provided by SFD is the capability to generate frozen particles with physical properties similar one to each other. Then, a major interest has been focused to understand how these physical properties can impact on the drying step.

In particular, the effect of the size of the granule pores on the sublimation kinetic constant has been investigated. A variation in the pore size affects the mass transfer through the particle according to the Carman-Kozeny expression (Eq. 3.1.2).

$$B_0 = \frac{d_{pore}^2}{180} \frac{\varepsilon_p^3}{\left(1-\varepsilon_p\right)^2} \tag{3.1.2}$$

The values of particle permeability and pore size used for the simulations are reported in Table 3.3.

Table 3.3: Particle permeability and pore size.

Label	Particle permeability, (m^2)	Pore size, (µm)
SP.1000	2.010E-15	0.032
SP.100	2.001E-13	0.325
SP.60	5,583E-13	0.541
SP.30	2,233E-12	1.083
SP.10	2.010E-11	3.248
SP.5	8.039E-11	6.496
SP250.1000	4.763E-13	0.500
SP250.100	4.763E-11	5.000

An increasing pore size provides lower water vapour transport resistance through the granules (i.e., higher particle permeability). Thus, an increasing sublimation kinetic constant will be seen. Fig. 3.2 reports the water vapour velocity profiles across the dried layer for the SP.100, SP.60, and SP.30 simulations.

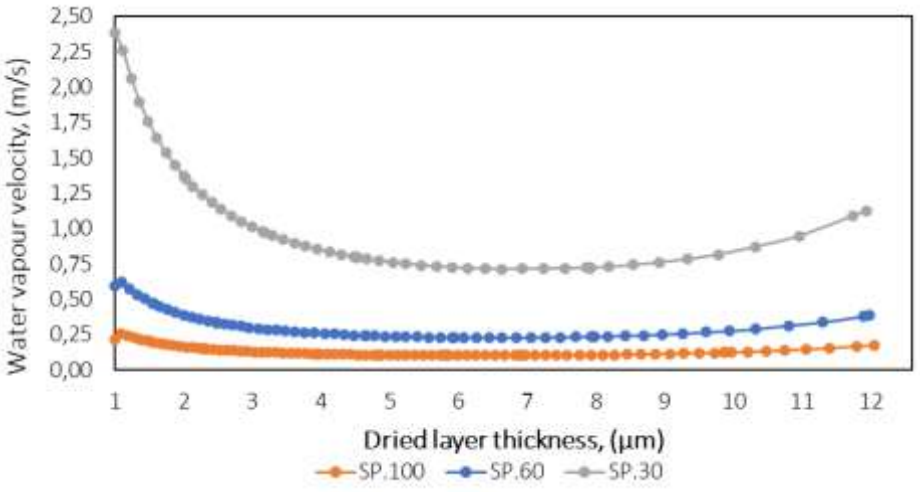

Figure 3.2: Comparison between water vapour velocity in the dried layer for the various simulations.

The values reported in Fig. 3.2 were evaluated according to Eq. (3.1.3).

$$u_w = \frac{N_{w,interf}}{\left(\frac{p_{inter}}{RT_{inter}} - \frac{p_{vac}}{RT_{r=R}}\right) M_w} \tag{3.1.3}$$

The time required to achieve the stop condition varied for each simulation. Hence, to fairly compare the different profiles obtained, in the abscissa the dried layer thickness was set (which

can vary from 0 µm to 16 µm for all the simulations, excluding both SP250.1000, and SP250.100). Note that the imposed stop condition is achieved when the dried layer thickness is around 12 µm.

The first ice layers (i.e., up to 4 µm from the particle surface) encounter less mass transport resistance and the vapour velocity is higher. Then, a stationary condition with a constant fluid velocity is achieved. During that, the increasing water vapour flux (Fig. 3.3) is balanced by an increasing driving force linked to a higher mass transport resistance. Lastly, a rising velocity profile is observed at the end of the drying step thanks to the ice volume reduction which allow less mass transport resistance.

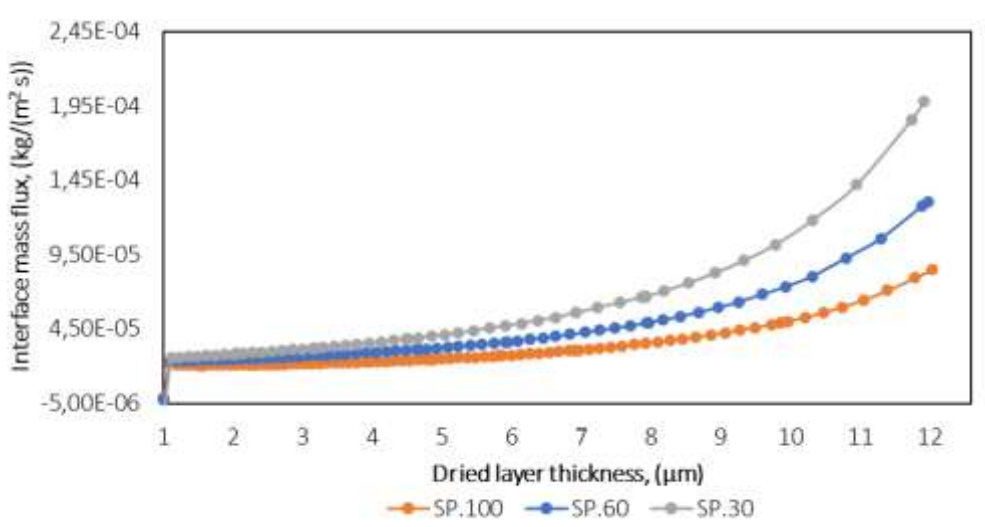

Figure 3.3: Comparison between water vapour flux across the interface for the various simulations.

The highest velocity registered for the SP.30 simulation can be linked with the lowest mass transport resistance provided by the pore size which allow the highest particle permeability, hence the highest interface mass flux. This phenomenon is translated in a narrower concentration gradient across the dried layer resulting in a more homogeneous water vapour distribution.

To provide a sublimation kinetic constant value which is independent of the mass transport resistance, each fluid velocity value obtained from Eq. (3.1.3) were divided by the dried layer thickness, according to Eq. (2.2.17). Fig. 3.4 shows the results.

As shown for the fluid velocity, even the sublimation kinetic constant profiles seem to achieve a stationary condition after the first ice layers were dried.

This behaviour can be feasible only when the granule dimension is lower enough to neglect the additive mass transfer resistance that the generation of the dried layer into the particle is providing. When the granule dimension starts to become higher enough, the change of the physical properties can no longer be neglected, and an asymptotic behaviour of the sublimation kinetic constant becomes wrong.

The values chose to represent the sublimation kinetic constant (Table 3.4) in the DIA.# and DINA.# simulations are the one evaluated when the profiles reach the stationary behaviour.

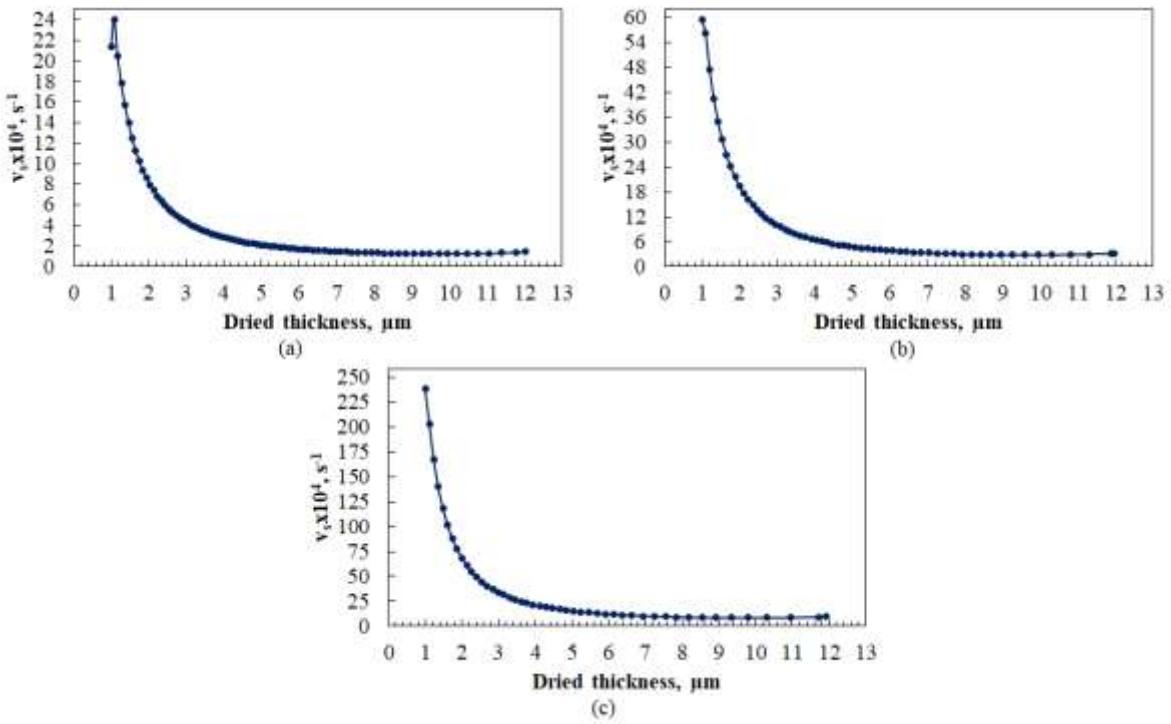

Figure 3.4: (a) SP.100, (b) SP.60, (c) SP.30 sublimation kinetic constant profiles with Eq. (2.2.17).

Table 3.4: Sublimation kinetic constant for diffuse interface model.

Label	Sublimation kinetic constant, (s^{-1})
SP.100	1.00E+4
SP.60	2.75E+4
SP.30	8.30E+4

As said in Chapter 2, to take into account the change in physical properties of the particles over time also after the drying of the first layers of the particles, a second definition of the sublimation kinetic constant (Eq. 2.2.18) was used.

Fig. 3.5 shows the profiles obtained. The entire behaviour was taken to simulate the sublimation kinetic constant profile in the DI.# simulations of the packed-bed.

The behaviour shown in Fig. 3.5 were modified according to Eq. (3.1.4) to be included in the diffuse interface simulations.

$$\nu_s = \begin{cases} 0, & if\ S = 0 \\ \nu_s, & if\ 0 < S \leq 1 \\ \nu_s|_{S=1}, & if\ S > 1 \end{cases} \tag{3.1.4}$$

The conditions imposed in Eq. (3.1.4) mean that the ν_s becomes constant when the ice starts to fill the pores within the packed-bed, and that the kinetic becomes null when the granule is fully dried.

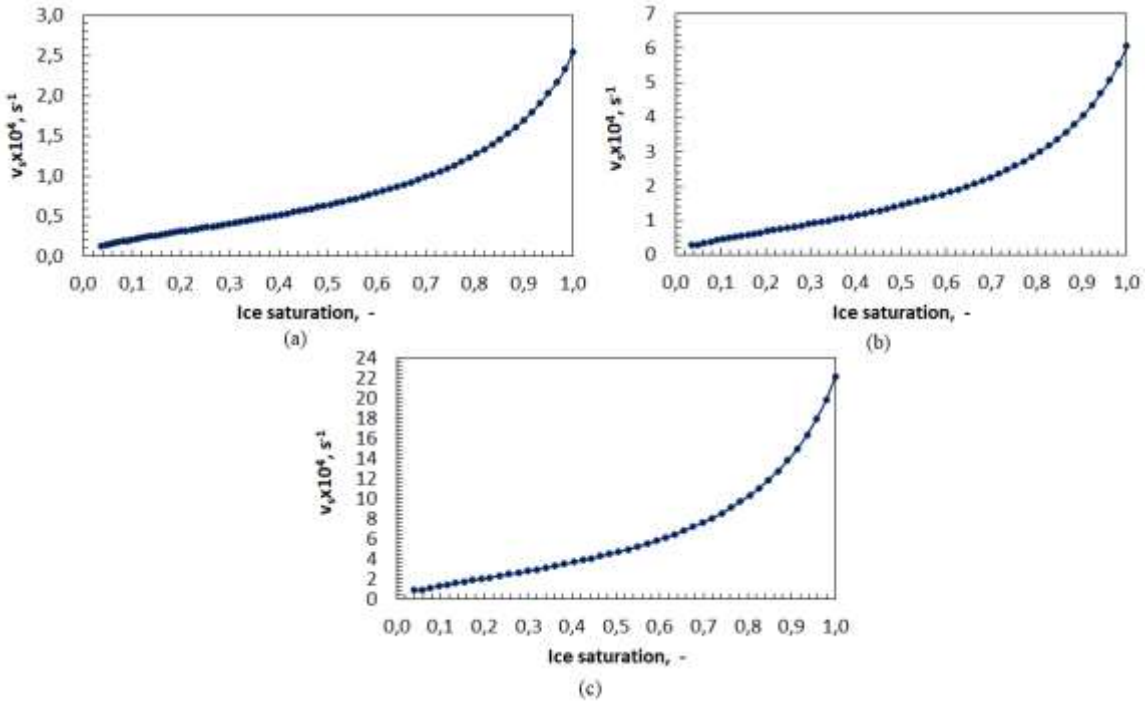

Figure 3.5: (a) SP.100, (b) SP.60, (c) SP.30 sublimation kinetic constant profiles with Eq. (2.2.18).

As will be presented in Sec. 3.2, a study about which resistance (i.e., the particle mass transfer resistance or the bed mass transfer resistance) is controlling the drying was done. The sublimation kinetic constants evaluated with SP250.# settings (Eq. 2.2.18) were used to carry out the simulations with the DI250.# models. Then, the results were confronted with the DI.1000 and DI.100 simulations.

Fig. 3.6 shows the sublimation kinetic constant behaviour used in the diffuse interface model simulations.

The behaviour presented in Fig. 3.6 was agreed with what was claimed before. Increasing the pore size within the particle means to increase the water vapour permeability through the granule, which can be translated in a lower mass transfer resistance and a higher sublimation kinetic constant.

Moreover, Fig. 3.6 shows that increasing the particle size maintaining constant the relative value with the pore size (i.e., the X value) was translated in a higher sublimation kinetic constant.

In Sec. 3.2 it will be shown if this effect is higher enough to maintain the controlling mass transport resistance the one across the bed, or if this aspect will be overcome by the increased pore size within the bed and the higher dried bed permeability, leading to the mass transport resistance across the granules the controlling one.

Note that the pore size dimension for the SP.250.1000 is similar to the one used in the SP.100 simulation (i.e., 0.5 μm and 0.32 μm, respectively). From Fig. 3.6, the difference in the sublimation kinetic constant is about one order of magnitude. This behaviour can be explained taking into account that during the drying, in the SP.250.1000 simulation is generated a dried thickness which is much higher compared to the dried layer in the SP.100 granule. This phenomenon will bring to a higher mass transport resistance for the SP.250.1000.

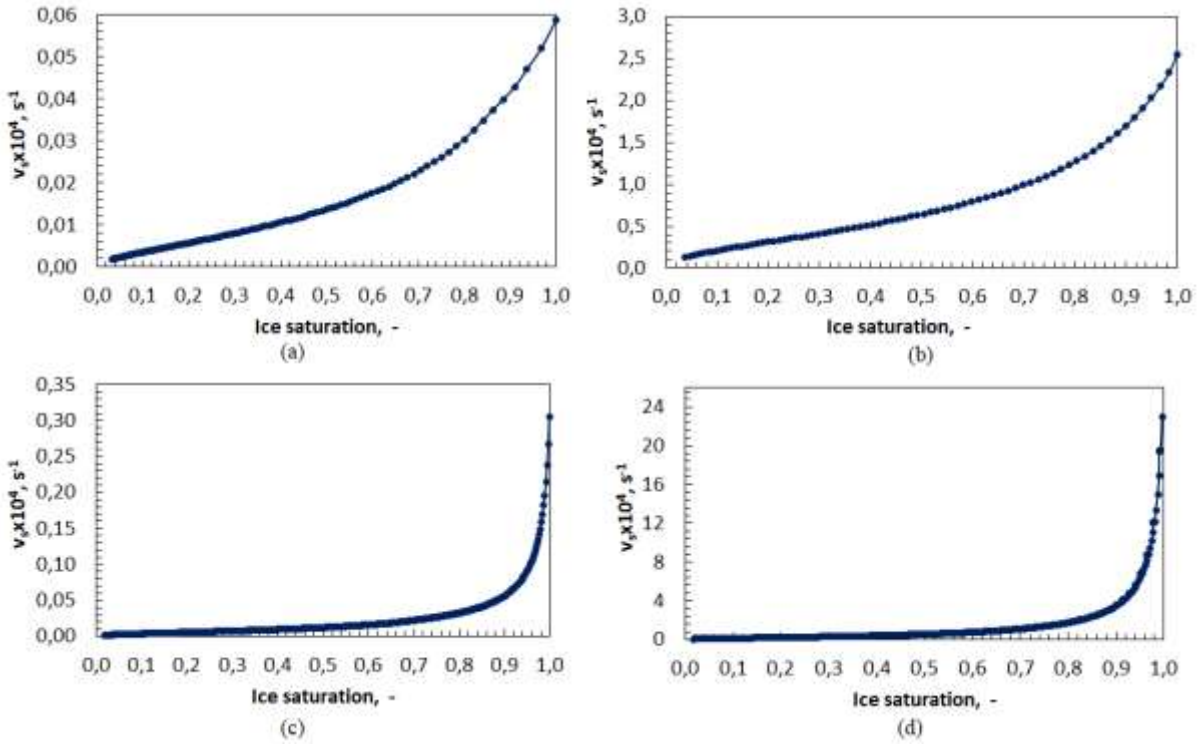

Figure 3.6: (a) SP.1000, (b) SP.100, (c) SP250.1000, (d) SP250.100 sublimation kinetic constant profiles with Eq. (2.2.18).

During simulation, the surface temperature of the particle was also monitored to understand if the controlling transport mechanism would have varied with the various pore sizes (Fig. 3.7).

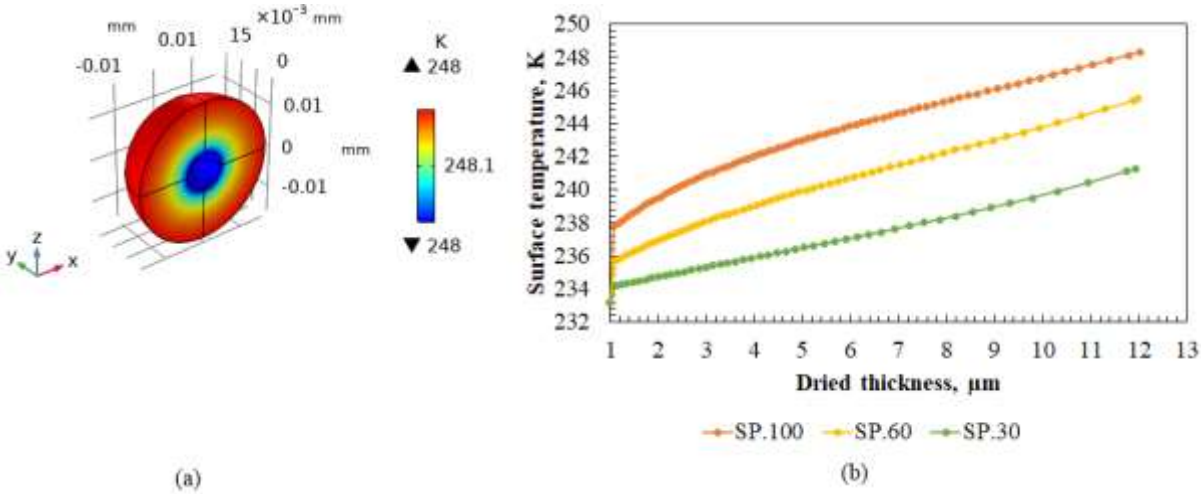

Figure 3.7: (a) SP.100 temperature 3D profile, (b) Surface particle temperature profile.

The surface temperature increases along with particle sublimation (Fig. 3.7b). Moreover, the temperature of the particle in the dried layer is constant along its radius (Fig. 3.7a). The resulting velocity fields lead to heat transport in the dried layer regulated by the conductive mechanism over the convective one.

The marked temperature jump present at the start-up of the drying is due to the strong surface sublimation given by the initial conditions set in the model. This jump decreases according to the increasing specific weigh of the heat transport resistance compared to the mass transport one. Note that the 3D profile shown in Fig. 3.7a belong to SP.100 simulation, but the other setups do not present behaviour variations (see Appendix C for further details).

Since, the frozen layer tends to equilibrate at the same temperature of the heating source, it can be stated that the controlling transport mechanism in the explored simulations is the mass transfer across the particle. Moreover, increasing the pore size seems to mean an increasing importance of the heat transfer over the mass transfer mechanism (i.e., the final temperature reached on the particle surface is lower). Thus, it would be possible to find a sublimation kinetic constant value at which the controlling transport mechanism switches from the mass transfer to the heat transfer.

Lastly, it has been studied how the operative condition, (i.e., the chamber pressure), can impact on the sublimation kinetic constant. Fig. 3.8 shows a comparison between the SP.100 and the SP.100.10 simulations.

Even if a decrement in pressure translate to a higher driving force at the particle surface, also the heat transfer coefficient reduces as well providing a lower amount of heat to the particle (Eq. 2.2.6). Due to the nonlinear variation of the *Kv* (hence, of the heating source), a lower chamber pressure means a slower ice sublimation rate in the first ice layers.

Taking into account the lower heat source provided in the SP.100.10 simulation, the profile shown from the surface temperature during the drying seems reasonable if compared to the one observed for SP.100. A lower exchanged heat flux means that the residual heat to increase the temperature in the dried layer after the ice sublimation is lower. This phenomenon is particularly visible during the first instants of the process. Here, the temperature difference between SP.100 and SP.100.10 is around 2 °C. Then, when the ice volume in the particle is significantly decreased, the surface temperature difference is lower than 1 °C.

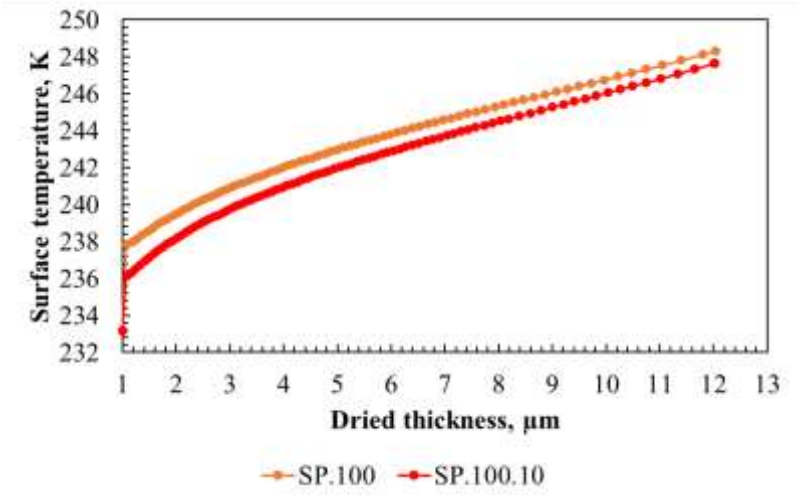

Figure 3.8: Comparison between SP.100 (orange) and SP.100.10 (red) particle surface temperature.

These aspects are reflected on the profile of the sublimation kinetic constant (Fig. 3.9). Firstly, when the fluid velocity across the dried layer is reasonably different due to the higher concentration gradient in SP.100.10, also the kinetic constant shows a marked variation. Then, when the ice fraction within the particle decreases, also the kinetic constant profile shows comparable values. This last aspect is probably given by the lower mass transport resistance present across the particle, which facilitates the evacuation of water vapour from the sublimation front resulting in similar fluid velocity compared to SP.100 (Fig. 3.10).

Note that the sublimation kinetic constant behaviour shown in Fig. 3.9 were evaluated according to Eq. (2.2.18).

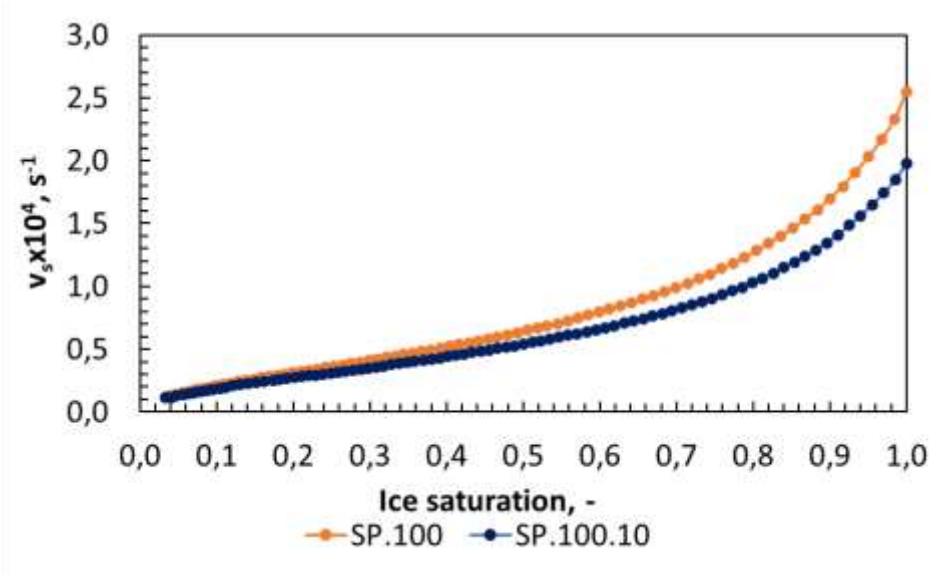

Figure 3.9: Comparison between SP.100 (orange) and SP.100.10 (blue) sublimation kinetic constant.

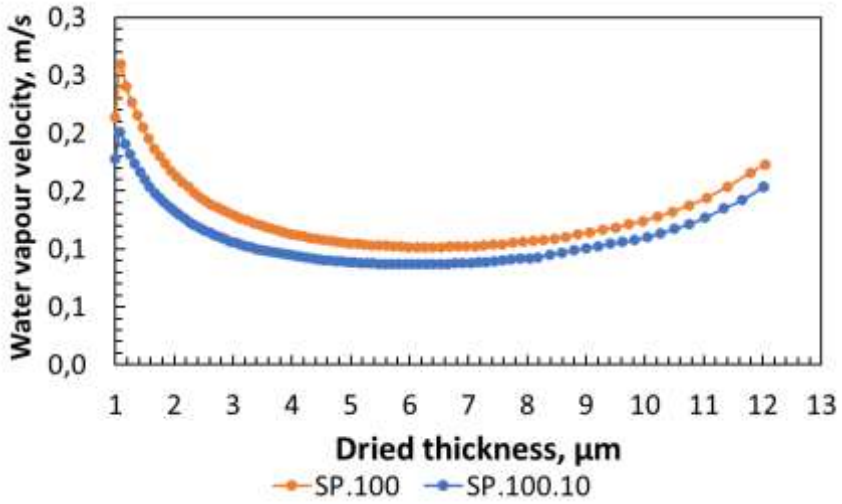

Figure 3.10: Comparison between SP.100 (orange) and SP.100.10 (blue) water vapour velocity.

It can be stated that a lower pressure chamber provides a slower sublimation at the beginning of drying. Then, when more than half of the ice has been sublimated, the difference significantly decreases. As a result, the overall time required to dry a single particle increases when the chamber pressure decreases. Note that the operative conditions compared were quite similar, no information was obtained when the pressure difference was higher than 5 Pa.

3.1.3 Effect of the pore size on the drying controlling mechanism

One of the major interesting aspect obtainable from the single particle model is the possibility to correlate the physical properties of the frozen particle with the transport controlling mechanism through the sublimation kinetic constant.

In the previous section was shown that increasing particle pore size provides a surface temperature profile less steep during drying. Thus, at some pore size a shift from the mass transport as a controlling mechanism to the heat transport should be achieved. Here, the efficiency at which the heat is provided to the particle surface starts to have a huge impact on the granule drying.

To analyse these aspects, a comparison between SP.10 and SP.5 with the previous simulations has been done. Fig. 3.11 presents the particle surface temperature profiles obtained.

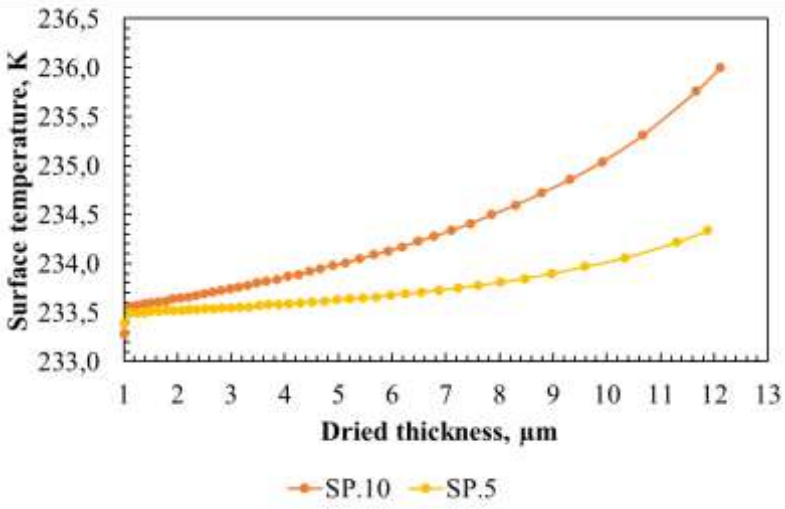

Figure 3.11: SP.10 (orange) and SP.5 (yellow) particle surface temperature profile.

As shown in Fig. 3.11, the temperature at the surface of the particle slowly changes during all the entire granule drying. For SP.5 simulation, the variation from the start to the end of the drying is only 1 °C. Thus, the heat transfer resistance starts to be the controlling resistance among the transport mechanisms. Furthermore, higher sublimation kinetic constants were observed compared to the previous simulations (Fig. 3.12). Bigger pores enhance the particle permeability, allowing higher fluid velocities and a more homogeneous water vapour concentration across the dried layer.

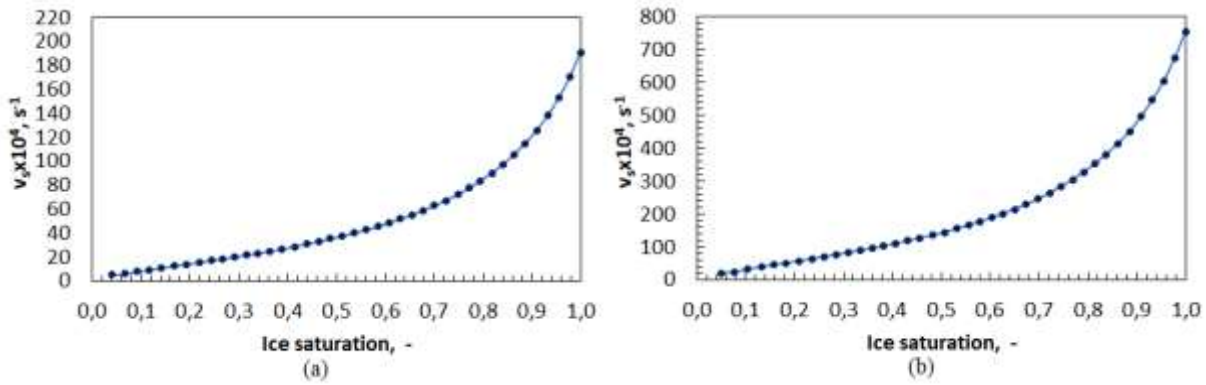

Figure 3.12: (a) SP.10, (b) SP.5 sublimation kinetic constant profile.

Note that the sublimation kinetic constant behaviour shown in Fig. 3.12 were evaluated according to Eq. (2.2.18).

Fig. 3.13 reports the asymptotic values of the sublimation kinetic constant evaluated according to Eq. (2.2.17), excluding the one carried out at different values of chamber pressure.

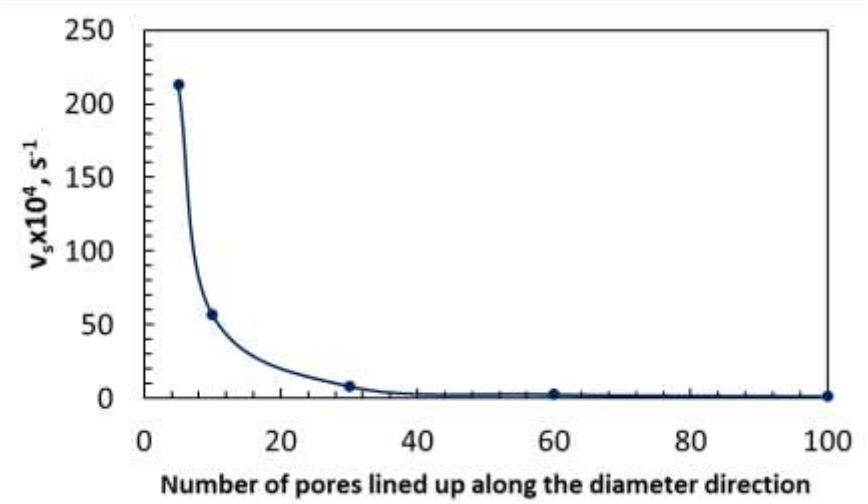

Figure 3.13: Asymptotic value comparison among all the single particle simulations.

As shown in Fig. 3.13, the conditions at which the controlling mechanism is the mass transfer have the sublimation kinetic constant of orders of magnitude lower than the conditions at which the controlling mechanism is the heat transfer.

Thanks to the value of the sublimation kinetic constant, it can be possible to discriminate the various situations. When the asymptotic value of the sublimation kinetic constant is around $10^4\ s^{-1}$ or lower, the mass transfer across the particle is the transport controlling mechanism. Instead, when the kinetic constant has a stationary value of orders of magnitude higher, the heat transfer is the transport controlling mechanism and the efficiency at which the heat is provided to the particle plays a huge role.

3.2 *Diffuse model results*

Once the sublimation kinetic constant value is obtained, the diffuse model simulations can be carried out.

Thanks to the diffuse model it was possible to evaluate the behaviour of mass transfer and heat transfer in the packed-bed during primary drying. It has been studied an equilibrium between sublimation and condensation phenomena varying the kinetic constants' values. Then, the influence of both packing and particle properties on the drying step was evaluated to understand the possible impact of these aspects to the design of a continuous apparatus.

Firstly, it will be presented the model mesh independency study. Then, it will be shown the major differences compared to the results obtained with the moving sublimation front. Moreover, it will be described the differences between adiabatic and not adiabatic simulations and the sublimation-condensation equilibrium. Lastly, it will be shown how the controlling mass transport resistance can vary from the one due to the packed-bed to the one across the particles changing the dimension of the granules and the pore size within them.

3.2.1 Diffuse model mesh independency

The set up used to carry out the mesh independency was the DI.100.100. A custom bed set up of the mesh was used where the finite element minimum size was fixed and the maximum one could vary. The finite element sizes used in the various configurations are reported in Table 3.5.

The values calculated for each mesh configurations were compared to the one evaluated for the DI.100.100.20 setting.

Table 3.5: Minimum and maximum finite element size.

Label	Minimum element size, (mm)	Maximum element size, (mm)
DI.100.100.20	9E-4	0.20
DI.100.100.25	9E-4	0.25
DI.100.100.30	9E-4	0.30
DI.100.100.35	9E-4	0.35
DI.100.100.40	9E-4	0.40
DI.100.100.45	9E-4	0.45

To analyse the impact of the mesh quality on the heat transport, the temperature was monitored at a point 5 mm high from the vial bottom. As was done for the single particle model, it has been necessary to evaluate a mean temperature value due to the unsteady nature of the phenomena.

The same procedure was adopted to evaluate the impact of the mesh quality on the mass transport. The ice saturation at the same previous point was the variable monitored.

Fig. 3.14 shows the relative error between the mean value calculated with the DI.100.100.20 set up and the one calculated with the other settings. The values obtained from all the simulations are reported in Table 3.6.

The relative error was calculated according to Eq. (3.1.1), where the $\overline{x_{ef}}$ term represents the mean value of a generic variable evaluated for the simulation with the DI.100.100.20 setting.

Table 3.6: Temperature and ice saturation mean values evaluated.

Label	Temperature mean value, (K)	Ice saturation mean value, (-)
DI.100.1.20	261,63	0,5642
DI.100.1.25	262,09	0.5649
DI.100.1.30	262,49	0.5742
DI.100.1.35	262,82	0.5675
DI.100.1.40	262,33	0.5980
DI.100.1.45	262,87	0.5906

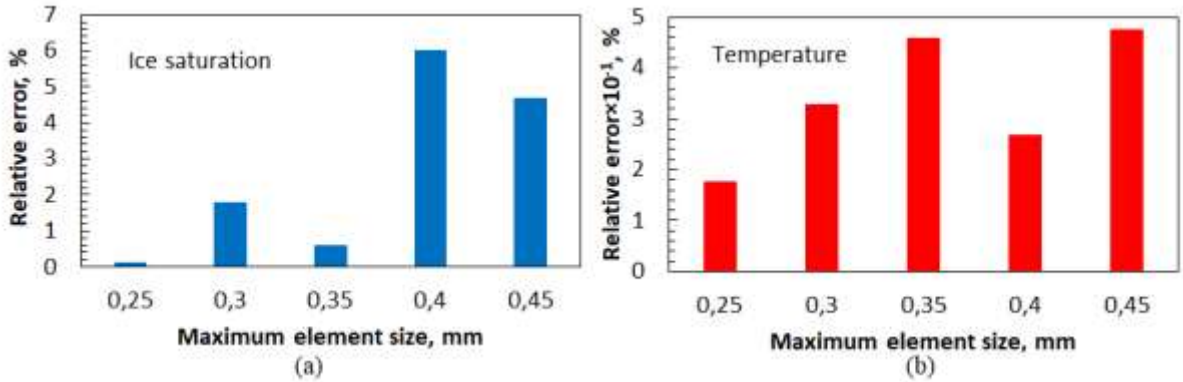

Figure 3.14: (a) Ice saturation and, (b) Temperature relative error.

The temperature relative error (Fig. 3.14b) was never higher than 0.5%. As was obtained for the single particle model, even the biggest maximum element size is fitted to accurately simulate the heat transport.

Instead, for the ice saturation (Fig. 3.14a), the error affected the third digit only for the DI.100.100.25 and DI.100.100.35 simulations. Even for the diffuse model, it has been decided that a relative error affecting the third digit give sufficiently accurate results.

It has to be noted that for both mass and heat transfer, the minimum relative error was obtained for the DI.100.100.25 setting. Moreover, even if a third digit accuracy for mass transfer was achieved in the DI.100.100.35 too, the same cannot be said for the heat transfer where the relative error is one of the highest. Then, the DI.100.100.25 setting was adopted as default mesh set up (see Sec. 2.4.6).

The simulation time required to carry out all the simulations with the various mesh settings varied in the range of 1 up to 4 hours. For the chosen setting, the required time was about 2 hours and half. Although the computational work for the DI.100.100.25 was one of the highest, this setting has been chosen to privilege the accuracy and make a fairly comparison between the model results and the experimental data.

3.2.2 Diffuse interface advantages

The major difference between the diffuse interface model and the moving interface model is the presence of an ice saturation gradient across the dried and the frozen zones of the packed-bed (Fig. 3.15).

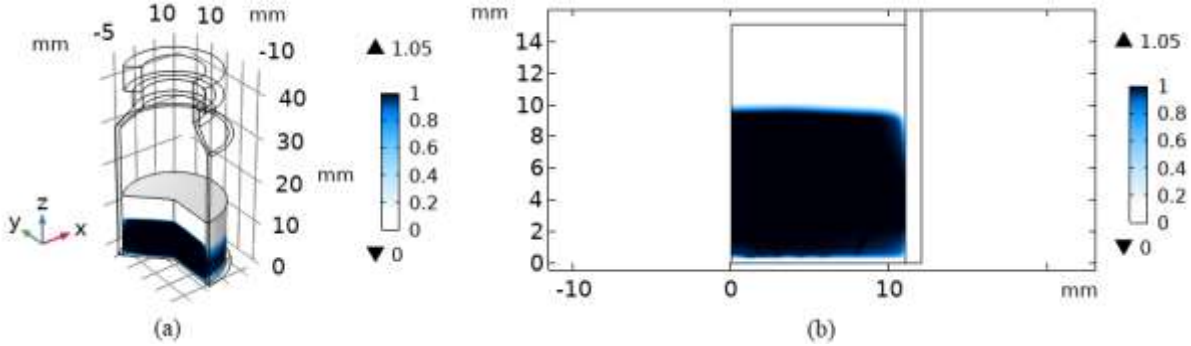

Figure 3.15: (a) 3D view, (b) 2D view of the ice saturation distribution along the packed-bed with the diffuse interface model. Time set at 5 hours of drying. DI.60.100 model used.

As shown in Fig. 3.15, the transition from a frozen zone to a fully dried one is no more sharply (see Sec. 2.1.3). The presence of the gradients derives from the possibility of the water mass flux generated to pass through the interface and leaves the sublimation front. Fig. 3.16 reports the water vapour concentration distribution along the bed.

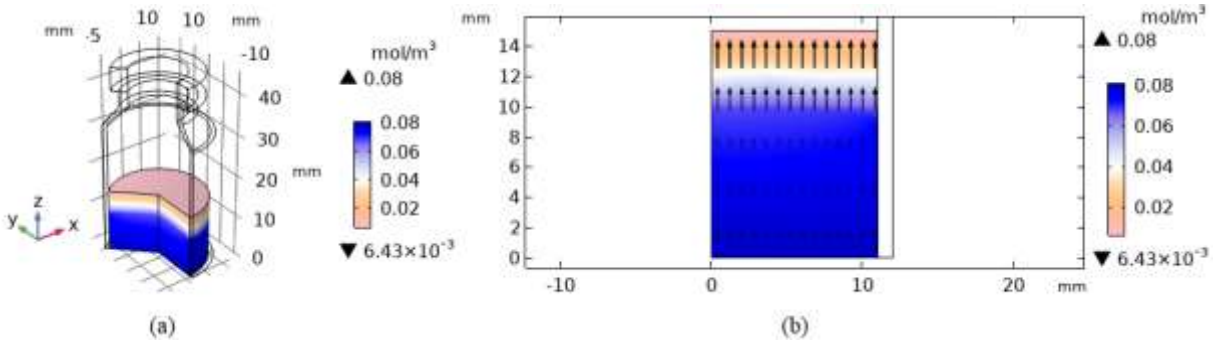

Figure 3.16: (a) 3D view, (b) 2D view of the water vapour distribution along the packed-bed with the diffuse interface model. Time set at 5 hours of drying. DI.60.100 model used.

The black arrows in Fig. 3.16a represent the water mass flux through the bed. The length of the arrows is proportionated to the water flux magnitude. As can be seen from the picture, the higher flux is located right above the diffuse interface between the frozen zone and the fully dried zone. Thus, in contrast with the previous results obtained from Capozzi *et al.* (2019), the presence of a diffuse interface does not involve a no flux condition and the ice saturation changing is no more pre-imposed in the model setting. The drying of the bed is a consequence of the heat exchanged between the shelfs and the vial, increasing the ice vapour tension and promotes the sublimation phenomenon.

As can be seen from the magnitude bar in Fig. 3.15, there are some zones into the bed where the ice starts to fill the void between the particles, decreasing the permeability and increasing the local ice saturation. This behaviour no longer affects a large part of the frozen domain as shown by Capozzi *et al.* (2019b) but involve just some local condensation (Fig. 3.17).

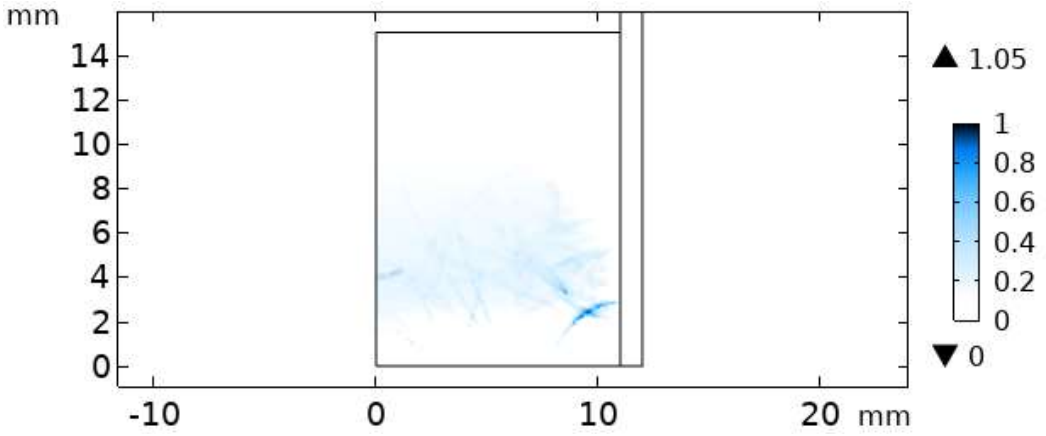

Figure 3.17: Local condensation within the bed pores. Time set at 5 hours of drying. DI.60.100 model used.

Fig. 3.18 reports the mean ice saturation profile during the drying step. In contrast to the one presented in Sec. 2.1.3 (Fig. 2.7) the profile decreases along the drying time. The allowed fluxes through the bed avoid the water accumulation generated by the moving sublimation front. As a result, the mean ice saturation can decrease, and the packed-bed can be dried even if local condensation is allowed.

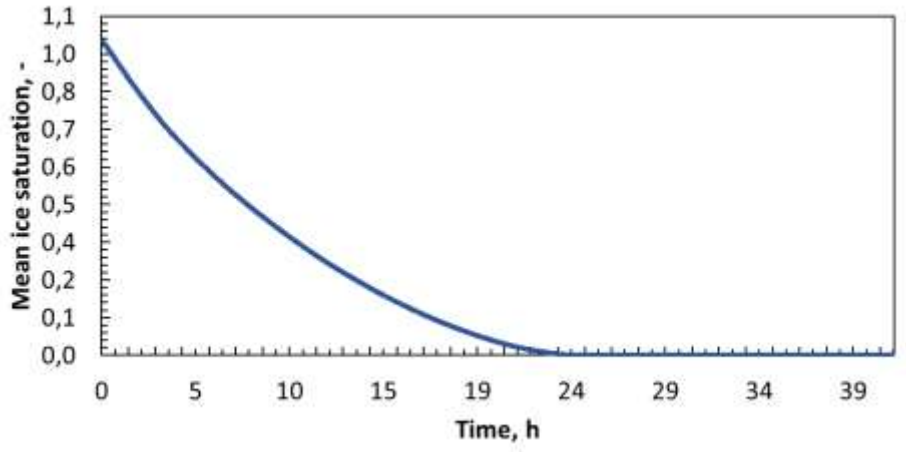

Figure 3.18: Mean ice saturation during the bed drying. DI.60.100 model used.

3.2.3 Influence of sublimation kinetic constant and heat boundary conditions

As anticipated in Chapter 2, two formulations were used (Eqs. 2.2.17, and 2.2.18) to describe the behaviour of the sublimation kinetic constant, more specifically a constant value and a decreasing profile were investigated.

Firstly, it will be presented the results obtained with the simulations carried out with a constant value (i.e., DIA.# and DINA.# models). All the simulations were run using a condensation kinetic constant value equal to 1 $[s^{-1}]$.

Fig. 3.19 shows the mean ice saturation profiles for the carried DIA simulations.

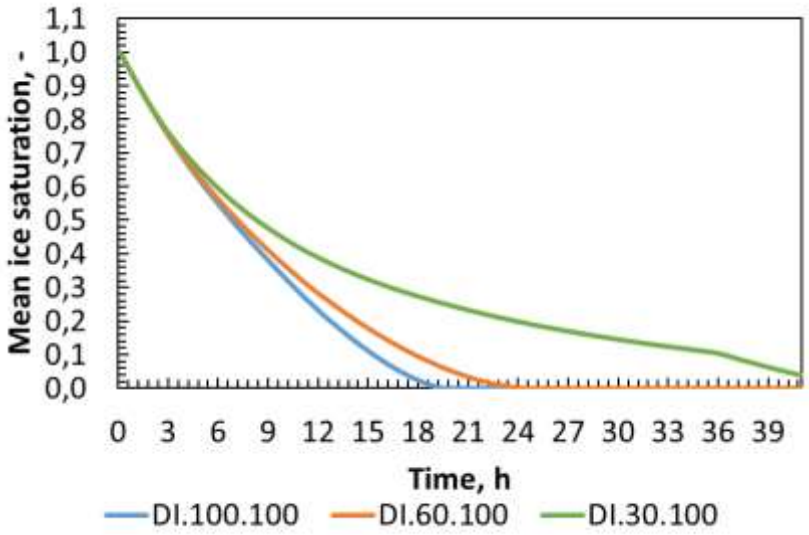

Figure 3.19: Mean ice saturation during the bed drying for DIA simulations.

As said before, the DIA simulations are run with adiabatic conditions at the top bed surface. From Fig. 3.19 it seems that the particles with a pore size from 60 up to 100 times smaller than the granule diameter well describes the results obtained from the experimental data by Dott.ssa M. Adali. Instead, the particles with a pore size 30 times smaller than that the granule diameter led to a bed that did not fully dry in 41 hours.

Fig. 3.20 shows the mean temperature profile of the packed-bed during the drying for the DIA.100 simulation.

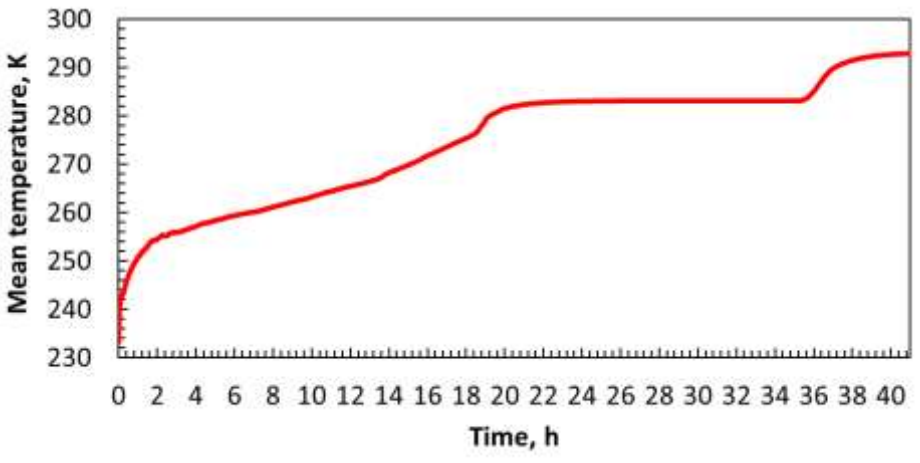

Figure 3.20: Mean temperature of the bed during the drying. DIA.100 simulation.

As can be seen in Fig. 3.20, as soon as the bed is fully dried, the mean temperature reached the shelf temperature and followed its profile (Fig. 2.17) for the rest of the operational time.

To understand if this behaviour is shown also locally in the bed, three different points were monitored to see the evolution of the temperature, and of the ice saturation at 12 mm, 8 mm, and 4 mm from the vial bottom. The radial coordinate was always set in the centre of the bed.

Fig. 3.21 presents the ice saturation profiles for the three different points.

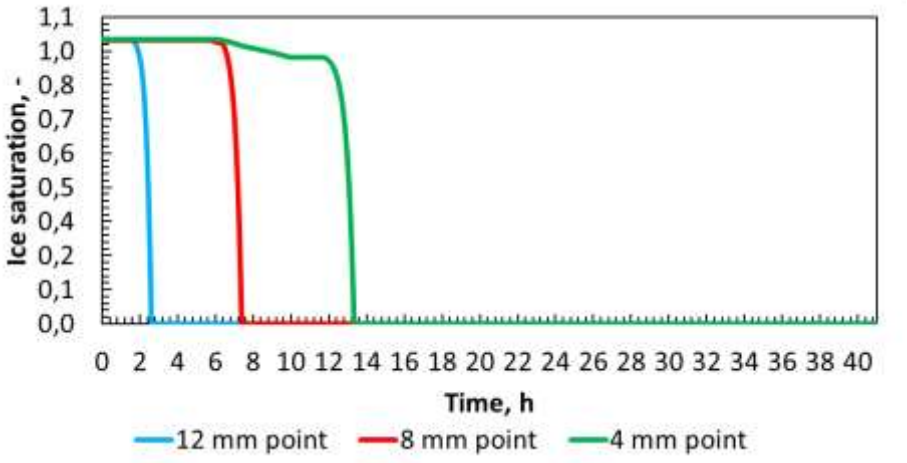

Figure 3.21: Ice saturation profiles for three different points into the bed. DIA.100 simulation.

Fig. 3.22 shows the temperature profiles for the three different points.

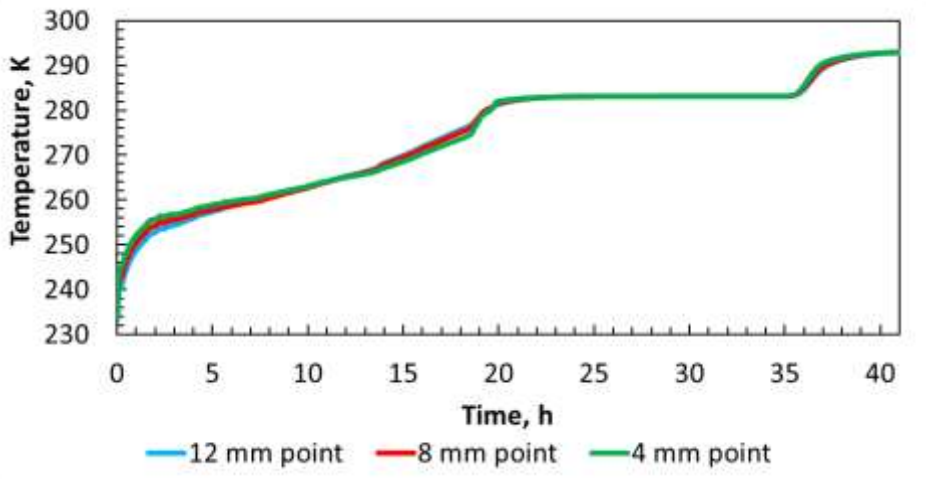

Figure 3.22: Temperature profiles for three different points into the bed. DIA.100 simulation.

Even if the upper points dry before, the temperature tends to remain lower compared to the one of the points below. When the three temperature profiles override each other, the difference is too small to claim that it is not due to numerical error. Overall, the local temperatures reach the shelf temperature as the mean temperature of the bed.

Normally, it would be expected to see the temperature of the dried point overcomes the temperature of the frozen point. The behaviour shown in Fig. 3.22 can be linked to the heating source which is provided only at the bottom of the vial, while the drying starts from the top of the bed due to the adiabatic conditions.

To understand the behaviour presented by the local temperature profiles, Fig. 3.23 shows the temperature and the ice saturation distribution of the packed-bed after 5 hours of drying.

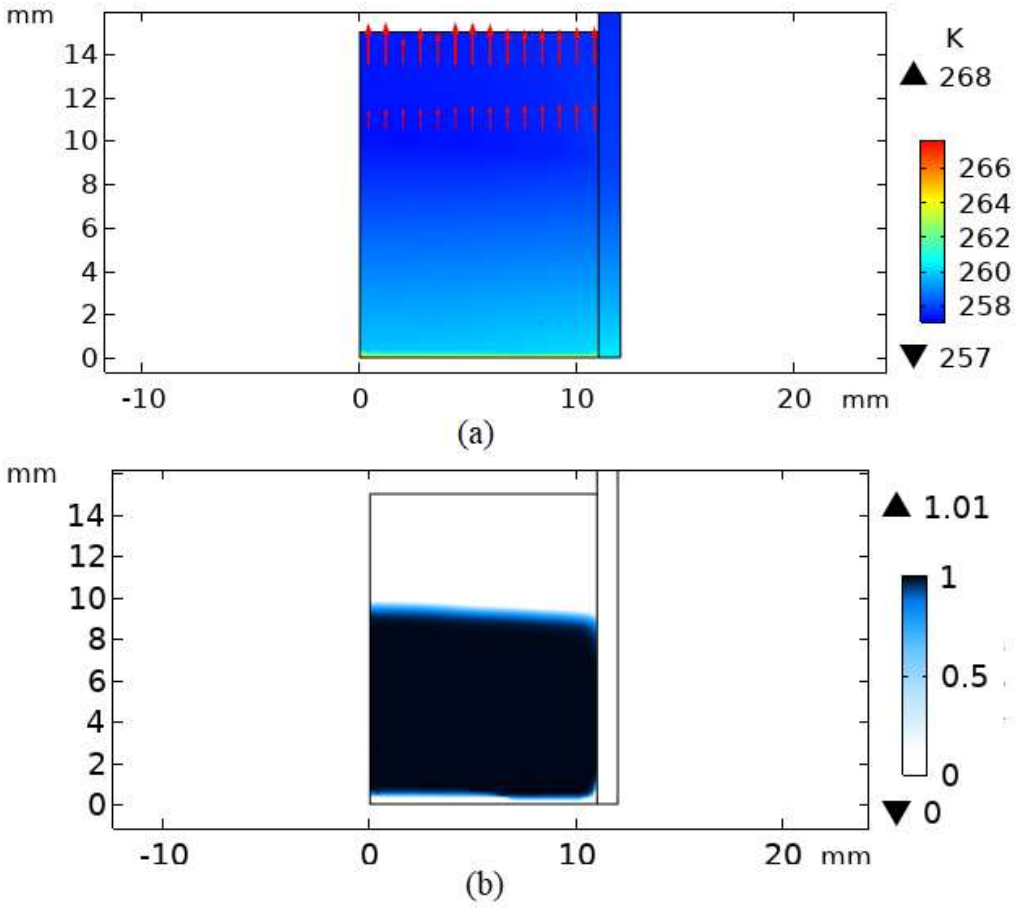

Figure 3.23: (a) Temperature, (b) Ice saturation distribution of the packed-bed after 5 hours. DIA.100 simulation.

From Fig. 3.23a it can be seen as the adiabatic conditions lead to a temperature which is quite homogeneous along the packed-bed. Only the bottom layer, which is in direct contact with the shelf seems to achieve higher temperatures compared to the rest of the particles.

The temperature slightly rises from the dried to the frozen zone and the highest heat fluxes are located the top surface of the bed as shown from the red arrows in Fig. 3.23a. Due to the adiabatic conditions, the heat fluxes coming from the below frozen zone cannot overcome the top bed surface and a heat accumulation is generated. As a result, Fig. 3.23b presents a double front of sublimation.

This phenomenon provides the energy necessary to dry the frozen particles starting from the top of the bed, and overall leads to an increased drying velocity. This behaviour will be particularly evident if compared to the DINA.# simulations.

From Fig. 3.22 is also evident that the transport controlling mechanism during the drying is the heat transfer. The particles can lyophilize before the shelf temperature is reached, and the same is done by the packed-bed.

From the profiles shown in Fig. 3.21 it can be claimed that the mass transport controlling resistance for the DIA.100 simulation is the bed one over the resistance across the particle. A fast decrease of the ice saturation profile is linked to a condition in which it is more difficult to

evacuate the mass fluxes through the bed compared to a water vapour diffusion across the granule.

The same results presented above were obtained for the DIA.60, and DIA.30 simulations.

Fig. 3.25 shows the mean ice saturation profiles for the carried DINA simulations.

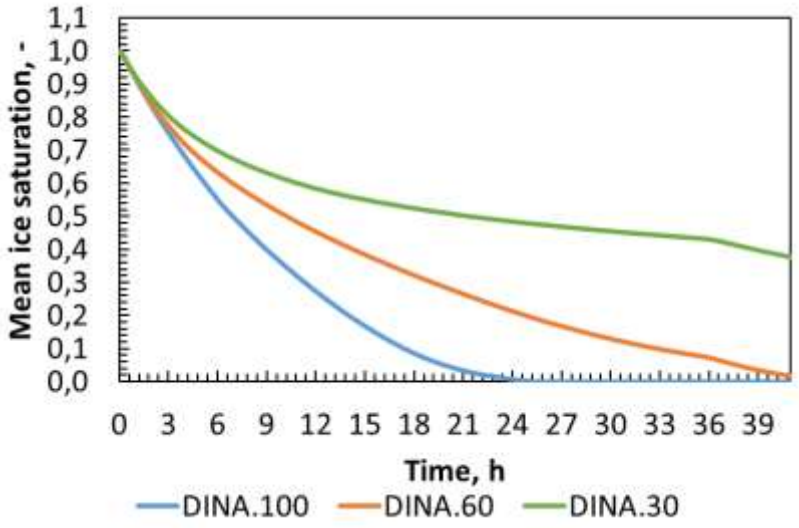

Figure 3.25: Mean ice saturation during the bed drying for DINA simulations.

Compared to the DIA simulations, the DINA profiles presented in Fig. 3.25 are slower. As said before, the adiabatic condition run in DIA settings led to an increased drying velocity due to heat accumulation at the top surface of the bed. In DINA settings, the surface of the packed-bed is heated by the vial cap and the heat fluxes can overcome the top of the bed leaving the packing. Note that, as said in Sec. 2.4.4, the value of the overall heat transfer coefficient was reduced in the DINA simulations to provide the same amount of heat in both DINA and DIA settings.

Fig. 3.26 shows a heat map and the ice saturation distribution of the packed-bed after 5 hours of drying, obtained with the DINA.100 setting.

Compared to Fig. 3.23a, with not adiabatic boundary conditions the heat distribution in Fig. 3.26a is no longer homogeneous. Instead, the radiative fluxes generated by the vial cap help the drying of the bed providing the heat necessary to lyophilize the granules and increase the local temperatures.

However, the disappearance of the heat accumulation overall decreases the drying velocity. If the ice distribution in Fig. 3.23b is compared to the one in Fig. 3.26b, point at 10 mm height is almost dried in the first case and almost fully frozen in the second one. The double sublimation front is still present also in Fig. 3.26b.

As a result, the temperature and ice saturation local profiles obtained are the one shown in Figs. 3.27, and 3.28. With not adiabatic boundary conditions, the temperature profiles of the upper points are able to overcome the one of the points below. Also, note that the ice saturation at 4 mm point is lower compared to the one at 8 mm point until this last part starts to dry. As a consequence, until about 9 hours the temperature profile of the 4 mm point shows higher values compared to the one at 8 mm height from the vial bottom.

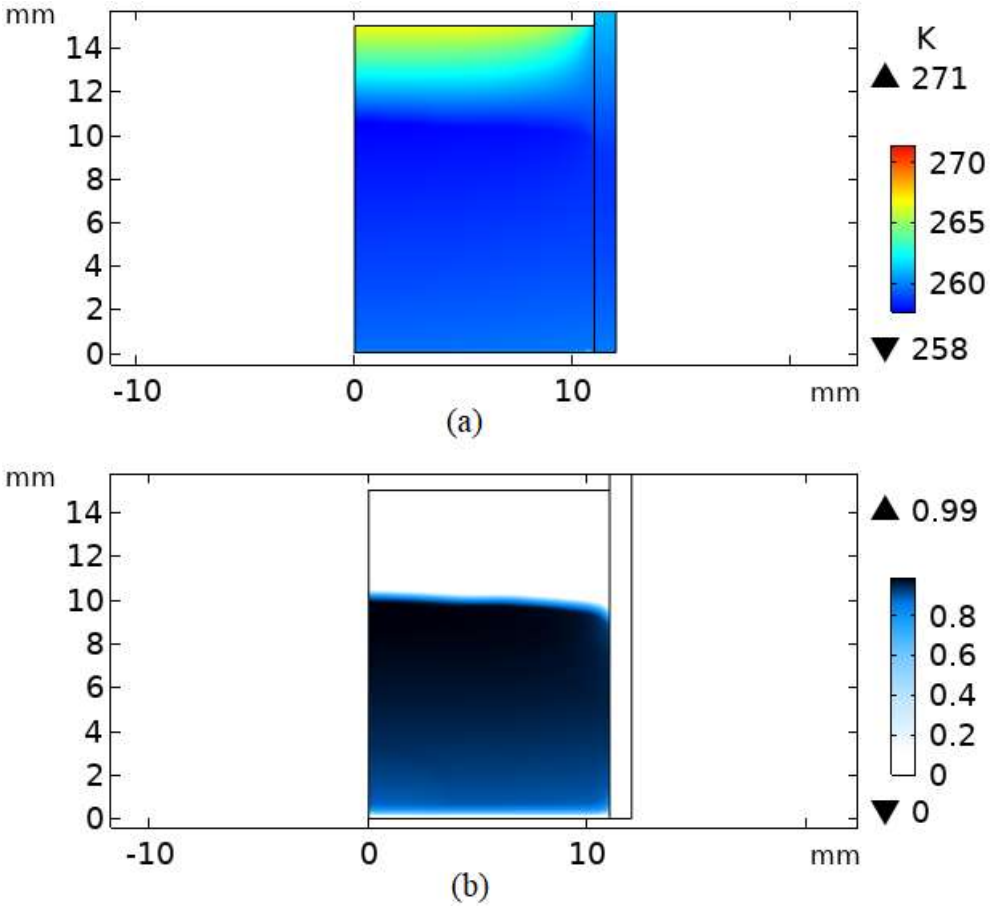

Figure 3.26: (a) Heat map, (b) Ice saturation distribution of the packed-bed after 5 hours. DINA.100 simulation.

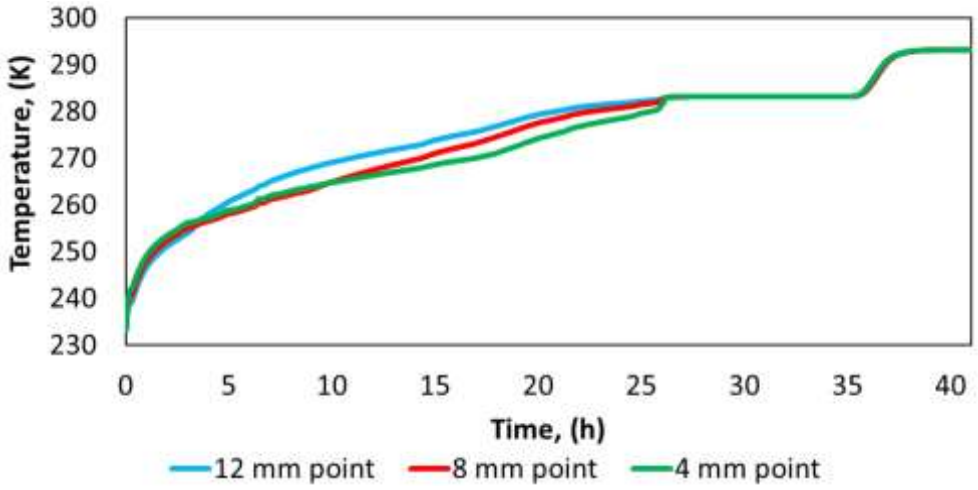

Figure 3.27: Temperature profiles for three different points into the bed. DINA.100 simulation.

Even with not adiabatic boundary conditions, the controlling transport mechanism remains the heat transfer and the mass transport resistance through the bed is higher compared to the one across the particle.

The same results were obtained were obtained for the DINA.60, and DINA.30 simulations.

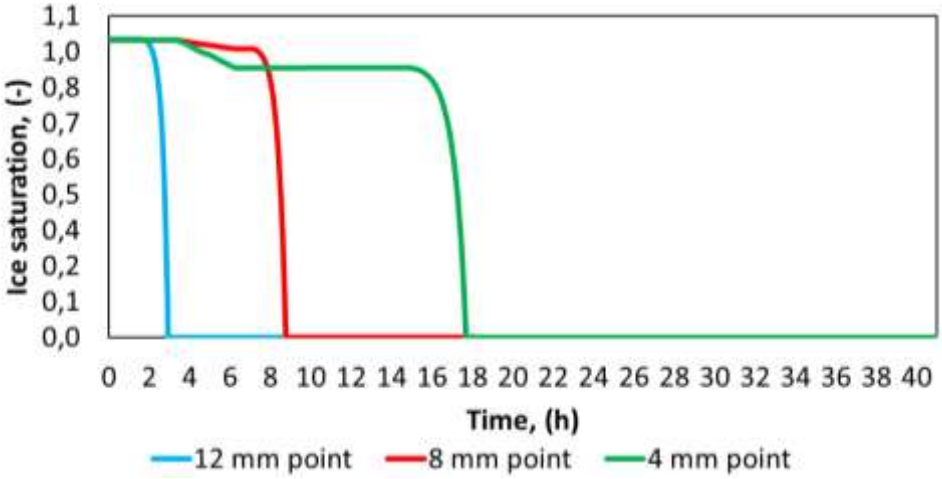

Figure 3.28: Ice saturation profiles for three different points into the bed. DINA.100 simulation.

3.2.4 Ice saturation dependence and sublimation-condensation equilibrium

In this section, it will be presented the results obtained with the simulations carried out with the time dependent sublimation kinetic (Eq. 2.2.18). As said in Chapter 2, the necessity of a time dependent kinetic came out because the sublimation dynamic of a fully frozen particle cannot be the same of a partially or fully dried granule due to the physical properties change.

Fig. 3.29 presents the mean ice saturation profiles for the DI.100.100, DI.60.100, and DI.30.100 simulations. Note that the not adiabatic boundary conditions are still present even in these settings.

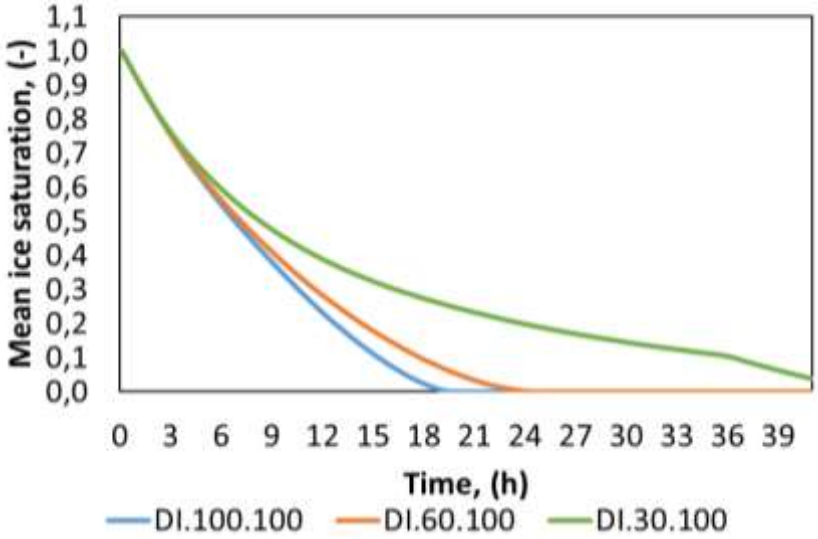

Figure 3.29: Mean ice saturation during the bed drying for DI.100.100, DI.60.100, and DI.30.100 simulations.

First, the simulation which seems to best describe the experimental results was the DI.60.100. The ice saturation profiles obtained shown higher drying velocities compared to those obtained with the DINA configurations.

Even if the overall amount of heat supplied to the bed is the same, the sublimation kinetic in DI configurations is no longer constant with the local ice saturation. This aspect leads to lower heat necessary to lyophilize a partially dried granule compared to the heat needed to dry a fully frozen particle (Eqs. 2.3.8, and 2.3.19). As a result, even if the amount of water molecules which

can locally sublimate for unit of time is higher for DINA settings when the granule is partially dried, the amount of heat required to carry out the lyophilization slows the process if compared to DI simulations.

Fig. 3.30 shows the ice saturation distribution evolution coupled with the heat map for the DI.60.100 simulation.

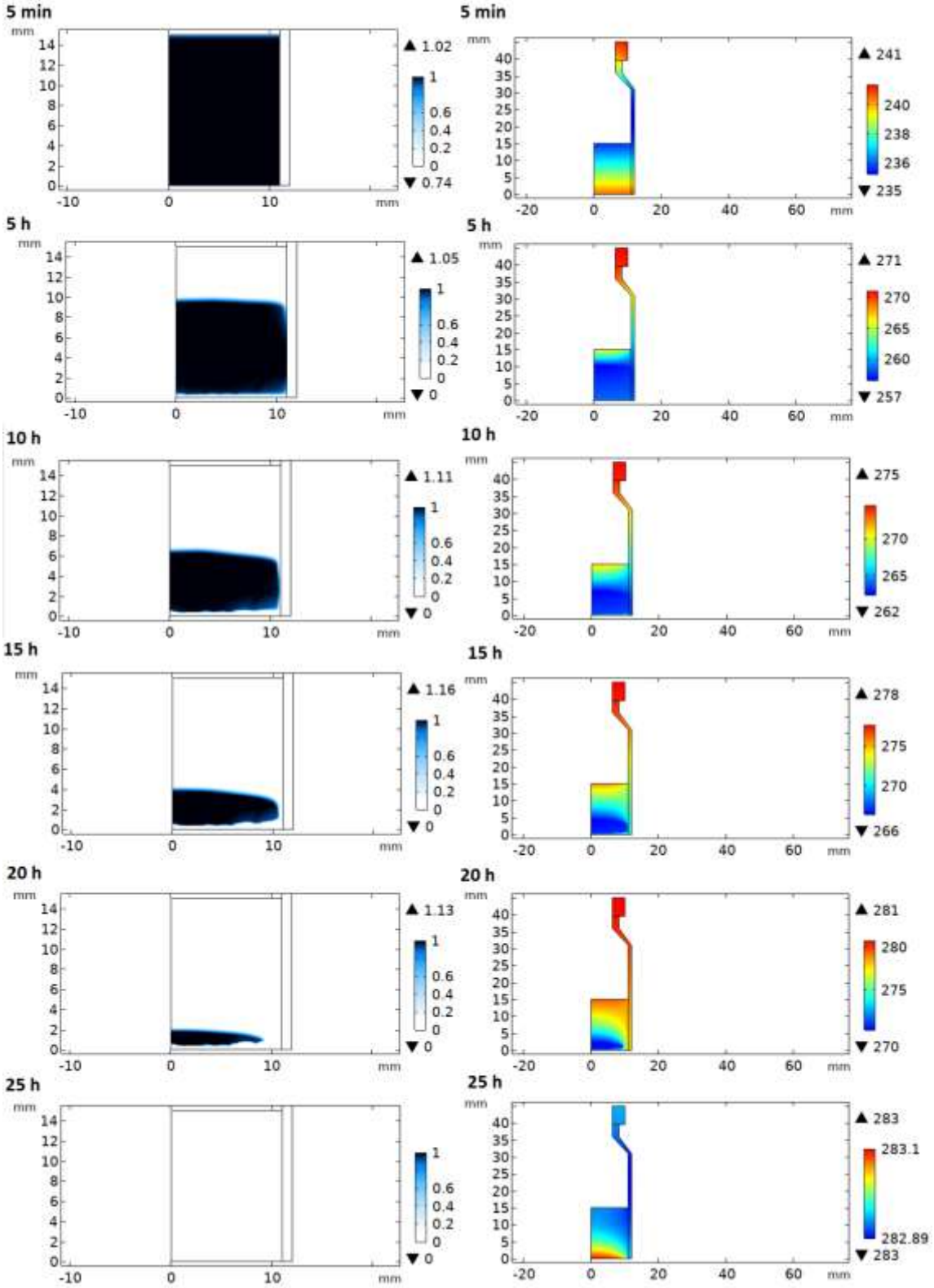

Figure 3.30: Ice saturation distribution and heat map of the packed during time. DI.60.100 simulation.

As can be seen from Fig. 3.30, a third sublimation front is generated thanks to the heat provided by the glass thickness of the vial. The packed-bed tends to lyophilize towards the core, following the heat distribution generated by the heat sources and by the heat conduction in the glass.

This behaviour can also explain the quicker drying obtained for the DI.60.1 simulation compared to the ice saturation profile obtained for the DIA.60 setting (Fig. 3.31).

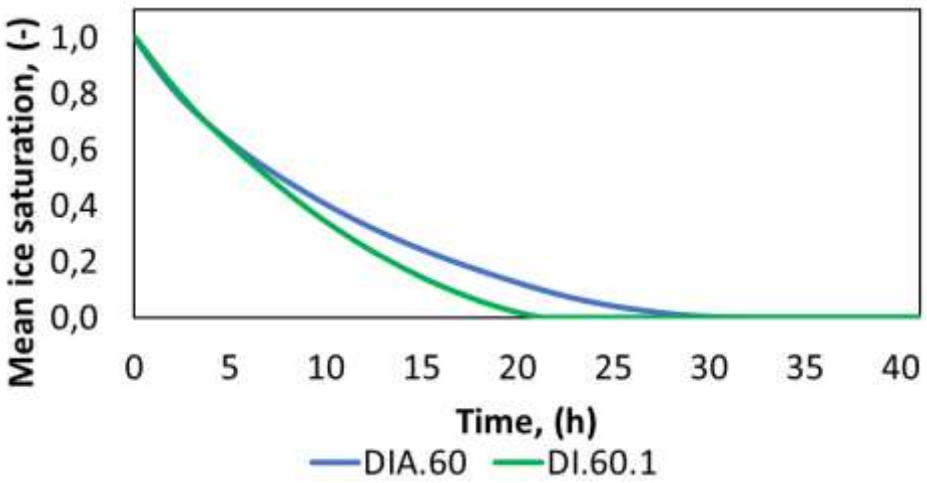

Figure 3.31: (blue) DIA.60, (green) DI.60.1 mean ice saturation during the drying of the bed.

The generation of a third sublimation front is caused by a huge heat flux coming from the glass walls of the vial. This aspect was not present in the DIA simulations due to the heat source and boundary conditions chosen. As a result, the radial fluxes due to the conduction between the packed-bed and the glass accentuate the temperature gradients across the bed (Fig. 3.32), providing an easier mass generation and an increased drying velocity.

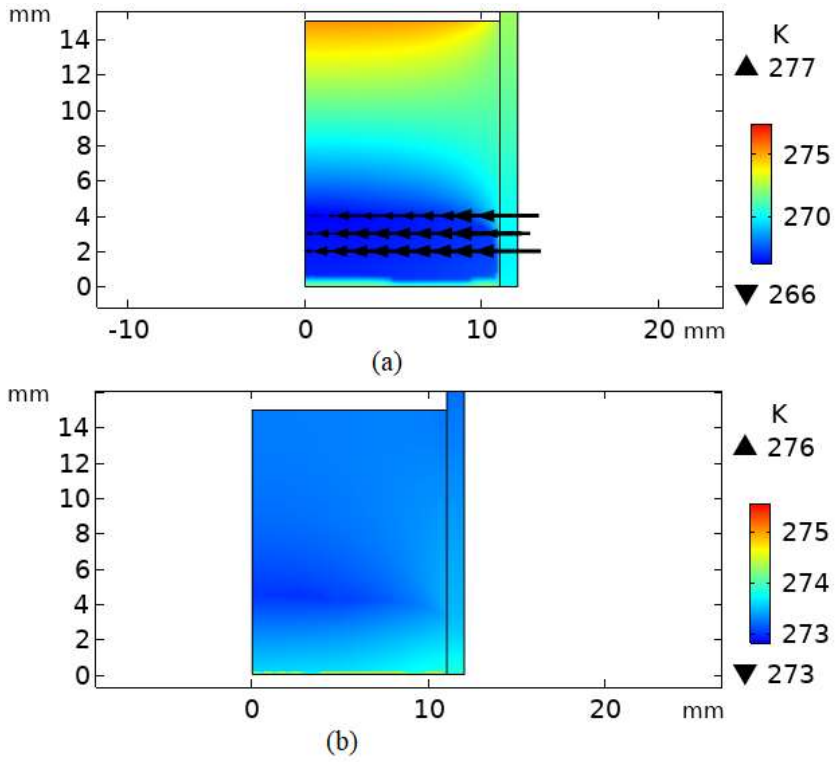

Figure 3.32: (a) DI.60.1, (b) DIA.60. Time set at 15 hours of drying.

As can be seen from Fig. 3.32, there is a huge difference in the heat distribution across the bed between the two different settings. Furthermore, the radial heat fluxes (black arrows) present in the DI.60.1 simulation cannot be seen in DIA.60 setting due to the almost homogeneous temperature distribution.

After the differences between the adiabatic and not adiabatic models were investigated, it was decided to understand the impact of the condensation kinetic constant to the model.

In a first brief analysis, there was expected to see a higher drying time along with the increased condensation kinetic constant due to the bigger amount of water moles which could have condensed. Fig. 3.33 shows the results of the parametric analysis.

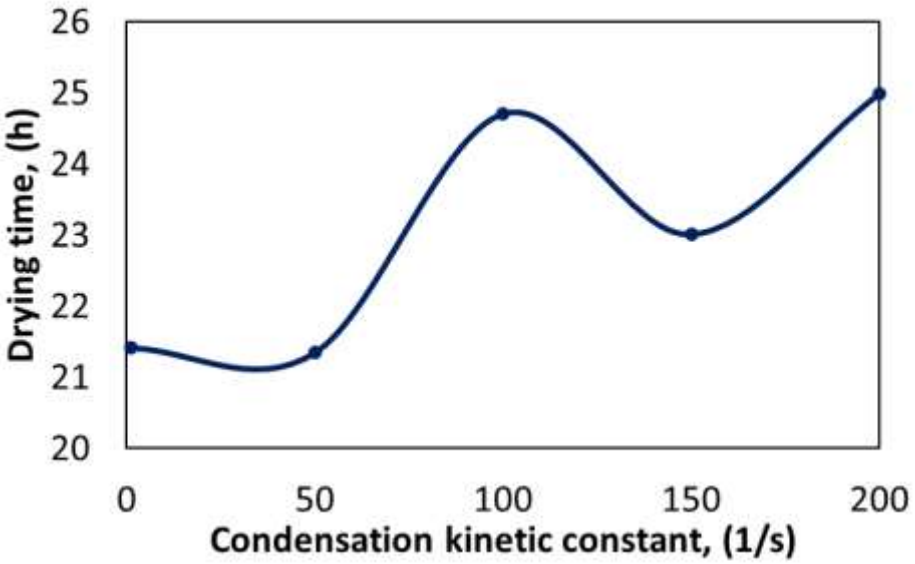

Figure 3.33: Impact of the condensation kinetic constant on the drying time.

As reference model was decided to use the DI.60.# setting because it shown the most accurate behaviour compared to the experimental data. The sublimation kinetic constant could vary from 1 to 200 $[s^{-1}]$ (see Table 2.3 for further details).

As shown in Fig. 3.33, a higher condensation kinetic constant does not mean an increased drying time. Instead, the sinusoidal behaviour suggests the presence of a sort of equilibrium between mass and heat transfers which varies along with the kinetic constant, influencing the overall drying time.

Taking into account both Eqs. (2.3.8), and (2.3.19) it is clear that, increasing the condensation constant mean not only a higher amount of water moles which will condense, but also a higher amount of heat which will be released due to the exothermic phenomenon. The same can be said about varying the sublimation kinetic constant, with an increased amount of heat taken from the bed due to the endothermic phenomenon which goes in contrast with the higher amount of water moles that could sublimate.

This equilibrium can also explain the higher drying time, which was obtained in all the previous results when the pore size within the granules increases (i.e., the sublimation kinetic constant increases).

To study the impact of the dimension of the granules and the pore size within them, as reference value for the condensation kinetic constant was chosen 100 $[s^{-1}]$.

3.2.5 Particle versus bed, mass transport resistance

In this section it will be shown the impact of some particle physical properties on the mass transport mechanism.

First, a comparison between DI.100.100, and DI.1000.100 models will be presented. Fig. 3.34 shows a comparison between the ice distribution across the bed for the two different settings.

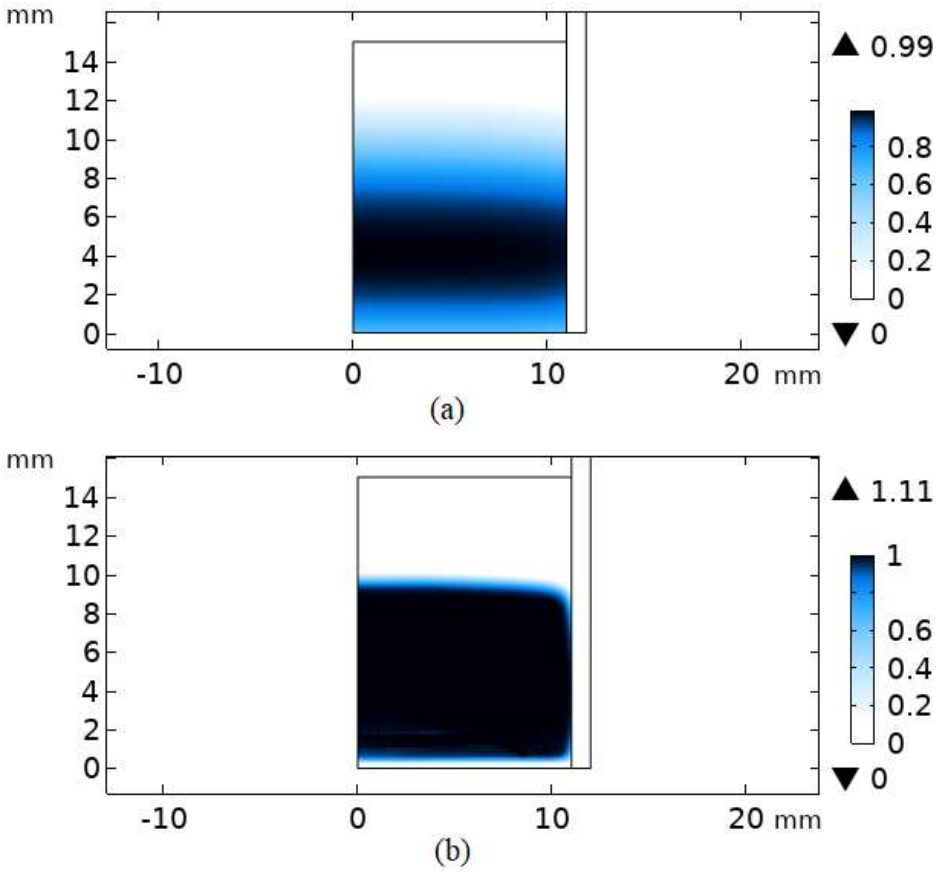

Figure 3.34: (a) DI.1000.100, (b) DI.100.100. Ice saturation distribution. Time set at 5 hours.

As it can be seen from Fig. 3.34, the sublimation front, and the ice distribution in the DI.1000.100 describe an increased capability to evacuate the water vapour flux generated compared to the DI.100.100 simulation. In the DI.1000.100 all the particles in the bed seem to sublimate at the same time, with a slower velocity for the centre bed particles due to the heat transport resistance provided by the surrounding granules, and a higher velocity for the top bed particles due to the boundary conditions.

Fig. 3.35 presents a comparison between the DI.1000.100 and DI.100.100 simulations for the ice saturation profiles in three different points. Fig. 3.36 shows the mean ice saturation profile during the drying for the two different settings.

The DI.100.100 profiles sharply decrease compared to the DI.1000.100 profiles (Fig. 3.35). In the DI.100.100 the controlling mass transport mechanism is the resistance across the bed, which means that the frozen particle is easily dried but the water vapour flux generated slowly flow through the bed. Instead, in the DI.1000.100 due to the huge reduction of the pore size within the granule, the controlling resistance become the resistance across the particle. The granules are no more easily dried as before, and it is required even hours to fully sublimate local points in the bed.

Overall, it can be claimed that the specific weight of the particle permeability, hence the mass transport resistance across the particle compared to the bed one, increases lowering the dimension of the pores within the particles.

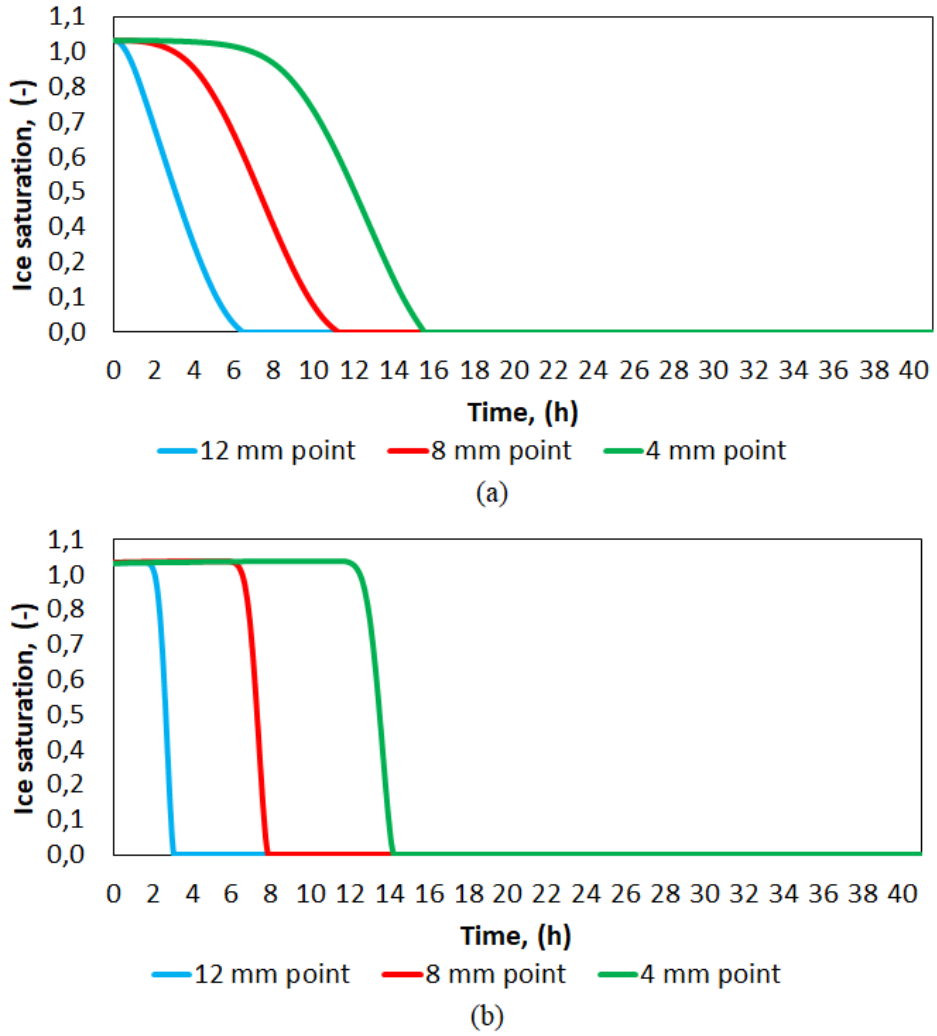

Figure 3.35: (a) DI.1000.100, (b) DI.100.100. Ice saturation profiles for three different points.

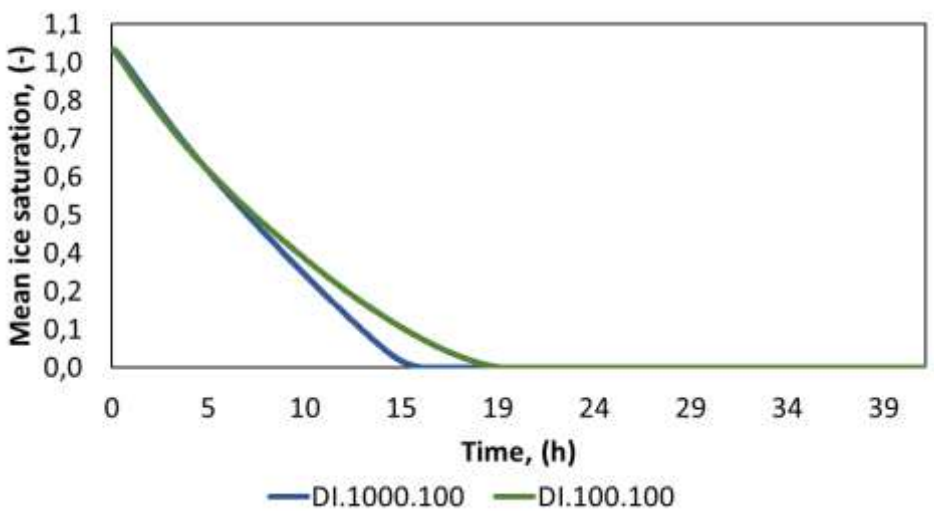

Figure 3.36: (green) DI.1000.100, (blue) DI.100.100. Mean ice saturation of the bed.

When the controlling transport mechanism is the resistance across the particle, the time required to completely dry the packed-bed decreases (Fig. 3.36) because the increased surface specific area of the pores in DI.1000.100 is linked to a lower heat necessary to sublimate the granule (indeed, the time dependent sublimation kinetic constant is lower for the SP.1000 setting compared to that of the SP.100).

After it was studied the impact on the drying performances of the fraction between the granule diameter to the pore size with the particle, it was decided to make a comparison between the DI.100.100 simulation and a setting with the same X parameter, but with a larger particle diameter (i.e., 500 µm). Note that, even if the fraction X is the same, the time dependent sublimation kinetic constant is different for the two simulations (Fig. 3.6).

Some packing descriptors obtained by Ing. Etiopia (2021) cannot be used for the packed-bed with 500 µm particles. To carry out the simulations it was decided to use the theoretical formulas in Tab. 3.7 presented by Capozzi *et al.* (2019a).

Table 3.7: Packing descriptors for 500 µm particles.

Descriptor	**Formula**	**Value**
B_0	$\frac{D_{part}^2}{180}\frac{\varepsilon_{pb}^3}{(1-\varepsilon_{pb})^2}$	2.214E-10 [m^2]
d_{pore}	$\frac{2}{3}D_{part}(1-\varepsilon_{pb})$	2.033E-04 [m]

Fig. 3.37 presents the ice saturation profiles for three different points obtained from DI250.100.100 setting.

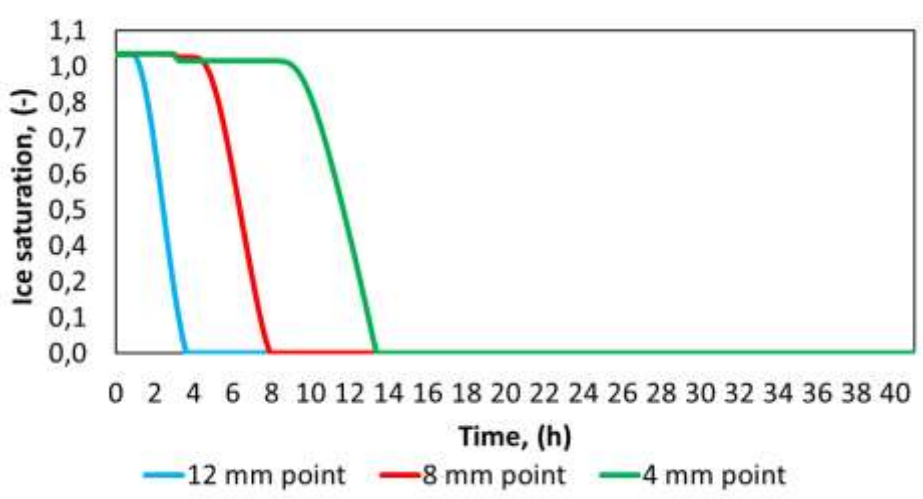

Figure 3.37: Ice saturation profiles for three different points in DI250.100.100 simulation.

The slope of the profiles in Fig. 3.37 is not as steep as that in Fig. 3.35b. Indeed, to fully dry a local point is required about two hours compared to the pseudo-instantaneous drying for the DI.100.100 simulation. This behaviour obtained for the DI250.100.100 setting is linked to larger dried layer which is formed during the particle drying. A bigger dried thickness in the granule (i.e., a larger resistance) increases the specific weight of the mass transport resistance across the particle compared to that of the bed.

The overall drying performance of the simulation (Fig. 3.38) are quite similar to the one shown in Fig. 3.36.

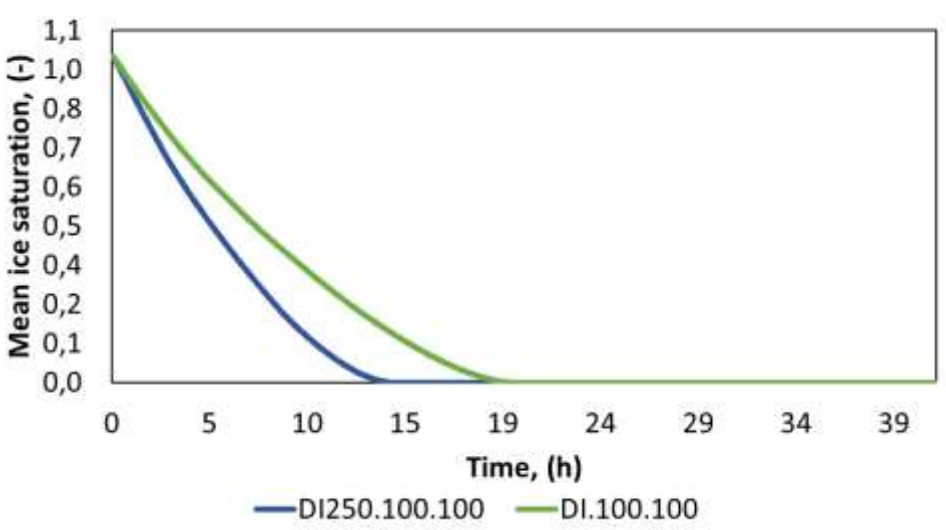

Figure 3.38: (green) DI.100.100, (blue) DI250.100.100. Mean ice saturation of the bed.

Even if the X parameter is the same, the dimension of the pores with the particle for the two simulations are different. The DI.100.100 has smaller pores but also lower bed permeability (about one order of magnitude lower compared to that of the DI250.100.100 setting). Instead, the DI250.100.100 simulation has bigger pores (i.e., bigger specific surface area of the pores) but higher bed permeability.

Overall, from Fig. 3.38 it seems that the impact of the bed permeability is higher compared to the that of the pores dimension, thus it can be claimed that in DI.250.100.100 the controlling mass transport mechanism is still the resistance across the packed-bed. Note that this behaviour does not mean that the specific weight of the mass transport resistance across the particle didn't change, as shown in Fig. 3.35a.

To double check the impact of the X parameter on the drying performance it was also run the DI250.1000.100 simulation. Fig. 3.39 shows the ice saturation profiles for three different points.

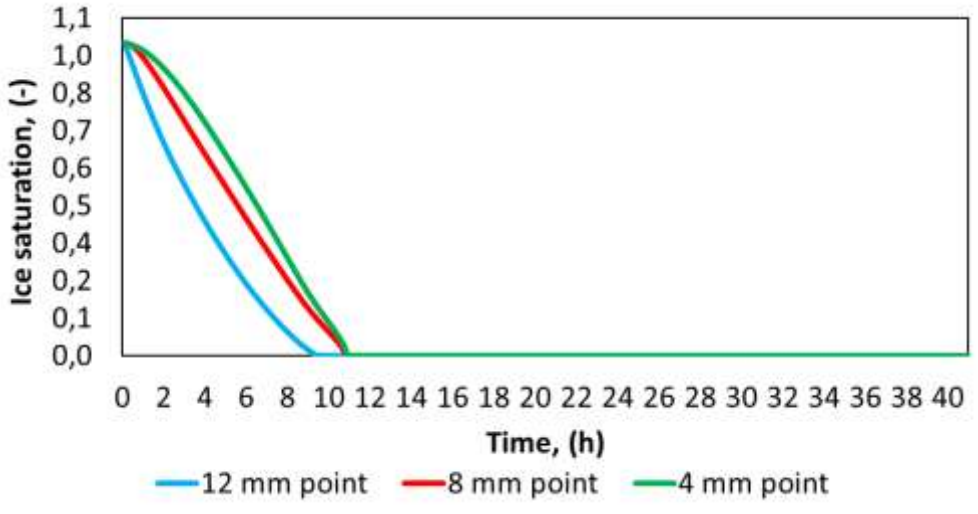

Figure 3.39: Ice saturation profiles for three different points in DI250.1000.100 simulation.

From Fig. 3.39, it can be seen how the packed-bed shown an almost homogeneous drying. The local points started to dry at the same time, and they spent a lot of hours to fully dry. The lowest steepness of the profiles slope suggests that the mass transport controlling mechanism is the resistance across the particle. The almost homogeneous drying is also confirmed in Fig. 3.40 which presents the ice saturation distribution during the drying.

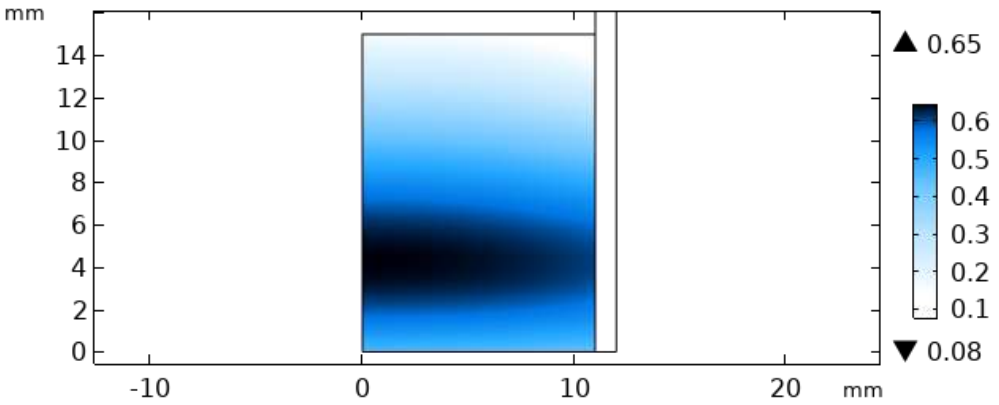

Figure 3.40: DI250.1000.100, ice saturation distribution. Time set at 5 hours.

The different drying velocity obtained in different zones of the packed-bed are linked to the same reason explained for Fig. 3.34a. Overall, the drying obtained for DI250.1000.100 is more homogeneous compared to that of DI250.100.100.

Lastly, Fig. 3.41 presents the mean ice saturation profile of the packed-bed for the DI250.1000.100 simulation.

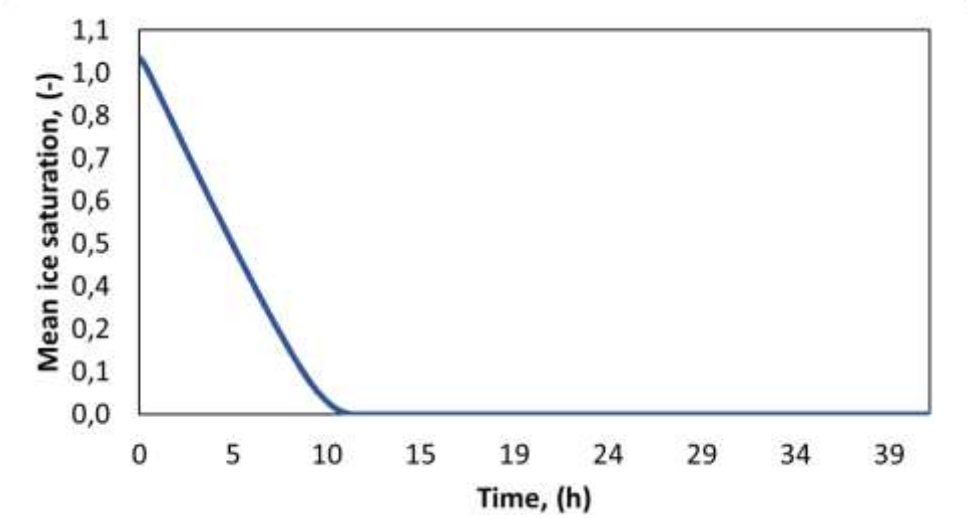

Figure 3.41: Mean ice saturation of the bed for DI250.1000.100 setting.

As obtained for the DI.1000.100, the increased specific surface area of the pores with the particles is linked to a lower heat necessary to sublimate the granules. Thus, the drying time obtained is lower compared to that obtained for DI250.100.100 simulation.

4 Conclusion

The aim of this work was to develop a mathematical model able to predict the behaviour of the packed-bed into vial during the drying phase of the SFD technique.

As was presented in Chapter 1, the transition from batch to continuous pharmaceutical production will solve the problem of the over-increased drugs demand, enhancing manufactory productivity, final product quality and processes control.

The SFD is one of the most promising technique for the development of a continuous lyophilization process. Thanks to this method it is possible to improve mass transfer and heat transfer phenomena during the drying, without compromising the structure and sterility of the final product. Moreover, a controlled homogeneity in both morphology and size of the drugs it is easily achieved.

Fast drying, controlled homogeneity and sterility of the final product, high process flexibility, and low impact on the structure of the active ingredient are all key peculiarity which make mandatory the transition from batch to continuous SFD.

From this great possibility born the necessity of a mathematical model which can predict the packed-bed behaviour during the drying. Thanks to this kind of model, it was possible to understand the role of process parameters such as the particles dimension. Furthermore, it would be possible to deep understand the impact on the final product of other process variables like shelf temperature or vacuum pressure.

As was shown in Chapter 2, other authors tried to develop a model of the drying phase for the SFD. However, both the solutions already proposed derived from a mathematical approach which is usually applied for the simulation of bulk product (i.e., the moving sublimation front). In this work, was decided to develop an innovative approach (i.e., the diffuse interface) which avoid the intrinsic problems derived from using the moving sublimation front and it is able to give enough accurate results.

To develop an accurate model and understand how the phenomena on the microscopic scale influence the results obtained at macroscopic scale, it was necessary to define a physical property (i.e., the sublimation kinetic constant) which is able to link the lyophilization of the particle to the behaviour of the entire packed-bed.

A first single particle model was developed to evaluate the behaviour of the sublimation kinetic constant under different conditions. It has been proved that the kinetic constant varies along whit the pores dimension within the particles due to different permeability of the generated water vapour. Furthermore, was highlighted the fact that for similar pore size dimension within the particle, the more the granule diameter the lower the sublimation kinetic constant due to higher mass transport resistance.

The results obtained with the single particle model were able to give an enough accurate description of the microscopic behaviour of the particle during the drying. Thanks to that, this information was transferred to the diffuse interface model to study the entire packed-bed behaviour during the process.

First, it was analysed the benefits which the diffuse interface can give over the moving sublimation front. A more realistic mass transport description without imposing intrinsic solutions, and parameters constrains were the main reason to support the use of the diffuse model. As was shown in Chapter 3, the water flux generated can overcome the interface resulting in a not sharply ice saturation gradient. Moreover, if the thermodynamic constrains

are respected, condensation phenomena can be locally observed into the packed-bed without generating numerical error propagation.

Then two main aspects were studied to understand the packed-bed behaviour: the impact of heat boundary conditions on the drying and the role of the sublimation kinetic constant.

First, it was observed that when the vial is not adiabatic, a third sublimation front could be generated thanks to the higher temperatures reached in the vial glass. This phenomenon slightly decreases the time needed to dry the packed-bed. A further investigation on the temperature distribution across the bed with experimental technique such as thermal camera could be useful to validate this simulation result.

Then, it was proved that an enhanced particle permeability it is not always linked with a lower packed-bed drying time due to the higher heat required to afford the particle sublimation. Hence, the controlled morphology and size of the SFD products it is a major property to design and control the drying time for a hypothetical continuous process.

Finally, the transport mechanisms behaviour was study comparing different particle physical properties. It was obtained that, varying the particle size can have a huge impact on the controlling mass transport mechanism with the particle resistance which becomes more important along with the increased granule diameter. This last aspect can have a huge impact on the continuous manufactory design due to the different behaviour which various active ingredients can have with different local water concentration. If the active ingredient must be dried rapidly without concerning about the local water concentration, a situation where the mass transport resistance across the particle is the controlling mechanism should be chosen. Instead, if the active principle is strongly denaturised by the water vapour, a configuration where the fluxes are evacuated from the particle as soon as they are generated (i.e., the controlling mechanism is the resistance across the packed-bed) are recommended.

The developing of a mathematical model able to show the physical phenomena occurring during the packed-bed drying was mandatory to understand how the several features offered by the SFD can affect the continuous production of drugs.

A possible step forward, it will be to study a sample of active ingredients and their denaturation to design the best equipment using the diffuse model. The use of the mathematical model will be crucial to couple the needs of the continuous manufactory with the pharmaceutical standards.

Appendices

Appendix A: Single spherical particle model

A.1. Particles number estimation

To calculate the number of particles which are equally receiving the heat Q_{shelf}, it has been supposed that all the heat flux is exchanged with the surfaces of the first layer particles at the bottom of the vial.

Fig. A.1 shown an overhead view of the first bottom layer. A regular packing of the particles was supposed.

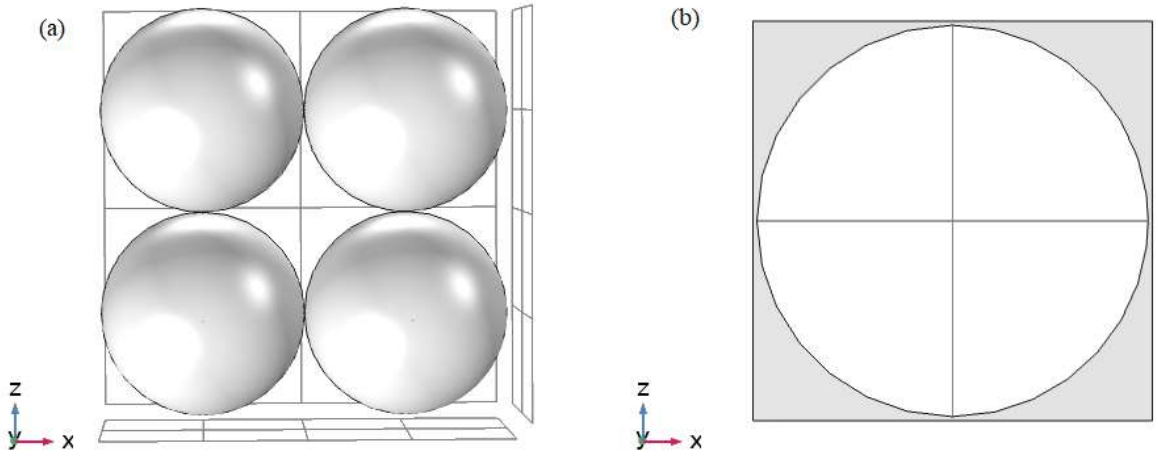

Figure A.1: (a) Overhead view, regular packed particles, (b) Surface void for each particle.

If R_0 is the particle radius, for each particle the degree of surface void (Eq. A.1.1) can be define as the fraction between the void surface (grey space in Fig. A.1, b) to the surface of the square. The void surface is the difference between the surface of the square and the surface of the inscribed circle of radius R_0.

$$\varepsilon_s = \frac{4R_0^2 - \pi R_0^2}{4R_0^2} = 1 - \frac{\pi}{4} \tag{A.1.1}$$

If D_v is the bottom internal diameter of the vial, the occupiable surface by the particles is defined as following (Eq. A.1.2).

$$S_{occ} = \frac{\pi}{4} D_v^2 (1 - \varepsilon_s) \tag{A.1.2}$$

The number of particles in the first bottom layer is defined as the fraction between the occupiable surface and the surface of the circle of radius R_0 (Eq. A.1.3).

$$N_{part} = \frac{S_{occ}}{\pi R_0^2} = \frac{\frac{\pi}{4} D_v^2 (1 - \varepsilon_s)}{\pi R_0^2} = \frac{\pi}{16} \frac{D_v^2}{R_0^2} \tag{A.1.3}$$

Appendix B: Diffuse interface model

B.1. Physical properties estimation

To solve Eqs. (2.3.4), (2.3.5), and (2.3.6) it is necessary to evaluate the physical properties of the packed-bed in frozen and dried zones.

When the particles are full of ice, their physical properties depend on both solid medium and ice characteristics. A weighted average, where the weight is the particle porosity ε_p, it has been used to evaluate the physical properties of frozen granules (Eqs. B.1.1, B.1.2, and B.1.3).

$$\rho_f = (1-\varepsilon_p)\rho_{sol} + \varepsilon_p \rho_{ice} \tag{B.1.1}$$

$$k_f = (1-\varepsilon_p)k_{sol} + \varepsilon_p k_{ice} \tag{B.1.2}$$

$$C_{p_f} = (1-\varepsilon_p)C_{p_{sol}} + \varepsilon_p C_{p_{ice}} \tag{B.1.3}$$

In Eq. (B.1.1), the terms ρ_{sol} and ρ_{ice} represent the solid medium and the ice density, respectively. The same can be assumed for the terms in both Eqs. (B.1.2), and (B.1.3).

When the particles are dried, the pores are full of gas which has its own characteristics. Thus, to evaluate the dried zone physical properties, it is necessary to fully define the gas phase.

First, the gas phase density (Eq. B.1.4) can be calculated starting from the gas component concentrations evaluated thanks to Eqs. (2.3.13), and (2.3.14).

$$\rho_{gas} = C_w M_w + C_{in} M_{in} \tag{B.1.4}$$

The value of the gas specific heat capacity (Eq. B.1.5) has been taken from Table 1 of Liapis and Bruttini (2009) work.

$$C_{p_{gas}} = 1616.6 \text{ Jkg}^{-1}\text{K}^{-1} \tag{B.1.5}$$

The thermal conductivity of the gas phase, due to rarefied conditions, was calculated according to the Kaganer model (Eq. B.1.6):

$$k_{gas} = \frac{k_{gas}^{atm}}{1 + 2\beta K_n} \tag{B.1.6}$$

In Eq. (B.1.6), the terms K_n and k_{gas}^{atm} represents the Knudsen number and the thermal conductivity of the gas phase at atmospheric pressure, respectively. The K_n number can be evaluated according to Eq. (B.1.7).

$$K_n = \frac{\lambda}{d_{pore}} \tag{B.1.7}$$

The term λ in Eq. (B.1.7) is the molecular mean free path (Eq. B.1.8) in the equilibrium hard-sphere gas kinetic model.

$$\lambda = \sqrt{\frac{\sigma T}{2p\pi d_{H2O}^2}} \tag{B.1.8}$$

The terms σ and d_{H2O} represent the Boltzmann constant and the water molecular diameter, respectively.

The term d_{pore} in Eq. (B.1.7) is the diameter of the channels generated by the porous matrix of the packed-bed.

The number β is the so called temperature jump distance and is defined according to Eq. (B.1.9).

$$\beta = \frac{2-\alpha}{\alpha\beta^*} \tag{B.1.9}$$

The terms α and β^* are the accommodation coefficient and a corrective factor, respectively. These values (Eqs. B.1.10, and B.1.11) were taken from the Capozzi *et al*. (2019a) model.

$$\alpha = 0.98 \tag{B.1.10}$$

$$\beta^* = 1.42 \tag{B.1.11}$$

Starting from the gas phase characteristics, it is possible to define the physical properties of the dried zones in the packed-bed. To evaluate the density and the specific heat capacity, it has been used the same weighted average as in frozen zones (Eqs. B.1.12, and B.1.13). Instead, to estimate the thermal conductivity of the dried zones, Eq. (B.1.14) was used.

$$\rho_d = (1-\varepsilon_p)\rho_{sol} + \varepsilon_p\rho_{gas} \tag{B.1.12}$$

$$C_{p_d} = (1-\varepsilon_p)C_{p_{sol}} + \varepsilon_p C_{p_{gas}} \tag{B.1.13}$$

$$k_d = k_{sol}\frac{2k_{sol} + k_{gas} - 2\varepsilon_p(k_{sol} - k_{gas})}{2k_{sol} + k_{gas} + \varepsilon_p(k_{sol} - k_{gas})} \tag{B.1.14}$$

B.2. Overall heat transfer coefficient

Direct conduction from the heated shelf to the vial at the points of contact, the radiation and the conduction in the gap are the three different mechanisms governing the heat transport at the bottom of the vial. Fig. B.1 reports a scheme of the contributors to the heat transport.

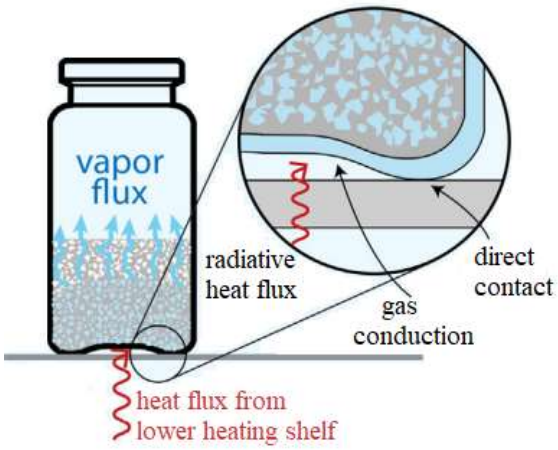

Figure B.1: Contributions to the overall heat transport coefficient at the vial bottom. Capozzi *et al*. (2019a).

According to Pisano *et al*. (2011), due to the different mechanism involved in the heat transport at the bottom of the vial and the rarefied conditions, the heat transfer coefficient between shelf and vials varies with temperature and chamber pressure (Eq. B.2.1).

$$K_v' = C_1 + \frac{C_2 p_c}{1 + C_3 p_c} \tag{B.2.1}$$

The coefficients (Eq. B.2.2) present in Eq. (B.2.1) are a function of the separation distance between vials and shelf, and the absolute temperature.

$$\begin{cases} C_1 = K_c + 4\sigma\overline{T^3}(e_s - e_v) \\ C_2 = \dfrac{\alpha}{2-\alpha}\sqrt{\dfrac{273.2}{T}}\Lambda_0 \\ C_3 = l_0\left(\dfrac{\Lambda_0}{\lambda}\dfrac{\alpha}{2-\alpha}\sqrt{\dfrac{273.2}{T}}\right) \end{cases} \tag{B.2.2}$$

While the values of Λ_0, λ and the shelf emissivity (e_s) can be found in literature, designed experiments need to be prepared in order to obtain the heat transport contact coefficient (K_c), the separation distance l_0, the accommodation coefficient α and the emissivity e_v.

Known the value of the heat transfer coefficient between the shelf and the vial, it is possible to calculate the overall heat transfer coefficient K_v (Eq. B.2.3). To do that, the heat transport resistance in the vial material and the heat transport coefficient between the heating fluid and the shelf are needed.

$$K_v = \left(\frac{s_{glass}}{k_{glass}} + \frac{1}{K'_v} + \frac{1}{K_s}\right)^{-1} \tag{B.2.3}$$

In Eq. (B.2.3) the terms K_s and s_{glass} represent the heat transport resistance in the vial material and the glass thickness, respectively.

Usually, the value of the overall heat transport coefficient is not evaluated through Eqs. (B.2.2), and (B.2.3) but thanks to gravimetric experiments.

B.3. DGM coefficients

To solve Eqs. (2.3.15), and (2.3.16) it is necessary to define the coefficient deriving from the dusty-gas model. The coefficients multiplying the total pressure gradient (Eqs. B.3.2, and B.3.4) describe the pressure contribution to molecular diffusion and viscous flow. Instead, the coefficients multiplying the partial pressure gradient (i.e., concentration gradient, Eqs. B.3.1, and B.3.3) describe concentration contribution to molecular diffusion.

$$c_1 = \frac{D_w^{Kn} D_{w,in}^{eff}}{D_{w,in}^{eff} + y_w D_{in}^{Kn} + y_{in} D_w^{Kn}} \tag{B.3.1}$$

$$c_2 = \frac{D_w^{Kn}(D_{w,in}^{eff} + D_{in}^{Kn})}{P(D_{w,in}^{eff} + y_w D_{in}^{Kn} + y_{in} D_w^{Kn})} + \frac{B_0}{\mu_{gas}}\left(1 + \frac{\varepsilon_{pb}}{(1-\varepsilon_{pb})\varepsilon_p} - S\right) \tag{B.3.2}$$

$$c_3 = \frac{D_{in}^{Kn} D_{w,in}^{eff}}{D_{w,in}^{eff} + y_w D_{in}^{Kn} + y_{in} D_w^{Kn}} \tag{B.3.3}$$

$$c_4 = \frac{D_{in}^{Kn}(D_{w,in}^{eff} + D_w^{Kn})}{P(D_{w,in}^{eff} + y_w D_{in}^{Kn} + y_{in} D_w^{Kn})} + \frac{B_0}{\mu_{gas}}\left(1 + \frac{\varepsilon_{pb}}{(1-\varepsilon_{pb})\varepsilon_p} - S\right) \tag{B.3.4}$$

In the above equations, the terms B_0 and μ_{gas} represent the bed permeability and the gas viscosity, respectively.

When S is equal to zero, the permeability value is the one estimated by Ing. F. Etiopia (see Sec. 2.5.1). Instead, an ice saturation increment leads to a lower bed permeability until the total bed porosity is nullified. Note that the term between brackets that multiplies the bed permeability is null when the total bed porosity is equal to zero.

To calculate the coefficients, for both the gas components it is necessary to calculate effective Knudsen diffusivity (Eqs. B.3.5, and B.3.6) and the effective binary diffusivity (Eq. B.3.7).

$$D_w^{Kn} = \frac{\varepsilon_{tot}}{\tau^2}\frac{d_{pore}}{3}\sqrt{\frac{8RT}{\pi M_w}} \tag{B.3.5}$$

$$D_{in}^{Kn} = \frac{\varepsilon_{tot}}{\tau^2}\frac{d_{pore}}{3}\sqrt{\frac{8RT}{\pi M_{in}}} \tag{B.3.6}$$

$$D_{w,in}^{eff} = \frac{\varepsilon_{tot}}{\tau^2} D_{w,in} \tag{B.3.7}$$

In Eqs. (B.3.5), and (B.3.6) the term τ represents the bed tortuosity. In Eq. (B.3.7) the term $D_{w,in}$ represents the binary diffusivity in a non-porous medium. Eqs. (B.3.5), (B.3.6), and (B.3.7) are diffusivity correction due to rarefied condition and porous matrix present in the packed-bed.

When the ice saturation reaches a value able to nullify the total bed porosity, all the above equations will be equal to zero.

Appendix C: Single particle model simulation pictures

Fig. C.1 presents the dried layer temperature 3D profiles extracted from SP.100, SP.60, and SP.30 simulations. All the shown profiles are obtained at the end of the particle drying.

Fig. C.2 reports the water vapour 3D profiles extracted from SP.100, SP.60, and SP.30 simulations. All the shown profiles are obtained at the end of the particle drying. Note that in this case the profile takes into account all the domains of the granule.

Fig. C.3 presents the mesh quality 3D profiles extracted from SP.100, SP.60, and SP.30 simulations. All the shown profiles are obtained before the last remeshing of the particle mesh.

Fig. C.4 shows the water vapour, temperature, and mesh quality 3D profiles from the SP.100.10.

Fig C.5 shows a comparison between the water vapour flux across the interface from the SP.100.10 and the SP.100 simulations.

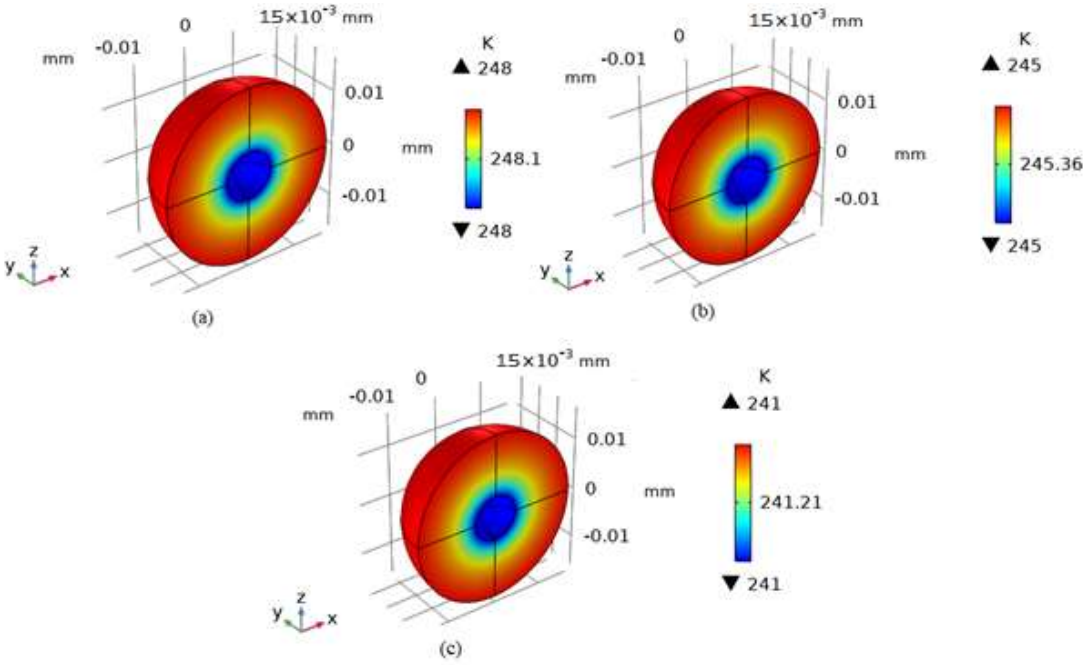

Figure C.1: (a) SP.100, (b) SP.60, (c) SP.30, dried layer temperature 3D profile at the end of the drying step.

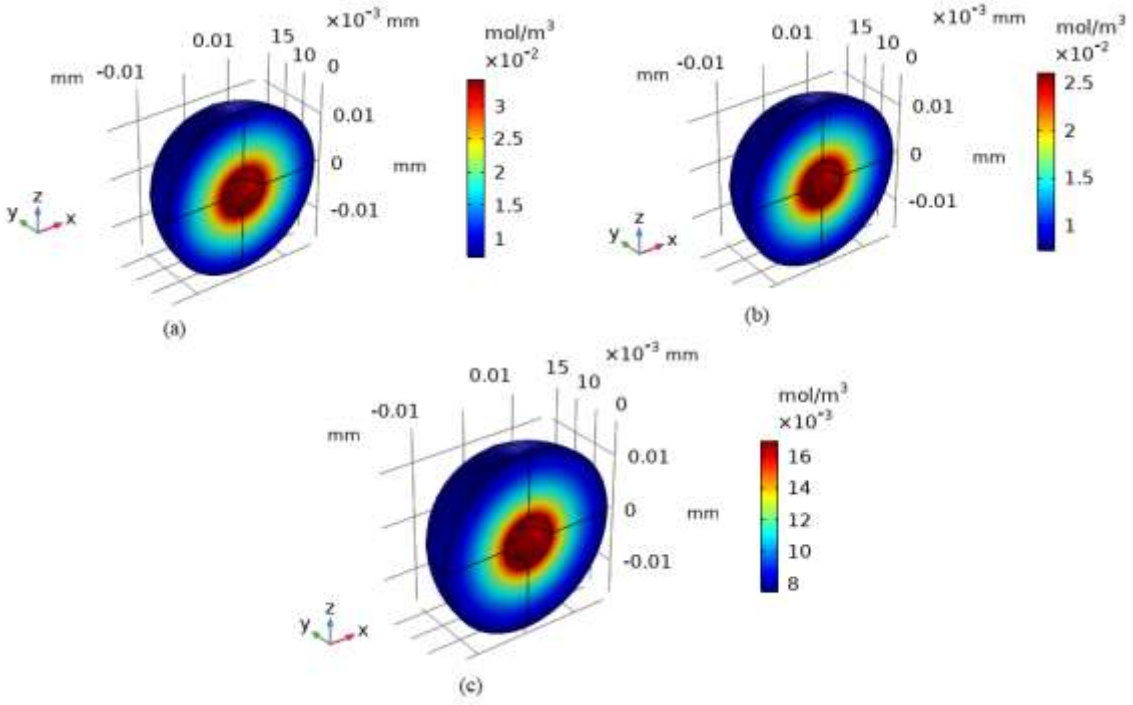

Figure C.2: (a) SP.100, (b) SP.60, (c) SP.30, water vapour 3D profile at the end of the drying step.

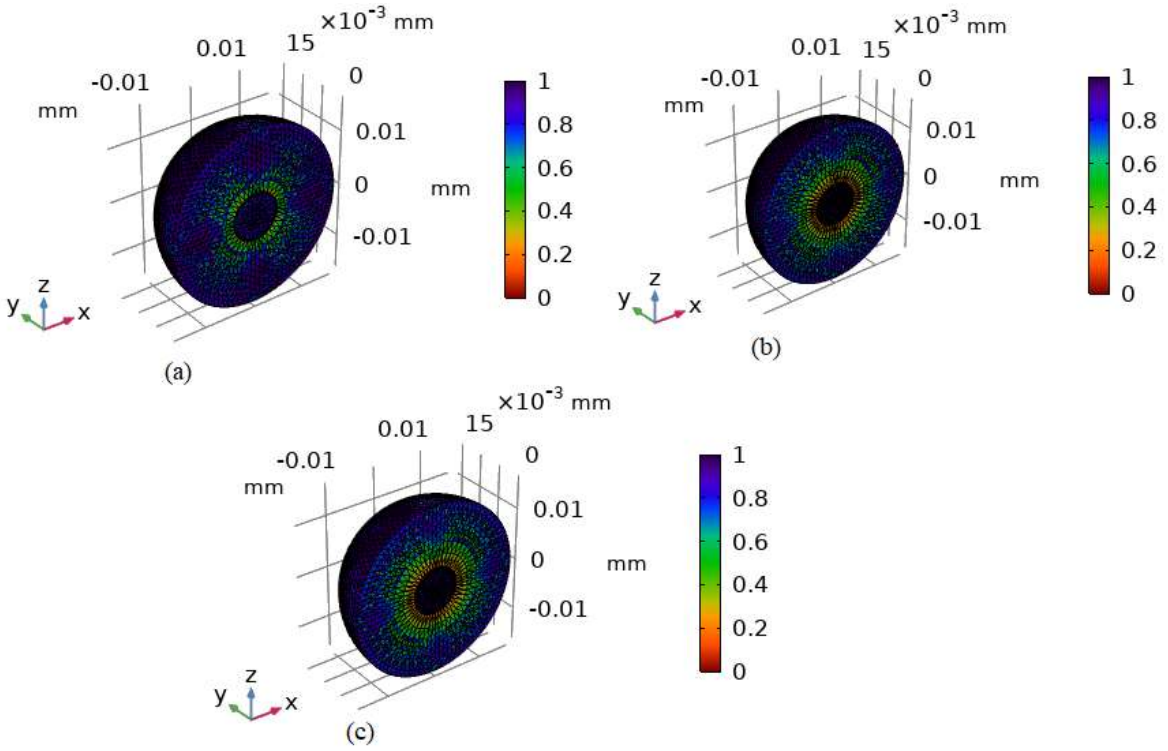

Figure C.3: (a) SP.100, (b) SP.60, (c) SP.30, mesh quality 3D profile before the last remeshing.

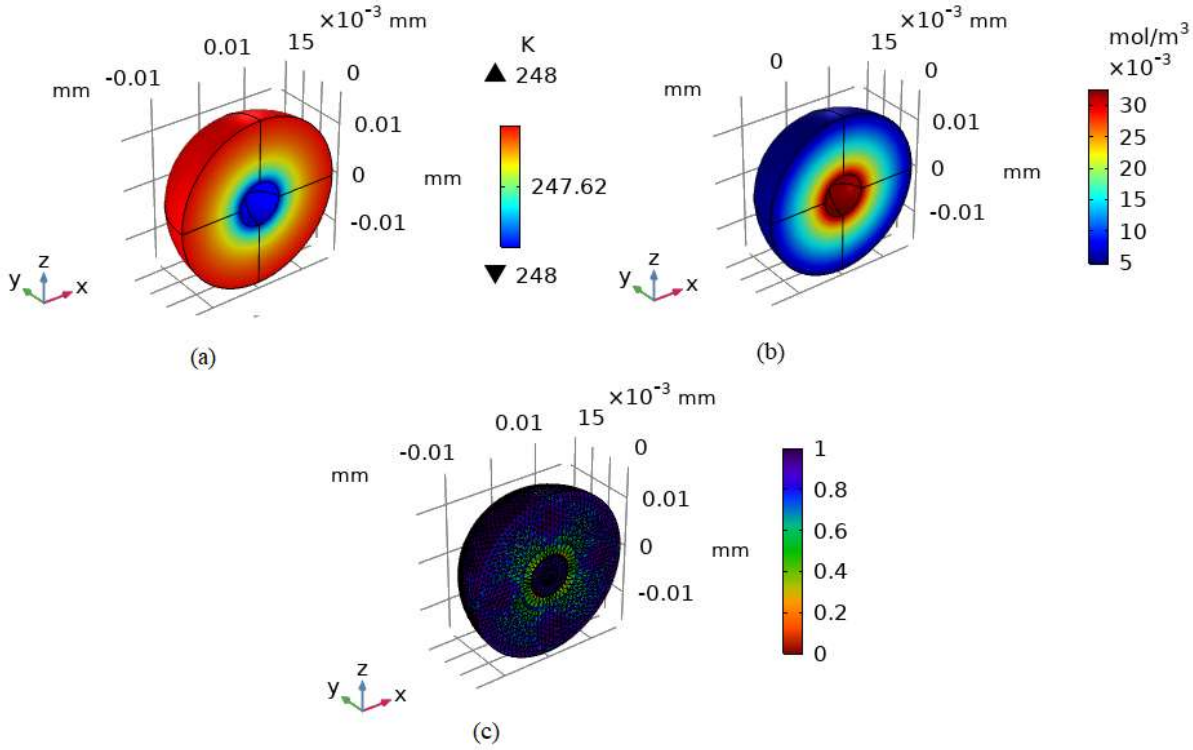

Figure C.4: (a) Dried layer temperature, (b) Water vapour, (c) Mesh quality 3D profiles. Obtained from SP.100.10 simulation.

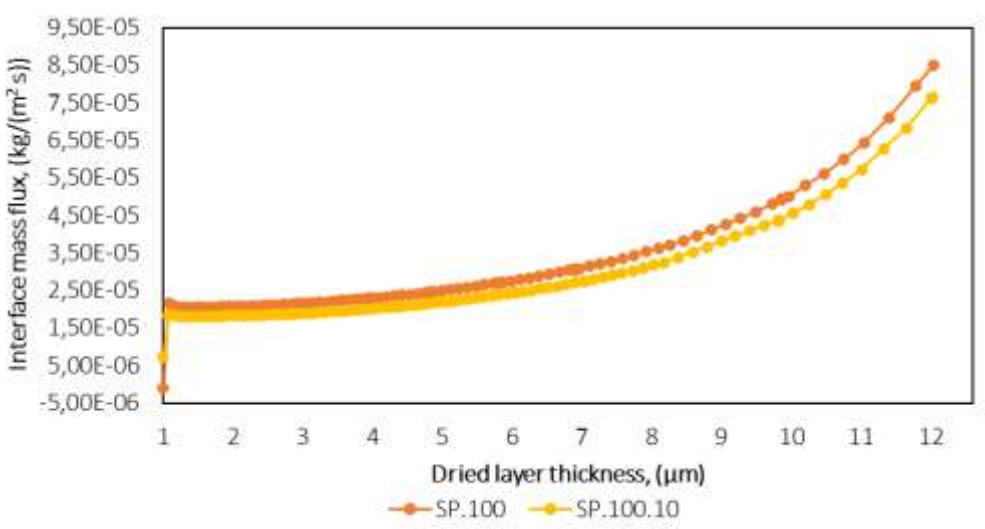

Figure C.5: SP.100 (orange), and SP.100.10 (yellow) water mass flux across the interface.

Bibliography

Adali M. B, Barresi A. A., Boccardo G., and Pisano R., 2020. Spray freeze-drying as a solution to continuous manufacturing of pharmaceutical products in bulk. *Processes*. **8.6**, 709.

Alexeenko, A.A., Ganguly, A. and Nail, S.L., 2009. Computational analysis of fluid dynamics in pharmaceutical freeze-drying. *J. Pharm. Sci*. **98,** 3483-3494.

Alvarez A.J., Singh A. and Myerson A.S., 2011. Crystallization of cyclosporine in a multistage continuous MSMPR crystallizer. *Cryst. Growth Des*. **11**(10), 4392–4400.

Anandharamakrishnan C., Rielly C.D., and Stapley A.G.F., 2010. Spray-freeze-drying of whey proteins at sub-atmospheric pressures. *Dairy Sci. Technol*. **90**, 321–334.

Arsem H.-B., 1986. *Continuous freeze drying*. U.S. Patent Appl. No. US 4590684, 05 1986.

Badman C., Cooney C. L., Florence A., Konstantinov K., Krumme M., Mascia S., Nasr M. and Trout B. L., 2019. Why we need continuous pharmaceutical manufacturing and how to make it happen. *J. Pharm. Sci*. **108**, 3521-3523.

Bonde, M., 1998. Continuous granulation. In: *Parikh, D. (Ed.), Handbook of Pharmaceutical Granulation Technology*. Marcel Dekker Inc, New York, 369–387.

Borchert C., Nere N., Ramkrishna D., Voigt A. and Sundmacher K., 2009. On the prediction of crystal shape distributions in a steady-state continuous crystallizer. *Chem. Eng. Sci.* **64**(4), 686–696.

Bruttini R., 1993. *Continuous freeze drying apparatus*. U.S. Patent Appl. No. US 5269077, 12 1993.

Bullich R., 2015. Telstar industry session: continuous freeze drying, Presented at *Pharmaprocess forum*, Barcelona, 28 October 2015.

Capozzi L. C, Barresi A. A., and Pisano R., 2019a. A multi-scale computational framework for modeling the freeze-drying of microparticles in packed-beds. *Powder Technology.* **343**, 834-846.

Capozzi L. C., Barresi A. A., and Pisano R., 2019b. Supporting data and methods for the multi-scale modelling of freeze-drying of microparticles in packed-beds. *Data in Brief*. **22**, 722-755.

Claussen I.C., Ustad T.S., Strømmen I., and Walde, P.M., 2007. Atmospheric freeze drying—A review. *Dry. Technol*. **25**, 947–957.

Corver J.A.W.M., 2012. *Method and system for freeze-drying injectable compositions, in particular pharmaceutical compositions*. U.S. Patent Appl. No. US 2014/0215845, 08 2012.

Costantino H.R., Firouzabadian L., Hogeland K., Wu C., Beganski C., Carrasquillo K.G., Córdova M., Griebenow K., Zale S.E., and Tracy M.A, 2000. Protein spray-freeze drying. Effect of atomization conditions on particle size and stability. *Pharm. Res*. **17**, 1374–1383.

D'Addio S.M., Chan J.G.Y., Kwok P.C.L., Benson B.R., Prud'homme R.K., and Chan H.K., 2013. Aerosol delivery of nanoparticles in uniform mannitol carriers formulated by ultrasonic spray freeze-drying. *Pharm. Res*. **30** (11), 2891–2901.

De Meyer L., Van Bockstal P.-J., Corver J., Vervaet C., Remon J., De Beer T., 2015. Evaluation of spin freezing versus conventional freezing as part of a continuous pharmaceutical freeze-drying concept for unit doses. *Int. J. Pharm.* **496** (1), 75–85.

Dombrowski R.D., Litster J.D., Wagner N.J. and He Y., 2007. Crystallization of alpha-lactose monohydrate in a drop-based microfluidic crystallizer. *Chem. Eng. Sci.* **62**(17), 4802–4810.

Dream R, 2017. Continuous manufacturing progress and the bio/pharmaceutical industry "reality or fad". *American Pharmaceutical Review.* Available at www.americanpharmaceuticalreview.com/Featured-Articles/341193-Continuous-Manufacturing-Progress-and-the-Bio-Pharmaceutical-Industry-Reality-or-Fad/. Last login: 03/08/2021.

Engstrom, J.D., Simpson, D.T., Cloonan, C., Lai, E.S., Williams, R.O., Barrie Kitto, G., and Johnston, K.P, 2007. Stable high surface area lactate dehydrogenase particles produced by spray freezing into liquid nitrogen. *Eur. J. Pharm. Biopharm*. **65**, 163–174.

Etiopia, F., 2021. Calcolo delle proprietà di trasporto in letti impaccati di microparticelle ottenute via congelamento spray. Master thesis, Politecnico di Torino, Turin, Italy.

Ferguson S., Ortner F., Quon J., Peeva L., Livingston A., Trout B.L., et al., 2014. Use of continuous MSMPR crystallization with integrated nanofiltration membrane recycle for enhanced yield and purity in API crystallization. *Cryst. Growth Des*. **14**(2), 617–627.

Fuentevilla M., 1966. *Method and apparatus for continuous freeze drying*. U.S. Patent Appl. No. US 3264747, 08 1966.

Krok A., Vitorino N., Zhang J., Frade J. R., and Wu C. Y., 2017. Thermal properties of compacted pharmaceutical excipients. *Int. J. Pharm*. **534.1-2**, 119-127.

Lee S. L., 2017. Modernizing the way drugs are made: a transition to continuous manufacturing. *U.S. Food & Drug Administration*. Available at www.fda.gov/drugs/news-events-human-drugs/modernizing-way-drugs-are-made-transition-continuous-manufacturing. Last login: 03/08/2021.

Liapis A.I, and Bruttini R., 2009. A mathematical model for the spray freeze drying process: The drying of frozen particles in trays and in vials on trays. *Int. J. of Heat and Mass Transfer*. **52.1**, 100-111.

Lombardo C., 2021. *Spray freeze-drying of a solution containing lactate dehydrogenase*. Master thesis, Politecnico di Torino, Turin, Italy.

Machado M., Moreira P., Flores P., and Lankarani H.M., 2012. Compliant contact force models in multibody dynamics: evolution of the Hertz contact theory. *Mech. Mach. Theory.* **53**, 99–121.

Marti J., and Mauersberger K., 1993. A survey and new measurements of ice vapor pressure at temperatures between 170 and 250 K. *Geophys. Res. Lett*. **20**, 363–366.

Mason E.A., and Malinauskas A.P., 1983. *Gas Transport in Porous Media: The Dusty-Gas Model.* Elsevier, New York, NY, USA.

Mascia S., Heider P. L., Zhang H., Lakerveld R., Benyahia B., Barton P. I., Braatz R. D., Cooney C. L., Evans J. M. B., Jensen K. F., Myerson A. S. and Trout B. L., 2013. End-to-end continuous manufacturing of pharmaceuticals: integrated synthesis, purification, and final dosage formation. *Angewandte Chemie*. **52.47** (International Ed.), 12359-12363.

Masters, K., 2002. Process stages and spray drying systems. In: *Masters, K. (Ed.), Spray Drying in Practice.* Spray Dry Consult International, Charlottenlund, 39–96.

Meryman H.T., 1956. Sublimation freeze-drying without vacuum. *Science* **130**, 628–629.

Oddone I., Pisano R., Bullich R., Stewart P., 2014. Vacuum-induced nucleation as a method for freeze-drying cycle optimization. *Ind. Eng. Chem. Res.* **53**, 18236–18244.

Oddone I., Van Bockstal P.-J., De Beer T., Pisano R., 2016. Impact of vacuum-induced surface freezing on inter-and intra-vial heterogeneity. *Eur. J. Pharm. Biopharm*. **103**, 167–178.

Oetjen G., Schmitz F., Eilenberg H., 1971. *Continuous freeze-dryer*. U.S. Patent Appl. No. US 3612411, 10 1971.

Otake H., Okuda T., and Okamoto H., 2016. Development of spray-freeze-dried powders for inhalation with high inhalation performance and antihygroscopic property. *Chem. Pharm. Bull*. **64**, 239–245.

Padmanabhan B., 2017. True continuous manufacturing. *Pharma Manufacturing.* Available at www.pharmamanufacturing.com/articles/2017/true-continuous-manufacturing. Last login: 03/08/2021.

Parthasarathi S., and Anandharamakrishnan C., 2016. Enhancement of oral bioavailability of vitamin E by spray-freeze drying of whey protein microcapsules. *Food Bioprod. Process*. **100**, 469–476.

Pisano R., 2020. Continuous manufacturing of lyophilized products: why and how to make it happen. *Am. Phar. Rev.* **23**(3), 1-4.

Pisano R., Arsiccio A., Capozzi L.C., and Trout B.L, 2019. Achieving continuous manufacturing in lyophilization: Technologies and approaches. *Eur. J. of Pharm. Biopharm.* **142**, 265-279.

Pisano R., Fissore D., and Barresi A. A, 2011. Heat transfer in freeze-drying apparatus, in *Developments in Heat Transfer*, InTech, Rijeka, Croatia, 92-114.

Quon J.L., Zhang H., Alvarez A., Evans J., Myerson A.S. and Trout B.L., 2012. Continuous crystallization of aliskiren hemifumarate. *Cryst. Growth Des*. **12**(6), 3036–3044.

Reitzle M., Ruberto S., Stierle R., Gross J., Janzen T., and Weigand B., 2019. Direct numerical simulation of sublimating ice particles. *Inter. J. Therm. Sci*. **145**, 105953.

Rey L., and May J. C., 2010. Glimpses into the realm of freeze-drying: classical issues and new ventures, in *Freeze-Drying/Lyophilization of Pharmaceutical and Biological Products*, CRC Press, New York, USA.

Rogers T.L., Nelsen A.C., Sarkari M., Young T.J., Johnston K.P., and Williams R.O., 2003. Enhanced aqueous dissolution of a poorly water soluble drug by novel particle engineering technology: Spray-freezing into liquid with atmospheric freeze-drying. *Pharm. Res.* **20**, 485–493.

Schaber S.D., Gerogiorgis D.I., Ramachandran R., Evans J.M.B., Barton P.I. and Trout B.L., 2011. Economic analysis of integrated continuous and batch pharmaceutical manufacturing: A case study. *Ind. Eng. Chem. Res.* **50**(17), 10083–10092.

Schiffter H., Condliffe J., and Vonhoff S., 2010. Spray-freeze drying of nanosuspensions: the manufacture of insulin particles for needle-free ballistic powder delivery. *J. R. Soc. Interface*. **7** (Suppl. 4), S483–S500.

Schroeder, R., 2004. Planetary roller. Presented at: *Novel approaches for oral solid dosage forms*. ISPE, Brussels, Belgium, 13–14 May.

Trout B.L., Pisano R. and Capozzi L.C., 2018. *Continuous freeze-drying methods and related products*. International Patent Application WO 2018/204484 A1 filed 05 2, 2018.

Van der Wel P.-G.-J., 2015. Active freeze drying, *Proceedings of 5th European Drying Conference*, Budapest, 21–23 October.

Vetter T., Burcham C.L. and Doherty M.F., 2014. Regions of attainable particle sizes in continuous and batch crystallization processes. *Chem. Eng. Sci.* **106**, 167–180.

Vigano G., 1966. *Process and equipment for the continuous lyophilization of liquid substances*. U.S. Patent Appl. No. US 3257731, 07 1966.

Vishali, D.A, Monisha J., Sivakamasundari S.K, Moses J.A, and Anandharamakrishnan C., 2019. Spray freeze drying: Emerging applications in drug delivery. *J. Contr. Rel.* **300**, 93-101.

Wang Z.L., Finlay W.H., Peppler M.S., and Sweeney L.G, 2006. Powder formation by atmospheric spray-freeze-drying. *Powder Technol*. **170**, 45–52.

Weisselberg E., 2013. *Apparathus and method for continuous lyophilization*. U.S. Patent Appl. No. US 8528225, 09 2013.

Williams, R., Johnston, K., Young, T., Rogers, T., Barron, M., Yu, Z., and Hu, J, 2005. *Process for production of nanoparticles and microparticles by spray freezing into liquid*. U.S. Patent Appl. No. US 6862890 B2, 8 03 2005.

Yu Z., Rogers T.L., Hu J., Johnston K.P., and Williams R.O., 2002. Preparation and characterization of microparticles containing peptide produced by a novel process: Spray freezing into liquid. *Eur. J. Pharm. Biopharm*. **54**, 221–228.

Zhang D., Shijie X., Shichao D., Jingkang W., and Junbo G., 2017. Progress of pharmaceutical continuous crystallization. *Engineering.* **3.3**, 354-364

Zhang F., Ma X., Wu X., Xu Q., Tian W., and Li Z., 2020. Inert particles as process aid in spray-freeze drying. *Dry. Technol*. **38**, 71–79.

Zhao L., Raval V., Briggs N.E.B., Bhardwaj R.M., McGlone T., Oswald I.D.H. et al., 2014. From discovery to scale-up: α-lipoic acid: Nicotinamide co-crystals in a continuous oscillatory baffled crystalliser. *Cryst. Eng. Comm.* **16**(26), 5769–5780.

List of symbols

Single spherical particle model

$[A]$	concentration of component A, mol m^{-3}
ΔH_s	latent heat of sublimation, J kg^{-1}
B_0	particle permeability, m^2
C_p	specific heat capacity, J kg^{-1} K^{-1}
D	thickness, m
k	thermal conductivity, J s^{-1} m^{-1} K^{-1}
K_v	overall heat transfer coefficient, J s^{-1} m^{-2} K^{-1}
M_w	water molecular weight, kg mol^{-1}
N	mass flux, kg m^{-2} s^{-1}
n	normal vector, -
N_{part}	number of particles, -
p	pressure, Pa
Q	heat, J s^{-1}
R	ideal gas constant, J mol K^{-1}
R_0	particle radius, m
S	surface, m^2
T	temperature, K
u	fluid velocity, m s^{-1}
V	volume, m^3

Diffuse interface model

ΔH_s	latent heat of sublimation, J kg^{-1}
B_0	bed permeability, m^2
C	concentration, mol m^{-3}
c_1	DGM constant, m^2 s^{-1}
c_2	DGM constant, m^3 s^1 kg^{-1}
c_3	DGM constant, m^2 s^{-1}
c_4	DGM constant, m^3 s^1 kg^{-1}
C_1	heat transfer coefficient constant, J s^{-1} m^{-2} K^{-1}
C_2	heat transfer coefficient constant, Pa^{-1}
C_3	heat transfer coefficient constant, Pa^{-1}
C_p	specific heat capacity, J kg^{-1} K^{-1}
d_{pore}	bed channels diameter, m

d_{H2O}	water molecular diameter, m
D	diffusivity, $m^2\ s^{-1}$
e	emissivity, -
F_w	wall view factor, -
F_{ls}	lower shelf view factor, -
G_w	water generation term, $mol\ m^{-3}\ s^{-1}$
Kn	Knudsen number, -
K_v	overall heat transfer coefficient, $J\ s^{-1}\ m^{-2}\ K^{-1}$
K_s	vial heat transport resistance, $J\ s^{-1}\ m^{-2}\ K^{-1}$
k	thermal conductivity, $J\ s^{-1}\ m^{-1}\ K^{-1}$
l_0	separation distance, m
M	molecular weight, $kg\ mol^{-1}$
N	mass flux, $kg\ m^{-2}\ s^{-1}$
n	normal vector, -
p	partial pressure, Pa
P	total pressure, Pa
p_w^{sat}	ice saturation pressure, Pa
Q	heat for unit of volume, $J\ s^{-1}\ m^{-3}$
R	ideal gas constant, $J\ mol\ K^{-1}$
r	r-coordinate, m
s	thickness, m
S	ice saturation, -
T	temperature, K
t	time, s
z	z-coordinate, m

Greek letters

Single spherical particle model

ε_p	particle porosity, -
λ	phase change interface velocity, $m\ s^{-1}$
μ	viscosity, Pa s
ν	kinetic constant, $\left(\frac{mol}{m^{-3}}\right)^{-(n+m-1)}\ s^{-1}$
ρ	density, $kg\ m^{-3}$
Ω	domain, -

Diffuse interface model

α	accommodation energy coefficient, -
β	temperature jump distance, -
β^*	corrective factor, -
ε	porosity, -
λ	molecular mean free path, m
μ	gas viscosity, Pa s
ν_c	condensation kinetic constant, s^{-1}
ν_s	sublimation kinetic constant, s^{-1}
ρ	density, kg m^{-3}
σ	Stefan-Boltzmann constant, $J\,s^{-1}\,m^{-2}\,K^{-4}$
τ	tortuosity, -

Subscripts

Single spherical particle model

bottom	vial bottom
dried	dried domain
i	initial
I	dried domain
II	frozen domain
int	interface
interf	interface
part	particles
ref	reference
s	sublimation
shelf	heating shelf
sol	solid
source	heating source
vac	vacuum
w	water
wv	water vapour

Diffuse interface model

bed	particle packed-bed

c	chamber
d	dried
f	frozen
gas	gas phase
gen	generated
glass	glass vial
i	initial
ice	ice
in	inert
int	integral
p	particle
pb	particle bed
s	shelf
shelf	heating shelf
sol	solid
t	total
tot	total
v	vial
w	water

Superscripts

Diffuse interface model

atm	atmospheric
eff	effective